Carrier Transport in High-Speed Photodetectors Based on Two-Dimensional-Gas

A Thesis

Submitted to the Faculty

of

Drexel University

by

Xia Zhao

in partial fulfillment of the

requirements for the degree

of

Doctor of Philosophy

November 2006

Dedications

Dedicate to my parents, my sister and my husband for their love and support.

Acknowledgements

This dissertation summarized the research work I have accomplished during my graduate study in Drexel University. Over all these years, I obtained tremendous help from all the people around and I cannot leave the dissertation without expressing my gratitude to them.

First of all, I would like to thank my supervisor, Dr. Bahram Nabet, for his all the time support and guidance. I benefited a lot from his valuable guidance, not only in the direction of research, but also in my method of research, which for me was offen of greater importance.

Many thanks to our generous collaborators, Dr. Adriano Cola, Dr. Quantanra Fabio and Andrea Terson at IMM/NRL in Italy, for their tremendous efforts in fabrication of the 2-DHG devices and I-V, C-V characterizations of the devices. Particularly, Dr. Cola offered valuable thoughts and discussions in data analysis. I would also like to dedicate many thanks to Dr. Marc Currie, working with Naval Research Laboratory, for his assistance in high-speed measurement of the devices and his valuable suggestions in measurements. Our collaborator in Drexel, Dr. John Spanier, deserves many thanks for his financial support in the ISE-TCAD software.

I owe a lot to Eric Gallo, who directly contributed to this work. My graduate research could not be able to finish without his long-term and earnest help during my whole graduate study. He has been involved with device fabrication in Italy and high-speed measurement in Washington D.C.. He helped me with editing any document that might lead to publication. In the same group, we shared many research topics. I benefited a lot from discussions and arguments with him, not only limited to the research. All in all, he has been helping me all the time during my stay at Drexel University, on both research and graduate study life in the U.S.. I would also like to appreciate our previous group members, Dr. Xiying Chen, being so helpful with my research, Mr. Hungjen Huang and Ms. Athena Bauerle for their valuable discussions, arguments and cooperation in research.

I would further thank Dr. Yifei Li for his assistance in providing equipments and assistance in optoelectronic measurement setup; and all my friends in Drexel for their friendship.

Finally, my parents and sister, they deserve my most sincere gratitude. Though they live far from me, they always there, believe in me, encourage me, love me. Last but not the least, my husband, it is his encouragement and love that supported me through all these years. I would never have been able to stand here and finish the dissertation without him.

Table of Contents

CHAPTER 1: INTRODUCTION 1

1.1. BACKGROUND 1
1.2. HIGH-SPEED PHOTODETECTORS 5
1.2.1. Speed Limitations 5
1.2.2. Performance Tradeoffs 7
1.3. LITERATURE REVIEW 12
1.4. SCOPE AND ORGANIZATION OF THE DISSERTATION 15

CHAPTER 2: MSM STRUCTURE AND 2DEG DEVICE 18

2.1 MSM STRUCTURE 18
2.1.1 Capacitance Analysis 18
2.1.2 Transient Current Response of MSM 20
2.2 EXPERIMENTAL RESULTS OF THE 2DEG DEVICE 24
2.2.1 2DEG Device Structure, Design and Fabrication 24
2.2.2 Experimental Evaluations of the Time Response 26
2.3 STATIC AND DYNAMIC SIMULATION RESULTS 27
2.3.1 Static Behavior 28
2.3.2 Dynamic behavior 37
2.4 CONCLUSION 50

CHAPTER 3: 2DHG DEVICE DESIGN AND PERFORMANCE 52

3.1 TWO-DIMENSIONAL-HOLE-GAS (2-DHG) DEVICE DESIGN AND FABRICATION 53
3.1.1 Device Design and Optimization 53
3.1.2 Device Fabrication 62
3.2 DARK AND PHOTOCURRENT PERFORMANCE 65
3.2.1 Dark Current Characterizations 68
3.2.2 Photocurrent 70
3.2.3 Responsivity 71
3.2.4 Current spectrum 72
3.3 OPTICAL STRUCTURE CHARACTERIZATION 72
3.3.1 Introduction 72
3.3.2 Reflectance Simulation 73
3.3.3 Reflectance Spectra Characterization 76
3.4 TIME RESPONSE 77
3.4.1 Introduction 77
3.4.2 Simulation Results 78
3.4.3 Experimental results, Observations and Analysis 88
3.5 CONCLUSION 99

CHAPTER 4: CAPACITANCE-VOLTAGE CHARACATERISTICS 101

4.1 APPLICATION FOR HIGH FREQUENCY MULTIPLIER 101
4.2 C-V CHARACTERISTICS 103
4.2.1 Maximum Capacitance (Cmax) 104

4.2.2 Minimum Capacitance (Cmin) 105
4.3 OPTICAL MODULATION OF C-V 108
4.4 SIMULATION AND THE MODEL 110
4.5 DISCUSSIONS 116
4.6 CONCLUSIONS 118

CHAPTER 5: CARRIER TRANSPORT IN TWO-DIMENSIONAL-GAS 120

5.1 INTRODUCTION 121
5.2 PHOTOGENERATED CARRIER TRANSPORT IN 2-D GAS 122
5.2.1 Electronic States 122
5.2.2 Electron-Electron Scattering with EMC simulation 125
5.3 DISCUSSION 135
5.3.1 2-D versus 3-D gas system 135
5.3.2 Schottky contacts 136
5.4 CONCLUSION 137

CHAPTER 6: FUTURE WORK AND CONCLUSIONS 138

6.1 FUTURE WORK 138
6.1.1 2DEG/2DHG Device Design 138
6.1.2 Edge-coupled traveling-wave Design 152
6.1.3 Extension of theoretical work 155
6.2 CONCLUSIONS AND CONTRIBUTIONS 159

LIST OF REFERENCES 162

VITA 174

List of Tables

Table 2.1 Calculated capacitance with respect to different finger gaps and widths. 19
Table 2.2 Performances of the 2-DEG device at different electrode configurations. 27

Table 3.1 The Layered structure for 2-DHG device. 62
Table 3.2 Parameters for curve fitting of time response with Gaussian distributions. 92

Table 4. 1 Hole concentrations in 2-DHG and δ-doping layer at different valence band offsets ΔE_v 115

Table 5.1 Binding energies and carrier population in each subband. 124

Table 6.1 Material parameters for InAs and GaAs. 147
Table 6.2 Layered structure design for 2-DEG/2-DHG based photodetector design. 150
Table 6.3 Layered structure for InP material system. 158

List of Figures

Figure 1.1 Schematics of conventional fiber optic communication link with photodetector in the receiver [2]. 1
Figure 1.2 Band gap of semiconductor materials and corresponding wavelengths v.s. Lattice constant [12]....................4
Figure 1.3 Schematic diagrams of the p-i-n photodetector (a) and MSM (b) photodetector............5
Figure 1.4 The schematic diagram of carrier transit and recombination limits...............6
Figure 1.5 The schematic plots of edge-coupled photodetector with electrical and optical waves propagation in the waveguide structures. 9
Figure 1.6 Band structure of an UTC photodiode. Only electrons pass through the collector.......11
Figure 1.7 The main trend in progress of the high-speed photodetectors. APD: Avalanche Photodetector. UTC: Uni-Traveling Carrier. WGPD: Waveguide Photodetector. TWPD: Traveling-wave Photodetector. VMPD: Velocity-matched Photodetector. 12

Figure 2.1 Electrical field dependent electron and hole velocities [60]. 21
Figure 2.2 Illustration of the photocurrent contributions from electrons and holes (a) An electron-hole pair is generated in the photodetector (b) the electron and hole contributions to the photocurrent. 21
Figure 2.3 Schematics of the cross section of the 2-DEG based MSM photodetector..................24
Figure 2.4 Illustration of the interdigitated MSM electrode Patten. Active region is built on a mesa top. 25
Figure 2.5 The transient current response of the 2-DEG MSM photodetector in time (a) and frequency domain (b) [63]. 26
Figure 2.6 Illustration of cross section of an interdigital structure for simulation. The region between two dot lines is one unit cell for simulation. 29
Figure 2.7 The schematic diagram of the mesh grid for the device simulation. Coordinates of *x-y* plane is given. 29
Figure 2.8 Three dimensional view of static conduction band for the δ-doped 31
Figure 2.9. The evolution of the conduction band with external voltage for doped (upper row) and undoped device (bottom row). The external voltages applied from left to right are 1, 2, 3, 4, 5-V respectively for both upper and bottom rows. 32
Figure 2.10 Three dimensional view of static electron concentration for the δ-doped (right) and the undoped HMSM (left). Cathode is at the left; anode is at right. High concentration of 2-DEG exists even under the lateral bias. Coordinates are the same as Figure 2.9. 33
Figure 2.11 Three cuts of the conduction band along the direction of growth for the δ-doped (left) and undoped device (right)...............34
Figure 2.12 Two dimensional electric field distributions for the δ-doped (bottom) and undoped device (top). 35
Figure 2.13 (a) Illustration of the photocurrent in structure by (b)Counting current by charge collection at the electrode (c)Counting current during the whole transit time. 38
Figure 2.14 The electrical field used for dynamics calculation. Left column is for undoped device; right column is for doped device. (a) 3-D view of intensity (b) 2-D view of intensity (c) 2-D

view of vector. 43
Figure 2.15 Electron distribution of undoped (left column) and doped (right column) W2G2 HMSM with 5V bias. There figures show the carrier distribution at (a)3-ps, (b) 6-ps, (c) 9-ps, (d) 12-ps intervals. (Scales in the figures are in unit of μm). 45
Figure 2.16 Hole distribution of undoped (left column) and doped (right column) W2G2 HMSM with 5V bias. There figures show the carrier distribution at (a)3-ps, (b) 6-ps, (c) 9-ps, (d) 12-ps intervals. (Scales in the figures are in unit of μm). 46
Figure 2.17 Time response comparison between doped (bottom) and undoped (top) device with separated contributes from electrons and holes....49
Figure 2.18 Comparisons of time responses due to electrons for figure gap of 2 and 4-μm devices. 50

Figure 3.1 Illustration of InGaAs compressive strain on GaAs substrate. 54
Figure 3.2 Energy band diagram for $Al_{0.3}Ga_{0.7}As/In_{0.35}Ga_{0.65}As/GaAs$ heterojunction. 55
Figure 3.3 Doping concentrations of the 2-DHG for different delta doping level with (a) Uniform doping (b) Delta doping. 57
Figure 3.4 The ratio of 2DHG and δ-doping concentration at different doping levels. 58
Figure 3.5 (a) Hole concentration distribution in the 2DHG at different thickness of spacer (b) Peak 2DHG concentration and ratio of 2DHG/δ-doping at different thickness of spacer....60
Figure 3.6 Two dimensional field vector distributions in the doped (bottom) and undoped (top) device at equilibrium. 61
Figure 3.7 (a) Top view of the device with electrode (b) Cross section of the device on wafer. ...62
Figure 3.8 SEM pictures of the epilayer structure, courtesy of CNR-IMM. 64
Figure 3.9 SEM pictures of the interdigitated fingers, courtesy of CNR-IMM. 64
Figure 3.10 (a) Simulated energy band diagrams under equilibrium (b) A close-up look at the heterointerface. 65
Figure 3.11 Extension of the 2D path of current flow to the 1D. 66
Figure 3.12 Dark current for W2G4 device on low doped and high doped wafers. 68
Figure 3.13 Photocurrent at different input optical powers for W2G2 device. 70
Figure 3.14 Photocurrent subject to different incident optical power for high doped W2G2 device at V= 5V. The linear fit of the curve is also shown. 71
Figure 3.15 The photocurrent spectrum for low doped W2G2 device. 72
Figure 3.16 Schematic diagram of Fabry-Perot Cavity. 73
Figure 3.17 Wave transmission and reflection in a single layer. 74
Figure 3.18 Transmitted and reflected waves in a multilayers structure. 75
Figure 3.19 Experimental reflectance on high doped and low doped wafer compares with the simulated reflectance. 77
Figure 3.20 Three dimensional view of the electrical field in (a) *Ex* component (b) *Ey* component. 79
Figure 3.21 (a) Lateral field cut in the middle of the absorption region (b) Vertical field cut underneath the anode. 80
Figure 3.22 Vertical field cut in the middle of the absorption region. 81
Figure 3.23 Evolution of the electron concentration and corresponding contribution to the photocurrent. 83

Figure 3.24 Evolution of the hole concentration and corresponding contribution to the photocurrent. 85
Figure 3.25 (a) The schematic diagram of carrier movement in the absorption region (b) Two-dimensional view of the potential distribution at V=5....86
Figure 3.26 Time evolution of electrons (a) and hole (b) in doped and undoped devices. 87
Figure 3.27 (a) Transient time response for W2G2 device at voltage of 10 V (b) Corresponding response in frequency domain....89
Figure 3.28 (a) Time response at different external voltage (b) the normalized response. 91
Figure 3.29 Three components of the time response....92
Figure 3.30 (a) 2-D extension of depletion region with increased external voltages for absorption thickness of 118-nm (b) for absorption thickness of 1-μm. 94
Figure 3.31 Normalized second peak for W2G2 device on low doped wafer at different voltages. 95
Figure 3.32 Normalized time responses for geometries of G2 and G4 devices on low doped wafer. 96
Figure 3.33 Time response for high doped W2G2 device under different external voltages. 98
Figure 3.34 Lateral component of the electrical field cut in the middle of the high doped device 99

Figure 4.1 Capacitance-voltage characteristics of the high and low-doped devices in the dark at probe frequency of 10 kHz....103
Figure 4.2 The C-V characteristics for different electrode geometries. 105
Figure 4.3 Lateral depletion of the 2DHG creating a capacitance determining the $C_{min.}$....106
Figure 4.4 Simplified model of 2D electron gas – p-type semiconductor junction....107
Figure 4.5 C-V characteristics under light at probe frequency of 10 kHz. The slope of C-V depends on the incident power levels....108
Figure 4.6 C-V characteristics under light at probe frequency of 1 MHz. 109
Figure 4.7 Simulated C-V characteristics for high doped W2G2 device. 111
Figure 4.8 (a) Simulated potential distribution at 5-V bias voltage (b) Corresponding hole density at equilibrium. 111
Figure 4.9 The hole distribution at voltage from 0 to 0.7V with step of 0.1V....112
Figure 4.10 The equivalent circuit of the 2-DHG structure. 113
Figure 4.11 Proposed circuit model, including C0, C1 and C2, representing contributions from background charge, delta-doping layer, and 2DHG, respectively. 114
Figure 4.12 C-V profiles at different charge distributions between δ-doping layer and 2-DHG. The C-Vs presented corresponds to the heterostructure with ΔE_v of 0.09, 0.16, 0.25, 0.28-eV, respectively. X axis is the voltage, y axis is the capacitance....115
Figure 4.13 The probe frequency response of the capacitance for high doped W2G2 device. 118

Figure 5.1 A typical conduction band diagram of AlGaAs/GaAs heterostructure with 2DEG at the interface....121
Figure 5.2 Self-consistent effective potential (top), and the corresponding wave functions for the lowest five subbands at 300K respectively (bottom). 125
Figure 5.3 A simple flowchart of a Monte Carlo simulation program. 127
Figure 5.4 Electron-electron scattering form factors as a function of wave vector for a triangular

well. X axis is the wave vector q, Y axis is the form factor. The indices *ijmm* label the initial, *i/j*, and final subband states, *m/n*. 129
Figure 5.5 Histogram of e-e scattering rate with self-scattering technique....................131
Figure 5.6 Time evolution of the energy distribution in 2DEG when perturbed by extra electrons with energies above average. 133

Figure 6.1 A simple schematic diagram of 2-DEG/2-DHG device to be designed. 140
Figure 6.2 The AlGaAs refractive index and energy bandgap for different compositions [131]. 142
Figure 6.3 Schematic diagram of Resonant Cavity Enhanced structure [63]....................144
Figure 6.4 The optimization of RC limited and transit time limited frequency response. 145
Figure 6.5 Energy band diagraom for AlGaAs/InGaAs/GaAs. 147
Figure 6.6 The calculated and measured critical thickness of InGaAs as a function of In mole fraction [74]. 148
Figure 6.7 Equivalent circuit of semiconductor photodetector. 151
Figure 6.8 Schematic diagram of distributed MSM photodetector. 153
Figure 6.9 Schematic diagram of heterodimensional contact. 157

Abstract

Carrier Transport in High-Speed Photodetectors Based on Two-Dimensional-Gas
Xia Zhao
Supervisor: Bahram Nabet, Ph.D.

Monolithically integrated high-speed photodetectors are important components in fiber communications and optoelectronic integrated circuits (OEIC) with metal-semiconductor-metal (MSM) photodetectors (PD) being the device of choice due to the its high overall performance and technology compatibility with integrated circuits (IC). The speed of conventional top illuminated MSM-PD is limited by the transit time of photogenerated carriers. The concept of internal vertical field, developed in the MSM intrinsic absorption region by the two-dimensional-gas along the heterojunction, is proposed and implemented for the purpose of facilitating carrier transport, hence improving the transit time limitations. The time response of a two-dimensional-electron-gas (2-DEG) based photodetector suggests an enhanced electron transport but a long tail due to the slow holes. We have designed and fabricated two-dimensional-hole-gas (2-DHG) based MSM photodetector to investigate hole transport in the vertical field MSM photodetector. Simulation of charge carrier transport, verifies experimentally observed behavior, which manifests the enhanced hole transport benefit from the vertical field.

In addition, the 2-DHG based MSM structure device shows excellent capacitance-voltage (C-V) characteristic making it an excellent candidate for applications in odd-order high frequency multipliers. The high Cmax/Cmin ratio of 113 and high sensitivity of 35 are one of the best results reported. In addition, optoelectronic measurements demonstrate the slope of the C-V relationship can be modulated by the intensity of the incident optical power. A model describing the source of the C-V results is proposed along with the simulation results verifying the observed C-V behavior.

In order to produce a complete picture of charge transport and collection, we developed a program using Ensemble-Monte-Carlo (EMC) method incorporating the electron-electron scattering in the 2-DEG confined by AlGaAs/GaAs heterojunction. The result reveals an energy thermalization time of tens of femto-second in the 2-DEG, which suggest the 2D gas has the potential to collect the photogenerated carriers.

Based on all previous experimental results and analysis, a 2-DEG/2-DHG combined structure has been proposed on GaAs substrate. The design, taking advantage of the vertical field and fast thermalization time in the confined 2D gas, results in a wide bandwidth, high external quantum efficiency for vertically illuminated MSM device.

CHAPTER 1: INTRODUCTION

1.1. Background

Photodetectors have been widely applied in optical transmission systems. In ever-increasing bit rates of fiber-optical transmission systems, Tera-bits/s have been demonstrated [1] by using wavelength division multiplexing (WDAM) or optical time division multiplexing (OTDM) techniques. The development of optical fiber transmission systems and their penetration into local area networks has greatly increased the demand for high performance optoelectronic devices, including photodetectors, lasers and modulators. Photodetectors play a central role in the fiber optical communication system, whose schematic diagram is shown in Figure 1.1. In these applications, photodetectors transfer the time-modulated optical power to microwave power.

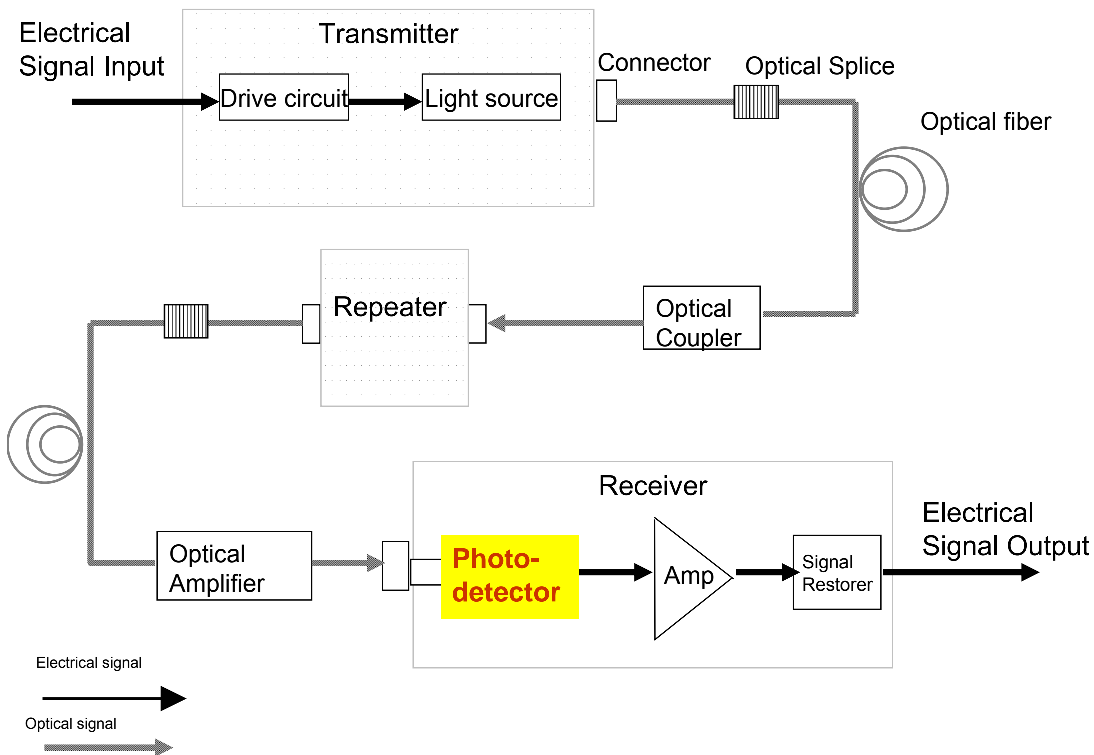

Figure 1.1 Schematics of conventional fiber optic communication link with photodetector in the receiver [2].

In addition to fiber optics, optical measurement systems employ photodetectors and photodetector arrays in a wide range of applications, such as, high-precision length measurement, light pattern and spectrum analyzer, velocity measurement in a luminous flow, etc. Imaging applications such as three-dimensional (3-D) imaging, sensing, and space-related spectroscopy have also greatly increased the demand on high sensitivity, low power, high resolution photodetector arrays and large area devices that operate in the UV and short wavelength infrared (SWIR) range (0.8-μm ~ 2.2-μm). Other applications include high-speed sampling, optoelectronic integrated circuits (OEIC), high-speed optical interconnection, optoelectronic mixers for microwave single-sideband modulation [3].

Several aspects evaluating photodetectors are bandwidth, efficiency, saturation power, and dark current. (1) Broad bandwidth and high-speed allow photodetectors capable of responding to high optical modulation rates. (2) High transfer efficiency enables the photodetectors to convert high portion of optical power to electrical signal. (3) High saturation power allows the photodetectors to sustain high optical power without distorting the output electrical signal. (4) Low dark current and low noise improve the signal-to-noise ratio to obtain a large spurious-free dynamic range and high RF gain. The bandwidth of the photodetector has steady improved, approaching 500-GHz [4] during the last decade by pushing the thickness of intrinsic region to the limit of nanometer scale [5], employing the traveling-wave design and LT-GaAs material [6]. The efficiency of the photodetector varies a lot from design to design. For edge-coupled design, the efficiency is usually less than 30% [7], and the design with LT-GaAs intrinsic region or uni-carrier-traveling design are even less, i.e., 8% [8] or less. However, the vertically illuminated configuration can reach as high as 99% [9], and the resonant-cavity design could approach 200% or more. Different applications require different the prioritization of these performance figures, particularly, extremely high-speed and wide-bandwidth

detectors are needed in optical fiber communication links, optical switches, etc. In applications such as imaging, it is essential to attain very low dark current densities and low noise, in addition, the development of the optical amplifier has created demand for high-power PDs.

The photodetection process can be schematized by the following steps:

- Absorption of photons in the material with generation of charge carriers;
- Drift of charge carriers under an internal electrical field;
- Collection of charge carriers at the contacts of the device;
- Detection of charge and signal.

The first point requires that, in order to generate an electron-hole pair, the photon energy has to be greater than the semiconductor material energy bandgap, $h\gamma \geq E_g$, where γ is the frequency of the photon. A variety of material systems have been employed for different wavelength detections due to their proper bandgap values. Generally, for fiber optical communication applications, GaAs material system is used for short wavelength detection, such as 850-nm for short-haul transmission; InP material system is used for 1310-1550 nm wave detection for long-haul transmission. The quaternary compound III-V $In_xGa_{1-x}As_yP_{1-y}$ compatible with growth on InP substrate, depending on composition, yields a threshold wavelength from 1000 to 1800-nm; that is, we have a heterojunction photodiode in the ternary $In_xGa_{1-x}As$ between layers of InP [10]. Wider range of wavelength detector can be achieved by employing III-Nitrides alloys toward shorter wavelength, and antimony-based material toward longer wavelength [11]. Figure 1.2 shows the energy bandgap, Eg, and lattice constant of III-V semiconductors and some of the related alloys.

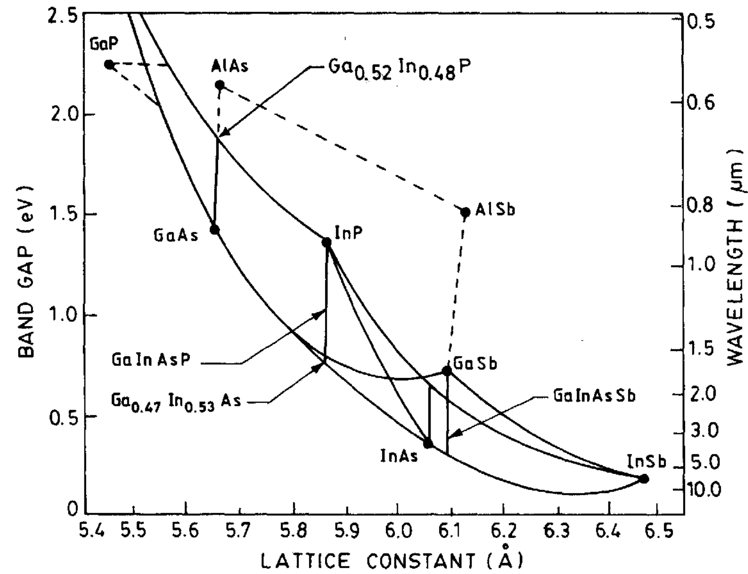

Figure 1.2 Band gap of semiconductor materials and corresponding wavelengths v.s. Lattice constant [12].

From the direction of illumination, the PD can be classified as vertically illuminated photodetectors (VPD) and edge-coupled photodetector. VPDs are good candidate for monolithic integrated circuit applications due to their planar structures. Edge-coupled PD overcomes the theoretical bandwidth-efficiency limitations in VPD by separating the electrical transit path from optical propagation path.

PDs can be classified on the basis of detection mechanism as the avalanche photodiodes (APDs) and PN junction photodiodes, with APDs being able to obtain 5-10 dB or better sensitivity than usual PN junction detectors due to their multiplication process in absorption region, thus achieving high gain detection.

On the basis of device structure, semiconductor junction PDs can be classified as the p_type-intrisic-n_type (p-i-n) photodiode, and metal-semiconductor-metal (MSM) photodetector (Schottky PD included). The schematic structure of the two photodetectors is shown in Figure 1.3. A

usual p-i-n photodetector consists of a highly doped p+ layer at the top, intrinsic photo-absorption region in the middle and a highly doped n+ layer at the bottom; those layers are in vertical arrangement. MSM PDs consist of interdigitated metal fingers on semiconductor, and they detect photons by collecting electron-hole pairs that drift under the electrical field applied between the fingers. Their structures are completely compatible with microwave monolithic integrated circuits, thus attractive for microwave application [13].

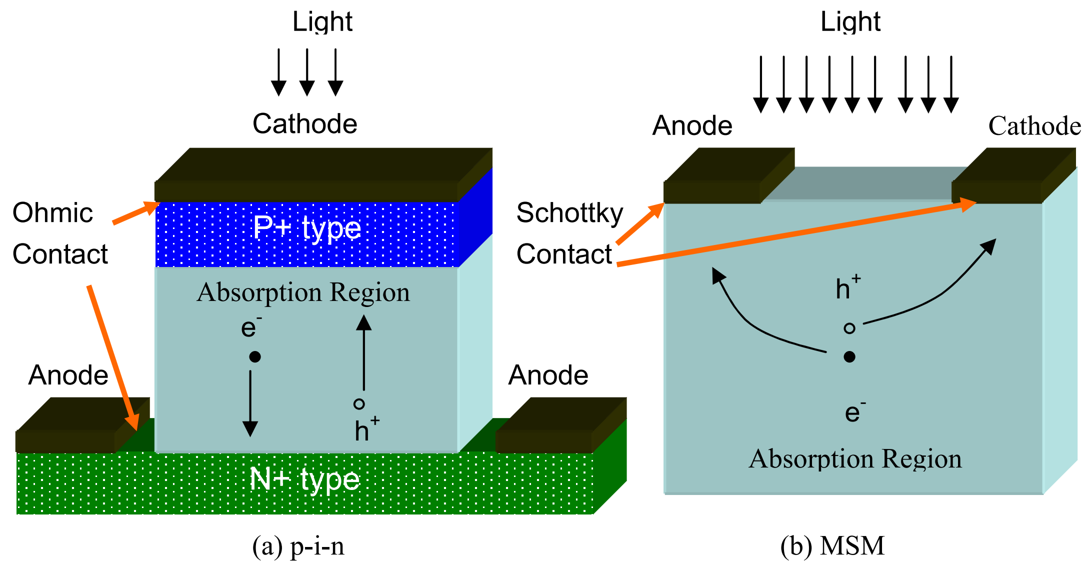

Figure 1.3 Schematic diagrams of the p-i-n photodetector (a) and MSM (b) photodetector.

1.2. High-speed Photodetectors

1.2.1. Speed Limitations

High-speed photodetectors have been developed in the past few decades. For an ultrawide-band response, the intrinsic response of the PD should be much faster than the required systems response. Three aspects can be identified as the major factors that limit the speed and bandwidth performance of PDs, those are (1) carrier-recombination lifetime τ in the absorption region (2) resistor-capacitor (RC)

charging and discharging time of the external circuit (3) carrier-transit time in the intrinsic region. In recombination-time-limited PD's, shorter recombination time and therefore higher speed are achieved through introducing high-density recombination centers into the semiconductor when processing the semiconductor material. This drastically lowers sensitivity and makes fabrication less compatible with Field-Effect-Transistor (FET) IC fabrication. For RC-time-constant limited devices, the capacitance between the two electrodes is the major source of capacitance, which would limit the device speed performance. MSM structure greatly enhances the RC limitations by employing the planar interdigital finger which is extremely small compared to the p-i-n structures [14]. More recently, the traveling-wave photodetectors (TWPD) [15] have been developed to overcome the ever-increasing speed limitation due to RC lump elements. The transit-time-limited detectors, where the response is determined by the time spent by the carrier transiting from where they are generated to the corresponding collecting electrodes, are usually fabricated on high-quality semiconductors and have a sensitivity of several orders of magnitude higher than that of recombination-time-limited devices.

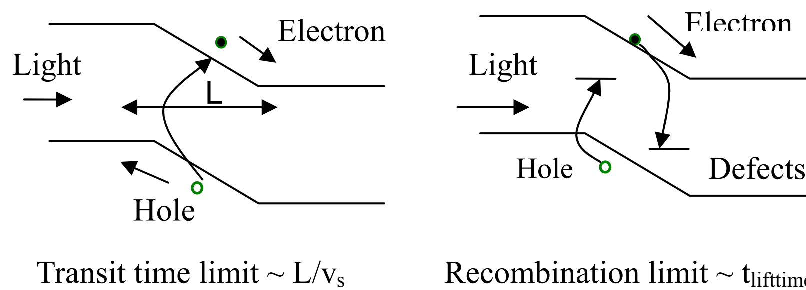

Transit time limit ~ L/v_s Recombination limit ~ $t_{lifttime}$

Figure 1.4 The schematic diagram of carrier transit and recombination limits.

Figure 1.4 shows the schematic diagram of speed limitations. The photogenerated carriers are either swept out by the strong built-in fields in the intrinsic region (left of figure 1.4), or removed by

the recombination centers (right of figure 1.4). In the former case, the speed is limited by transit time, the latter by the carrier recombination time.

Theoretically, the speed limitation has two major components that contribute to the current response of a photodetector, represented by [16]

$$J_{\mathrm{int}rinsic}(t) = \frac{1}{L}\int_{L}[J_{conduction}(t) + \frac{\partial}{\partial t}(\varepsilon E(t))] \qquad (1.1)$$

where, L is the thickness of intrinsic region, $J_{conduction}(t)$ is photocurrent due to the device response, namely, the photogenerated carriers moving at the force of internal electrical field before they are collected by the electrodes or eliminated by the recombination centers. Its transient response is limited by transit-time across the intrinsic region, or the carrier recombination time. $\frac{\partial}{\partial t}(\varepsilon E(t))$ is the displacement current, representing the charge and discharge processes of the overall circuits, which include intrinsic capacitance, parasitic capacitance and inductance of the metalization surrounding the photodetectors. The displacement current response subject to the RC time constant or the microwave distributed effects.

For carrier-transit time limited PDs, the 3-dB-down electrical bandwidth f_t is subject to carrier traveling distance D [17],

$$f_t \cong \frac{3.5\bar{v}}{2\pi D} \qquad (1.2)$$

$$\frac{1}{\bar{v}^4} = \frac{1}{2}\left(\frac{1}{v_e^4} + \frac{1}{v_h^4}\right) \qquad (1.3)$$

where, v_e and v_h are the electron and hole saturation velocities, respectively. Given $v = 5 \times 10^6$ cm/s for GaAs (for 0.85 μm: short wavelength) photoabsorption layer, D of less than 0.2 μm is required for 140-GHz bandwidths.

1.2.2. Performance Tradeoffs

Usually the speed of the photodetector device is limited by the carrier transit time, which is determined by the device structures and dimensions, while the photodetector circuit is optimized by RC-time constant[18] or traveling wave structures[19]. Trade-offs always exists when achieving overall optimized performances.

1.2.2.1. Bandwidth-efficiency trade-off

Vertical illuminated PD: The intrinsic capacitance and transit region should be both minimized to improve the device speed. For typical VPDs p-i-n structure, reducing the thickness of intrinsic absorption layer in order to achieve less transit time increases the parasitic capacitance, which prevents the further improvement of the speed performance and imposes an up limit speed of 200-GHz. On the other hand, the thin absorption layer greatly jeopardizes the absorption of photons, hence the internal quantum efficiency, given the absorption coefficient at certain wavelength in a certain material. For a typical p-i-n or Schottky VPD, the common technique to improve the internal quantum efficiency is multiple pass schemes using return light reflected by the electrode and bottom mirror. The input light impinges on the device and travels vertically through the absorption layer, the internal quantum efficiency is expressed as[20]:

$$\eta_{in} = (1 - e^{-\alpha d})(1 + re^{-\alpha d}) \cong (1 + r)\alpha d \qquad (1.4)$$

where, r is the reflection coefficient at the electrode, α is the absorption coefficient, and d is the thickness of the photoabsorption layer. Combining with Equation (1.2) in which $D=d$ in the VPD, the bandwidth-efficiency limit is:

$$f_t \eta_{\text{int}} \cong \frac{3.5\bar{v}(1 + r)\alpha}{2\pi} \qquad (1.5)$$

In the case of r = 0~1, the bandwidth-efficiency products are 30~60-GHz at 0.85 μm for GaAs when the GaAs absorption coefficient is 1.0 μm^{-1}[21], and 20-40 GHz at 1.55 μm for InGaAs when the

InGaAs absorption coefficient is 0.68 μm^{-1} at 1.55 μm. For MSM-PD, carrier-transit distance $D \cong \sqrt{d^2 + W_g^{\ 2}}$, where W_g is the gap distance between the fingers and d is the thickness of absorption region, we obtain similar results compared to the p-i-n structure.

For vertical illuminated device, this trade-off can be alleviated by employing a resonant-cavity-enhanced structure, where the active region is placed within a Fabry-Perot resonator which allows the thin absorption region accommodates multiple passes of the optical radiation.

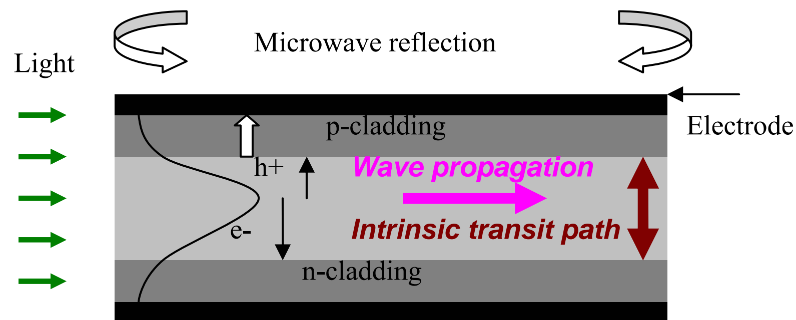

Figure 1.5 The schematic plots of edge-coupled photodetector with electrical and optical waves propagation in the waveguide structures.

Edge-coupled PD: By distributing the RC elements and impedance matching to external circuits, the edge-coupled waveguide p-i-n and MSM photodetectors are created to overcome the limitations imposed by trade-off between speed and efficiency in the VPD structure. Typical schematics of edge-coupled photodetector are shown in above Figure 1.5. The waveguide structure is formed by sandwiching the intrinsic absorption layer, i.e. GaAs, with two cladding layers of large bandgap material, i.e. AlGaAs, to confine the optical wave. Light is coupled from the edge, as shown in the Figure 1.5, and the propagation of the light, namely, the path of photon absorption, is along the wave guide. The photogenerated carriers move up and down, creating transit paths perpendicular to the

propagation of optical wave. This alteration allows for the independent design and optimization of speed and internal quantum efficiency. To improve the internal quantum efficiency, it is necessary to increase device length rather than the thickness of the absorption layer. However, the edge-couples PDs suffer from external quantum efficiency. For edge-coupled structure, it is difficult to obtain efficient optical coupling or a good overlap integral between the incident optical field and the optical field being detected at the PD. This is because the diameter of an input light, no less than 2 μm even when focused by lenses, is much larger than the thickness of the thin photo-absorption layer, usually less than 1 μm. It greatly diminishes the external quantum efficiency compares to the vertical illuminated PDs, where the external quantum efficiency approaches to 99%.

1.2.2.2. Bandwidth-sensitivity trade-off

Employ of Low-Temperature (LT) GaAs material in the absorption region is one of the solutions that improve the speed performance. LT-GaAs draws the attention of photodetector designer due to its huge defect densities, thus recombination center densities when the GaAs substrate is grown at temperature of around 200C. Photodetectors with intrinsic region made of LT-GaAs can be fabricated with a picosecond or subpicosecond response, showing 200~300 GHz of bandwidth enhancement over the general GaAs and InGaAs materials, due to its short carrier trapping time, usually less than 1-ps, in the absorption region. According to Ramo's theory [22], photogenerated carriers contribute to the photocurrent as they move. Since most of the carriers have recombined in a short time, no longer being able to contribute to the current, the intensity of the photocurrent is greatly reduced. Given the same intensity of the incident light, we expect much less sensitivity of the corresponding photocurrent detected from the LT-GaAs materials.

Another key limitation to the speed performance is that the photodetector is limited by the slower

velocity of hole, in the intrinsic region. This is particularly severe when device is subject to high levels of optical injection. The uni-traveling carrier (UTC) photodiode has been developed specifically to eliminate the influence of the slow carrier. Figure 1.6 shows the band structure of UTC photodetector. In this type of photodiode, the photogenerated extra holes recombine in the p+ layer, and do not drift across the high-field region, thus do not contribute to the photocurrent. Charge transport is dominant by the fast electrons. The UTC design improves the speed of the device; on the other hand, it improves the power handling capabilities as well at the expense of low internal quantum efficiency. When the overshoot velocity of the electrons occurs, the UTC can achieve saturation current densities 4-6 times higher than that in the p-i-n structures [23].

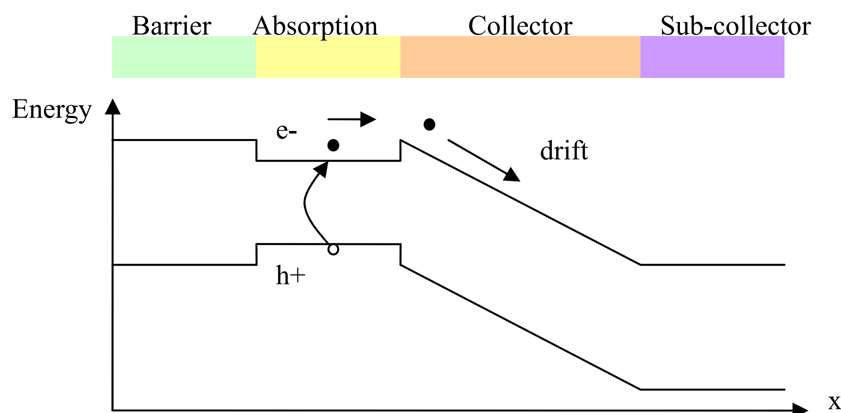

Figure 1.6 Band structure of an UTC photodiode. Only electrons pass through the collector.

As for the slow carriers, which prevent the fast response of the device, another solution without sacrifice the sensitivity and responsivity is collecting them as soon as possible, as we will address in the chapter 3 and chapter 5.

1.3. Literature Review

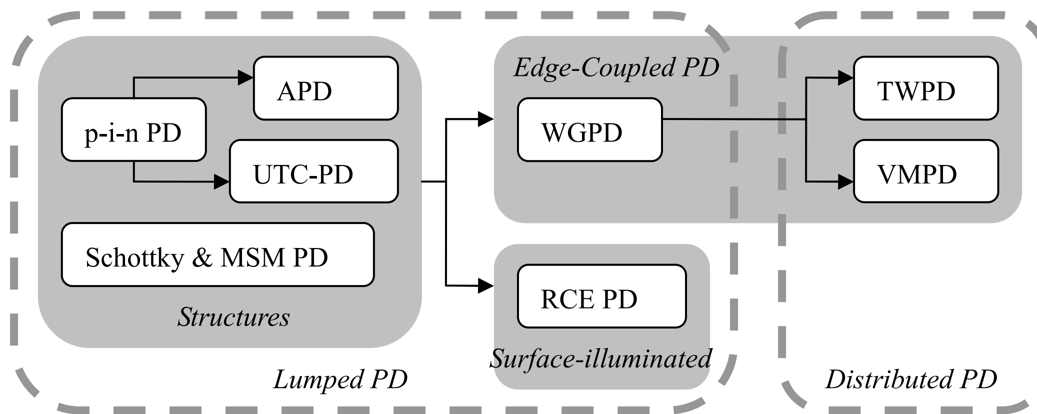

Figure 1.7 The main trend in progress of the high-speed photodetectors. APD: Avalanche Photodetector. UTC: Uni-Traveling Carrier. WGPD: Waveguide Photodetector. TWPD: Traveling-wave Photodetector. VMPD: Velocity-matched Photodetector.

In recent years there has been steady research interest in the development of high-speed photodetectors mainly for short and long haul fiber optical communication applications. Figure 1.7 draws the main trends in the development of the photodetector. P-i-n and MSM photodetectors are the major two types of structure of PDs in application. To further increase the speed and efficiency, conventional PDs employ waveguide and Resonant-Cavity-Enhanced (RCE) structures for edge-coupling and vertical illuminated device, respectively.

MSM-PD's have very low fabrication cost and can be designed for low capacitance resulting in high-speed performance. The study of MSM structure emerged in early 1970's [24] [25]. Earlier stage of the MSM PD was fabricated on GaAsCr [26], amorphous silicon [27], radiation damaged silicon-on-sapphire [28] substrate during 70' and 80's. Due to the development of monolithic fabrication techniques, great progress has been made. Wang and Bloom reported first GaAs Schottky photodiode above 100-GHz bandwidth in 1983 [29]. A transit-time-limited GaAs MSM PD was

reported with finger width of 0.75-μm and finger spacing of 0.5-μm in 1988. This device achieved the impulse response of 4.8-ps full width at half maximum (FWHM) and 3-dB bandwidth of 105-GHz [30]. In 1991, by combing the GaAs Schottky photodiodes and sampler circuits, a bandwidth higher than 150-GHz photodiode was reported [31]. Recombination-time-limited MSM PD on low-temperature-GaAs (LT-GaAs) with a finger width and spacing of 0.2-μm, a FWHM of 1.2-ps, and 3-dB bandwidth of 375-GHz was reported in the same year [32]. In 1992, an MSM with finger width and finger gap of 25-nm was reported achieving bandwidth of 510-GHz on LT-GaAs [5].

The research in this stage mainly deals with optimizing a single optoelectronic device. Soole et al. studied variation of the transport parameters with finger spacing and thickness of the active layer [33]. Space charge, thus field screening created by photogenerated electron-hole pair was studied by Zhou et al [34].

The *second* stage of photodetector design, aiming at further improving the speed and efficiency of the devices, driven by the ever increasing demand on high-speed high-power applications, split to two major branches. One branch is the vertically illuminated device, and efficiency improvement was achieved by adding Resonant-Cavity-Enhanced (RCE) structure, Distributed-Bragg-Reflector (DBR) structures [35], and further optimizing the internal structure. The other branch was developed toward edge-coupled Waveguide Photodetector (WGPD) design. The first high-speed edge-coupled waveguide photodetector was demonstrated in 1986, with a bandwidth of 28 GHz and an efficiency of 25% [7]. In 1995, the first traveling wave structure photodetector with a bandwidth of 176-GHz was demonstrated by Giboney et. al [15]. In 1998, the same group reported a p-i-n LT-GaAs photodetector with 560-GHz -3dB bandwidth using LT-GaAs traveling wave technique [8]. Same progress has been made in the long wavelength regime, namely the InP and InGaAs material based devices. Bowers and

Burrus reported and InGaAs p-i-n photodetector with a bandwidth above 50-GHz in 1987 [19]. In 1990, Wey at al. reported a 16-ps response instrument limited photodiode [36]. Also in 1991, Wey et al. demonstrated the first long wavelength photodetector above 100-GHz bandwidth, in which the double graded layers were used to improve the device speed [37]. In 1994, Kato et. al. reported a 110-GHz bandwidth of mushroom type waveguide photodetector. Using air-bridge and undercut mesa to reduce the RC-time constant [38, 39]. In 1995, Tan et. al. reported a 120-GHz bandwidth p-i-n photodetector [18], in 1998, Shimizu et. al. used a UTC technique to enhance the bandwidth up to 150-GHz [40]. J. Shi reported MSM TWPDs on LT-GaAs substrate with transformed bandwidth of 570-GHz in 2001 [4]. A. Stőhr et al. have demonstrated the TWPDs in the 1.55-μm wavelength for local oscillator applications in 2003 [41].

The research during this stage mainly focuses on the interaction of optical wave and electrical wave signal. The theory of standing-wave [42] and traveling-wave [43] have been applied in device design. The distributed component optimization, RCE structure, waveguide structures are employed to enhance overall performance.

More developments on photodetectors, not included in the main stream, have been reported. A lateral p-i-n with an unmodified 0.25-μm CMOS technology was reported operating at 850-nm in 2002 [44]. Silicon based MSM designs for ultrafast pulse detection at 840-nm was demonstrated with FWHM of 3.5-ps [45]. Lo. et al. reported grade superlattice-like layered Si-based MSM photodetector in 2005 [46]. MacDonald reported MSM on polysilicon with a bandwidth of 750-MHz at 860-nm [47].

To investigate and analyze device behavior, a large amount of simulation needs to be performed. Several approaches have been investigated. Nakajima et al. have examined the response of GaAs MSM-PD’s by using simplified saturation velocity in one-dimensional space [48]. Soole et al.

approached it by solving motion equations for carriers based on field-dependent velocities [33]. Koscienlniak et al. have investigated the speed issue by solving the one-dimensional Schrodinger equation for ballistic transport [49]. E. Sano [50] and C. Moglestue [51] have calculated the pulse response by two-dimensional Ensemble Monte Carlo(EMC). Averin et al. analyzed the transient response by two-dimensional Ramo's thorem [52]. G. B. Tait [53] has used quantum mechanical treatment.

The major topic of this dissertation is to study the RCE structure based vertically illuminated MSM photodetector. To achieve large bandwidth-efficiency product performance, the two-dimensional (2-D) gas structure is introduced to the device. The purpose of 2-D gas in terms of affecting device behavior is two-folded. One is creating vertical field, which facilitated the photogenerated carrier transport without sacrificing the coupling efficiency; the other is collecting the photo carriers, circumventing their further drifting in the device. Complete picture will be presented in later several chapters. Following section gives the scope and organization of the dissertation.

1.4. Scope and Organization of the Dissertation

This dissertation covers the design, simulation and analysis of 2-D gas based MSM photodetector. We compare the 2-D gas based structure with undoped structure for both simulation and experimental measurements. The results show that a vertical field developed in 2-D gas based structure facilitates photogenerated carrier transport with the aid of the confined 2-D gas. The capacitance-voltage (C-V) characteristics of the 2-DHG device prove its potential for high frequency multiplier applications due to its excellent Cmax/Cmin ratio. Moreover, Carrier transport in 2D gas is addressed with EMC technique, revealing a fast energy thermalization time helping collection of carriers. Based on all previous experimental results and analysis, a new high-speed photodetector design based on

2-DEG/2-DHG structure is proposed.

Chapters are organized as follows:

Chapter 1 has provided the background of this work, including applications, classifications, and development of various photodetectors. The speed performance and corresponding trade-offs have been addressed. The literature review is followed by the major objective of this work.

Chapter 2 provides some technical background and preliminary research work on heterostructure MSM (HMSM) and 2DEG devices. The static and dynamic behaviors of the 2DEG device are simulated using commercially available software and Ramo's theorem, respectively. The simulation results reveal that a vertical field is created in absorption region which facilitates electron transport though it degrades the hole transport. This motivates us to further explore the 2-DHG device.

Chapter 3 discusses the design and fabrication of 2DHG devices, with the intention of studying the slow carrier dynamics. Simulation and measurement results are presented. Major aspects of performances of the 2-DHG device under coverage are the current-voltage (I-V), current spectrum (I-λ), and time response. Simulation results combined with observations in time response manifest the enhanced hole transport benefit due to vertical field, though the electron creates the long tail due to the spreading of the 2-D hole gas.

Chapter 4 addressed the C-V characteristics of the 2-DHG device. The high Cmax/Cmin ratio of 113 and high sensitivity of 35 enable the device for applications in high odd-order frequency multipliers. Optically modulated sensitivity of C-V offers potential for applications in optical mixing, Millimeter-Wave-Integrated-Circuit (MMIC), etc.

Chapter 5 introduces the theory of carrier transport in the 2D gas. We propose the carriers dropping to the 2D gas can reach equilibrium by carrier-carrier scattering in a very short time, which

allows for their fast collection, thus the high-speed of the device. Monte-Carlo simulation incorporating carrier-carrier scattering mechanism is performed and the results are given.

Chapter 6 draws conclusions and proposes future research work. A new design of a vertical MSM photodetector based on both 2DEG and 2DHG structure by taking advantage of carrier transport by energy relaxation in the 2D gas is proposed. The major contributions of this work are (1) simulation of 2-DEG based MSM photodetector, where a vertical field is revealed to facilitate the electron transport; (2) design and analysis of 2-DHG based MSM photodetector; (3) proposal that the photogenerated carriers are collected by the 2DEG by means of electron-electron scattering assisted energy thermalization; (4) development of the high Cmax/Cmin ratio and high sensitivity varactor for odd-order high frequency multipliers application; (5) design of a 2-DEG/2-DHG based heterostructure MSM photodetector with overall enhanced performances.

CHAPTER 2: MSM STRUCTURE AND 2DEG DEVICE

Interdigital MSM-PD's are good candidates for optoelectrical integrated circuit (OEIC) receivers. They play an important role in the detection of optical signal, and are widely applied in optical communication systems and chip-to-chip connections due to their fast response, high sensitivity and low dark current. On the other hand, the fabrication of planar MSM-PD is compatible with usual field-effect transistor (FET) process technology on III-V material substrate, i.e. GaAs. It allows for the monolithic integration with IC logic on the same chip, and there is no additional cost added to logic chip since the metal electrode can be realized in the same procedure as gate metal deposition [54].

2.1 MSM Structure

Metal-semiconductor-metal (MSM) structure, consisting of two metal to semiconductor junctions in back-to-back configuration, was first studied by S. M. Sze in 1971 [24], where the current transport in one dimensional MSM structure was investigated systematically in theory. The MSM photodetector was reported in 1979 by Sugeta [55]. The internal gain and response speed characteristics of MSM-PD were shown to completely satisfy the necessary conditions for monolithic integration [56].

2.1.1 Capacitance Analysis

As one of the major limitations to the operation speed of the photodetector, the capacitance of the device is better to be maintained as low value as possible. One advantage of MSM structure PD over p-i-n PD, beyond its planar processing technology, lies in the extremely small capacitance due to the electrode configuration. For intrinsic and infinitely thick detector material, the capacitance, derived by the conformal mapping technique, is given in [57],

$$C = \frac{K(k)}{K(k')} \varepsilon_0 (1 + \varepsilon_r) \frac{A}{\Lambda} \tag{2.1}$$

where, Λ is the finger period, ε_r is the relative dielectric constant of the semiconductor, A is the

interdigitated area, and

$$K(k) = \int_0^{2\pi} [1/\sqrt{(1-\kappa^2 \sin^2 \varphi)} d\varphi] \quad (2.2)$$

is the complete elliptic integral of the first kind, with

$$k = \tan^2[\pi W / 4\Lambda] \quad (2.3)$$

where, W is the finger width, and

$$k' = \sqrt{(1-k^2)} \quad (2.4)$$

For an MSM-PD based on GaAs, the capacitance for several configurations of the finger width (W) and finger gaps (G) are calculated. Those chosen are typical values of the device dimensions we have used in our investigation. The calculated capacitance per (10 μm)^2 is listed in the Table 2.1. The corresponding charging times to a 50-Ω load are also listed adjacent to each capacitance.

Table 2.1 Calculated capacitance with respect to different finger gaps and widths.

G W	0.5 (fF/ps)	1 (fF/ps)	2 (fF/ps)	4 (fF/ps)
0.5	5.78/0.29	5.00/0.25	3.87/0.19	2.72/0.14
1	3.01/0.15	2.89/0.14	2.50/0.13	1.94/0.10
2	1.43/0.07	1.50/0.08	1.44/0.07	1.25/0.06
4	0.65/0.03	0.72/0.04	0.75/0.04	0.72/0.04

These calculations suggest the capacitance of the device is less than 5 fF/(10 μm)^2 for a typical photolithographically defined electrode structure. A MSM device with finger gap greater than 1-μm, given an active area of 40x40 μm^2 used for fiber coupling, creates an RC charging time of less than 2.4 ps into a 50-Ω load. For finger gap less than 1 μm, a distributed RC element circuit model should be considered.

Above model of MSM capacitance deals with the parasitic capacitance introduced by the

electrode geometry only. For certain structures, such as our device with built-in 2-D gas, the capacitance model should be more complicated than that due to the internal charge distribution in the layered structure. Further detail will be addressed in Chapter 4.

2.1.2 Transient Current Response of MSM

Transit-time limited conventional MSM-PD's have been extensively studied. One-dimensional Monte Carlo simulation predicts a clear temporal separation of the contributions of the electron and hole carriers to the response current [58]. The shape of the total current pulse is characterized by several feature including:

- A rise time
- An initial fast decay
- A subsequent long tail

The rise time consist of intrinsic rise times due to the material response of the device and circuit rise time due to the system response. Intrinsic rise time measures the generation time of photogenerated carriers when subject to the illumination and subsequent separation of electron-hole pair. A direct measurement using picosecond electro-optic sampling techniques found this time is faster than 300-fs, which is negligible compared to any time scale of interest. The circuit rise time measures the response of experimental set-up of the system, which is the major component of the rise time under measurement.

In the intrinsic region of the photodetector, the electrons move towards the anode at saturation velocity [59], the holes with a noticeably slower speed to the cathode. The field-dependent drift velocities of electrons and holes for intrinsic GaAs, the typical material for absorption region in the short wavelength regime, are shown in Figure 2.1. The solid line in Figure 2.1 (a) is calculated by [60],

the dashed and dotted curves are measured data [61] at 300K. Figure 2.1 (b) plots the field dependence of the hole drift velocity at different temperatures [62].

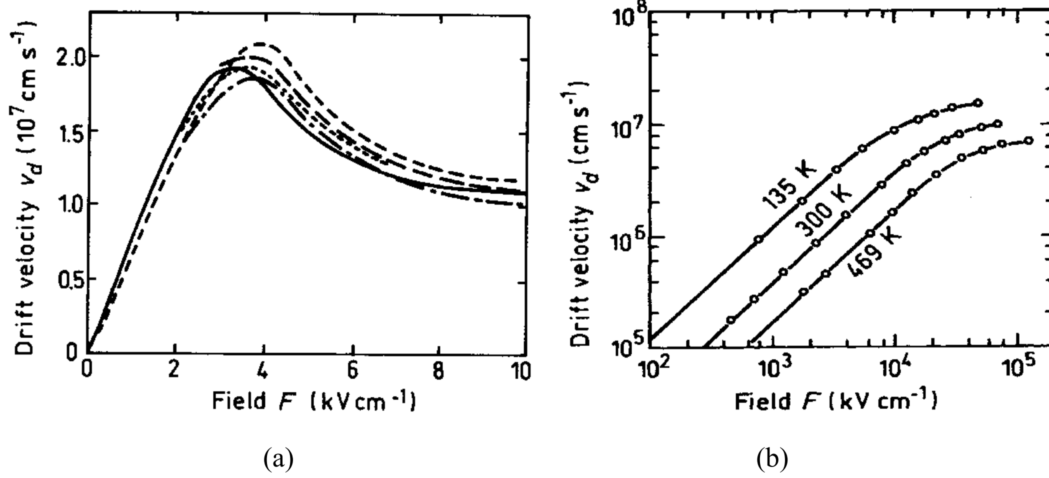

(a) (b)

Figure 2.1 Electrical field dependent electron and hole velocities [60].

Until the drift velocity of holes increases with the field strength at least up to $6\text{x}10^8$-V/cm at room temperature, the local field is too weak for the holes to reach saturation velocity.

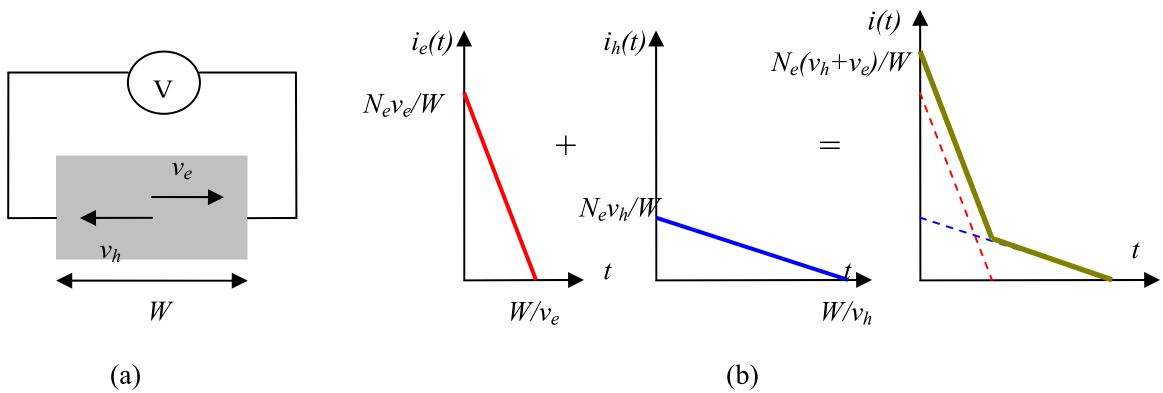

(a) (b)

Figure 2.2 Illustration of the photocurrent contributions from electrons and holes (a) An electron-hole pair is generated in the photodetector (b) the electron and hole contributions to the photocurrent.

The photogenerated current is created by collecting the photogenerated carriers and each electron-hole pair induces one unit charge in the external circuit. When electron-hole pairs are generated uniformly throughout the active region, as shown in Figure 2.2 (a), their respective contributions, in 1-D case, to the current with respect to time can be depicted as in Figure 2.2 (b). The initial fast decay corresponds to the fast electron sweep out, and holes yield the main contribution to the photocurrent at later times. Hole current can be neglected in evaluating the pulse width but it does influence the evaluation of the bandwidth significantly. The details will be addressed in Section 2.3.2.1.

The transient current response and the corresponding frequency bandwidth is determined by several factors, the major ones are the interdigital distance, the electric field strength, the absorption layer thickness, and the excitation density.

Geometries of the device electrode: The interdigital distance, namely gap between fingers, is one of the major factors that influence the dynamics of the MSM structure. As we mentioned in equation (1.2), the bandwidth is inversely proportional to the distance of the electrode, where $D \cong \sqrt{d^2 + W_g^{\ 2}}$, W_g is the gap distance between the fingers and d is the thickness of absorption region. In the real response, the FWHM is more related to W_g and d affects the tail more. An empirical formula of the pulse width of transient current response in MSM structure can be approximated with [50], $FWHM = L_g / 1.06 \times 10^7 + 0.26 ps$, where L_g is the finger separation in unit of cm, and the first terms $L_g / 1.06 \times 10^7$ is calculated with a unit of second. The current pulse narrows noticeably if the finger separation is reduced to 0.5-μm [51].

Background doping: For the unintentionally slightly n-doped absorption region, the holes tend to stay near the surface because of the surface field. The same field pulls electrons into the bottom low

field regions. Case is reversed for unintentionally p-doped absorption region. Hence, the unintentionally p-doped material exemplifies sharpened peak and ever slowly decayed long tail.

Incident intensity: At modest intensity, the presence of the charged particles does not noticeably modify the spatial field distribution in the device. As the intensity exceeds a certain threshold, the electron and hole populations do not separate as easily as in the low excitation case and the dynamic response changes drastically. The photogenerated carrier population thus is large enough to screen the externally applied field by the space charge fields created from the initial spatial separation of the electrons and holes. In this case, the significantly reduced fields slow down both types of carriers and the electrons and holes both contribute to the slow tail of the time response rather than the holes alone in the case without screening.

External bias: The screening effect discussed above becomes an even more severe problem for low external bias, where the weak internal field gets immediately screened even by the relatively low intensity of photon injection. In this case, electrons and holes migrate by diffusion rather than the drift thus there is no difference for electron and hole current in terms of rate of collection.

Surface charge: Due to the surface states at the top of semiconductor material, carriers trapped there create surface charge layer, hence a space-charge region in the body[34]. Inside the space-charge region, a strong “aiding” field accelerates electrons towards the bulk just beyond this region, a strong “retarding” filed sweeps the electrons toward the surface. As a result, the electrons generated inside the space –charge region are repelled from the surface by the surface charge, creating internal field which, in turn, cancels the field from surface charge. Consequently, the initial decay due to the electron contributions broadens in accordance with the surface charge density.

2.2 Experimental Results of the 2DEG Device

2.2.1 2DEG Device Structure, Design and Fabrication

An AlGaAs/GaAs based resonant-cavity-enhanced (RCE) Heterostructure MSM (HMSM) photodetector with $Al_{0.24}Ga_{0.76}As/Al_{0.9}Ga_{0.1}As$ Distributed-Bragg-Reflector (DBR) was fabricated and characterized. The wafers were grown by IQE, Inc., and the fabrication was performed at Consiglio Nazionate delle Recerche (CNR)/Istituto per la Microelectronica ed I Microsistemi (IMM) in Italy.

The HMSM-PD is constructed on GaAs material system for 850-nm wavelength detection. The basic layer structure is shown in Figure 2.3. On a GaAs substrate, 15 pairs of quarter wave $Al_{0.24}Ga_{0.76}As/Al_{0.9}Ga_{0.1}As$ DBR is built on a GaAs buffer layer. Growth is followed by an active GaAs absorption region with unintentional p-type doping. The thickness of the absorption region is prepared to be one half of the effective wavelength given the refractive index of the absorption material. In this way a resonant cavity is established to improve the external quantum efficiency hence the responsivity of devices for wavelengths of interest.

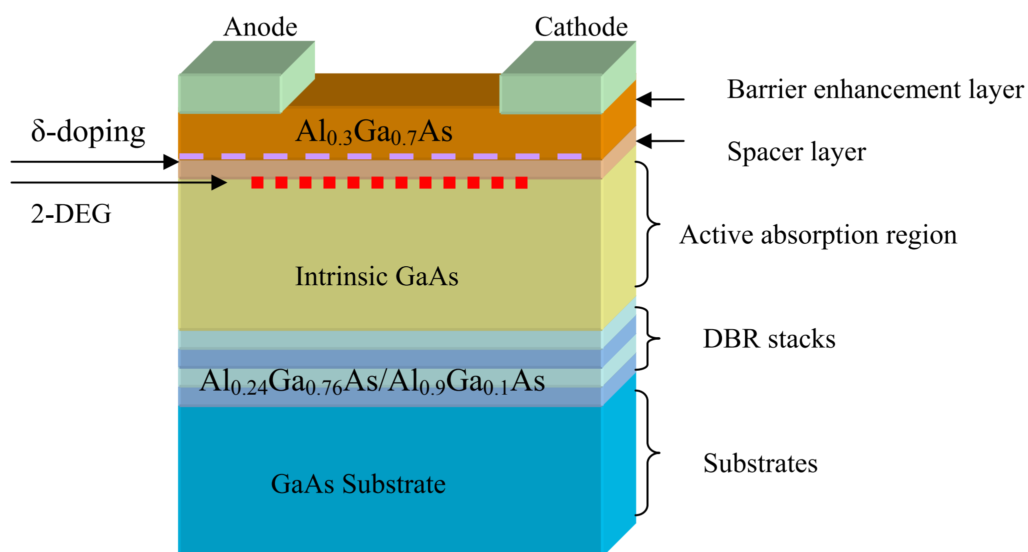

Figure 2.3 Schematics of the cross section of the 2-DEG based MSM photodetector.

An intrinsic $Al_{0.3}Ga_{0.7}As$ layer covers the active absorption region. It is employed to enhance the Schottky barrier height, as well as reduce surface recombination velocity. We term this an "undoped" device. A δ-doped structure was also produced by adding an additional highly n+ doped thin atomic planar doping layer, namely a δ-modulation doping layer into the $Al_{0.3}Ga_{0.7}As$ layer with a 5-nm of spacer layer away from the AlGaAs/GaAs junction. The DBR, absorption layer, barrier enhancement layer and air constitute a resonant Fabry-Perot (FP) cavity with two mirrors, DBR and air, at both ends for optical confinement of selected wavelength. In the device fabrication, metal electrodes are deposited on the top to create Schottky contact, and the anode and cathode forms interdigitated fingers. The interdigitated fingers of metal contact are illustrated in Figure 2.4, where, *L* is length of fingers 40-μm, *W* is the finger width, 1, 2-μm, and *G* represents the finger separations, 2 or 4-μm. The active region is about 40x40 μm^2. The device with the doped structure has been reported [35] as having a low dark current due to enhanced Schottky barrier height, high wavelength selectivity due to the bottom DBR mirror and resonant cavity, and above all, high speed performance up to 33-GHz is achieved[35].

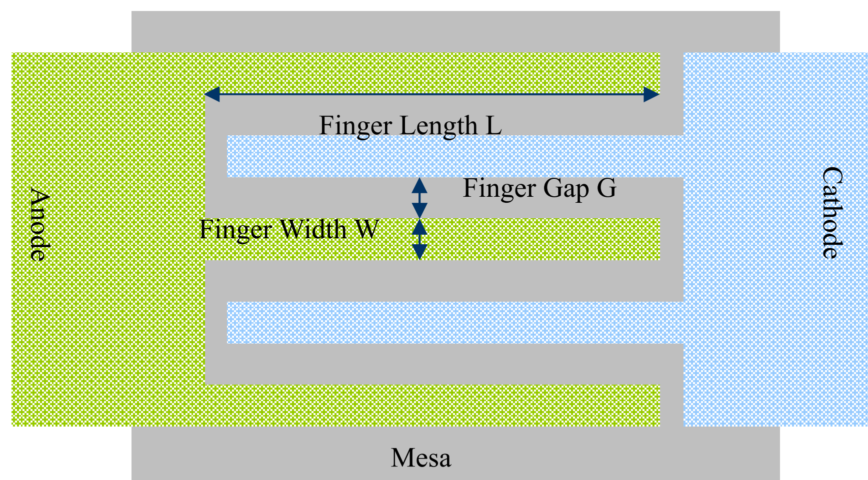

Figure 2.4 Illustration of the interdigitated MSM electrode Patten. Active region is built on a mesa top.

2.2.2 Experimental Evaluations of the Time Response

The experimental results such as, the dark current, the current spectrum, the reflectivity, etc., have been presented in [63] in detail. Here we are more interested in the time response of the device. The high-speed response was measured using a mode-locked Ti:Sapphire layer operation at a repletion rate of 76-MHz at wavelength of 850-nm. The time domain and frequency domain response are depicted in Figure 2.7 respectively. Figure 2.7 (a) shows a transient response of the device with a dimension of finger width of 1-μm and finger gap of 4-μm under external voltage of 20-V. The time response shows a FWHM of 8.1-ps, a rise time of 8.8-ps, and a fall time of 9-ps. Fourier transform generates the corresponding response in frequency domain, as shown in Figure 2.7 (b), where a maximum bandwidth is observed around 33-GHz.

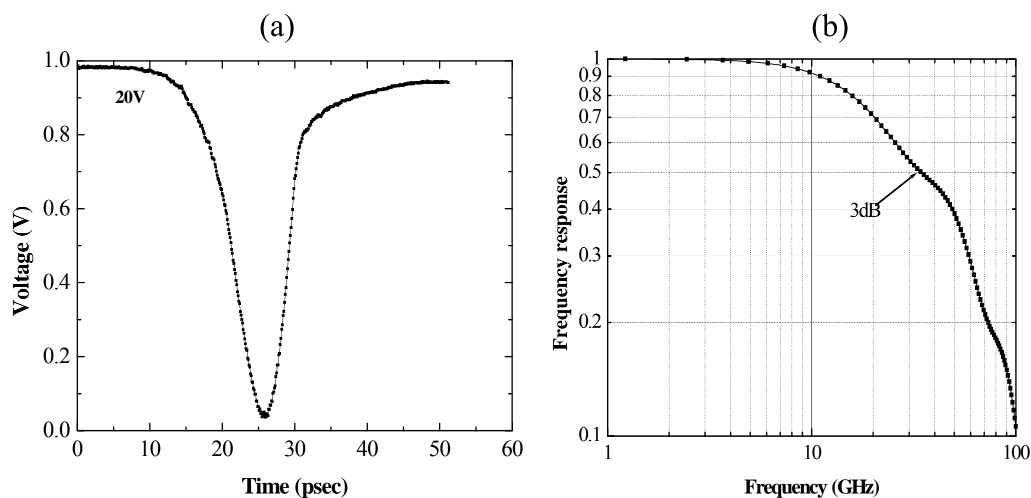

Figure 2.5 The transient current response of the 2-DEG MSM photodetector in time (a) and frequency domain (b) [63].

Several time response data from different electrode geometries are listed in Table 2.2.

Table 2.2 Performances of the 2-DEG device at different electrode configurations.

Contact Width, Gap (μm)	Amplitude low-doping (a.u.)	Amplitude high-doping (a.u.)	FWHM low-doping (ps)	FWHM high-doping (ps)	Cut-off frequency low doping (GHz)	Cut-off frequency high doping (GHz)
1,2	0.218	0.239	8.682	7.739	26.9	30.5
2,2	0.262	0.364	8.790	7.744	29.3	33.0
1,4	0.185	0.216	8.226	7.311	34.2	24.4
2,4	0.157	0.218	9.259	8.153	28.1	31.7

We see from the table that, the time response of the high-doped device exhibit larger amplitude, narrower FWHM and higher cut-off frequency. The most intriguing observations from above tables for the time response of doped devices is that the FWHMs for finger gap of 4-μm is close to that of the finger gap of 2-μm device, which is contradictory with what is predicted for MSM structure photodetector, that is the dynamic response is inversely related to the finger separations. According to the empirical formula we introduced in the previous section $FWHM = L_g / 1.06 \times 10^7 + 0.26 ps$, a rough estimation of the FWHM for 4-μm device is about 1.99 times larger than the 2-μm one for conventional MSM structure. Here we observe a difference in FWHM of around 5% between the 2-μm and the 4-μm device. The observation leads us to explore the particularity of the δ-doped MSM structure from conventional MSM structure. To solve the issue, we performed static and dynamic simulations regarding both doped and undoped devices. The simulation results reveal a vertical field facilitating the electron transport in the δ-doped MSM structure, which eventually motivates the research on slow carrier dynamics aiming at alleviating the long tails in the time response due to the slow holes.

2.3 Static and Dynamic Simulation Results

The electrical properties were simulated with commercial available software Integrated Systems

Engineering (ISE)-Technology Computer-Aided Design (TCAD) software. The major package we used is the device simulator DESSIS. It is a multidimensional, electro-thermal, mixed-mode device and circuit simulator for one, two and three-dimensional semiconductor devices. It incorporates advanced physical models and robust numerical methods for the simulation of most types of semiconductor device on a variety of materials. Our simulation used the hydrodynamic models, where the carrier temperatures differ from the lattice temperature. It accounts for energy transport of carriers. The major partial differential equations (PDEs) to be solved are the Poisson's equation, the electron/hole continuity equations and the energy conservation equations for electrons, holes and the lattice.

The dynamic behavior was simulated by Ramo's theorem [22], which was fed with the static two-dimensional electrical field profile and creates the time dependent photocurrent response from electrons and holes respectively. In what follows we will describe each component of the simulation analysis.

2.3.1 Static Behavior

The top electrodes of the MSM structure consists of anode and cathode in a interdigitated configuration, illustrated in Figure 2.6(a). Due to this repetition feature of the geometry, the structure of interest can be divided into several unit cells, as shown in Figure 2.6(b), the cross section cut from where Figure 2.6(a) is indicated.

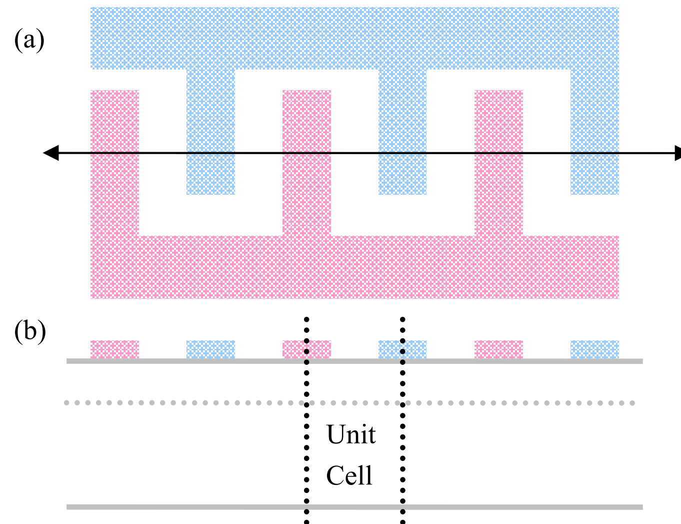

Figure 2.6 Illustration of cross section of an interdigital structure for simulation. The region between two dot lines is one unit cell for simulation.

In all the simulations, we only take one unit cell for calculation and apply a symmetric boundary condition for that unit cell. The selected unit cell is divided in a rectangular mesh. The motion of electrons and holes are both calculated in this mesh. The schematic diagram of simulated mesh grid in a unit cell is shown as in Figure 2.7. More mesh points were used around the heterojunction.

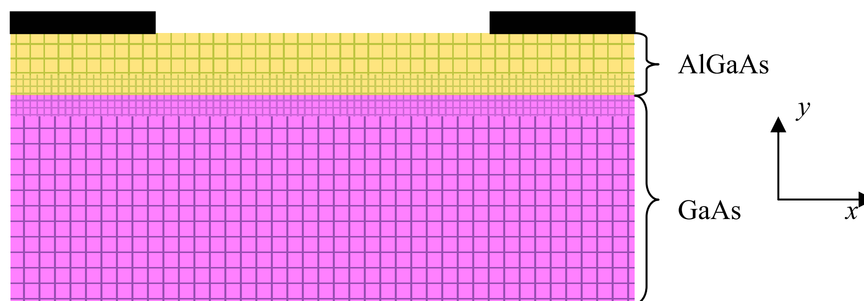

Figure 2.7 The schematic diagram of the mesh grid for the device simulation. Coordinates of *x-y* plane is given.

The δ-doped AlGaAs/GaAs heterostructure MSM photodetector was simulated. For the purpose

of comparison the undoped and CMSM structures have also been simulated under the same condition. The simulation employs geometry with finger width of 2-μm, finger gap of 2-μm (W2G2), and thickness of the active region of 1 μm. For better presentation of the simulation results considering the length and depth of the device, the thickness of active region is chosen larger than the real device. The eventual results have minor difference in terms of the background carrier distribution but major electrical properties will be kept unchanged. On the other hand, since we are interested in the electrical properties of the structure rather than the optical wave propagation in the device, the DBR layers were not included. The potential at the boundaries except the top assumes zero gradients, where there is no normal current component. The Schottky barrier height is 0.7 V, thus the contact potential is $V_{sc} = -0.7\ V$ at the cathode, and $V_{sa} = Va-0.7\ V$ at the anode, where, Va is the external applied bias.

Conduction Band: Figure 2.8 is the three dimensional view of the conduction band for CMSM, undoped and δ-doped structure at 5-V bias. The inset coordinates give the perspective view, x direction indicates the length of device, y the depth, where the layer information is provided, and z the conduction band energy through the device. A significant difference between δ-doped structure and undoped/CMSM is the potential drop along the x direction is step-like in δ-doped structure, rather than a uniform downward slope from cathode to anode in undoped/CMSM ones.

The MSM structure with Schottky contacts is essentially two diodes with back-to-back configuration. A large fraction of applied bias is expected to drop across the reverse junction and the rest across the forward before the critical point of flatband is reached [58]. In the Figure 2.8, the band bending of Conventional MSM (CMSM) at two contacts are opposite, suggesting that the applied voltage has exceed the flatband, and the whole sample is totally depleted. With the same bias applied on undoped structure, the reverse bias depletion region extends to the anode, but is not able to reach

the region under forward Schottky contact due to the relatively high electron concentration there. Intuitively, it is clear that it would take more effort to deplete a higher concentration of carriers.

However, for δ-doped structure, the case is quite different. A highly concentrated 2-DEG exists along the entire interface. Due to the high electron concentration, it is difficult for the depletion region to extend into the 2-DEG. In 2-D case, the depletion length is given by[64], $d_{2d} = 2\varepsilon(V_{bi} + V_a)/qn_s$, where d_{2d} is the width of depletion, V_{bi} is the built-in potential of the junction, V_a is the applied bias, n_s is the 2-D carrier density. A rough estimation of the 2-DEG concentration of $2.5\times10^{12}/cm^2$ provided the δ-doping level of $5\times10^{12}/cm^2$ gives a depletion width of 0.057-μm at voltage of 1-*V*. In 3-D case, the relationship of the depletion width with the doping level is given as $d_{3d} = \sqrt{2\varepsilon(V_{bi} + V_a)/qn_v}$, where n_v is the 3-D carrier density. Given a background unintentional doping level of around $1\times10^{15}/cm^3$, the width of depletion is around 1.57-μm at V=1-V. The extension of the depletion region in the 3-D absorption region is much wider than in the 2-DEG given the same voltage applied.

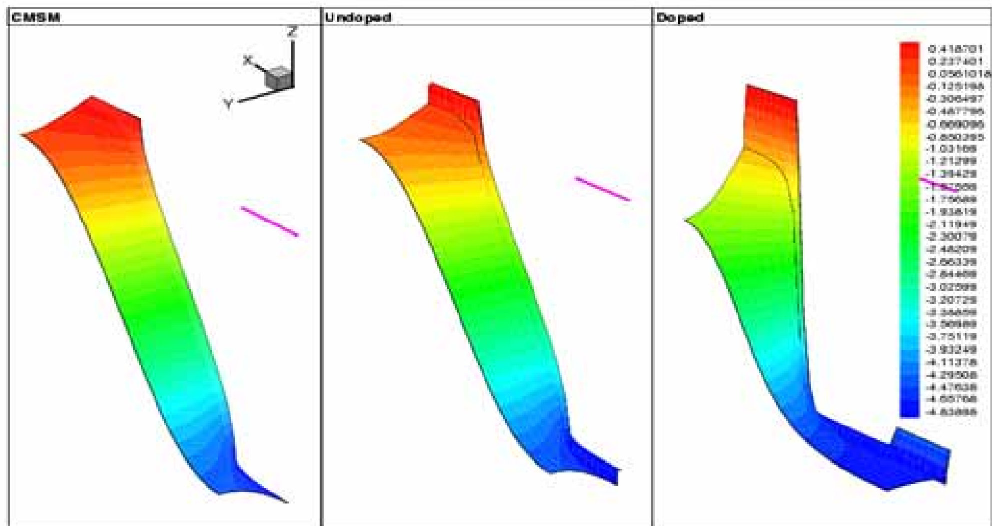

Figure 2.8 Three dimensional view of static conduction band for the δ-doped (right), undope HMSM (middle) and conventional MSM (left). The contact at left is cathode, right is anode.

The potential experiences an abrupt drop in lateral directions as we see in the Figure 2.8 since the depletion region extends vertically due to the 2DEG with high electron concentration. In other words, most of the channel between the cathode and anode has the same band bending expected from a HEMT device, with high electrical field in the transverse direction, and not strongly affected by the lateral field due to contacts. The lateral potential drop looks more a step like in the region close to the 2DEG compared to deep into the device. At the bottom of the device, the abrupt change is almost smeared. We also found that the regions under and close to the anode are not depleted, which is indicated by the polarity of the Schottky barrier, and obvious forward bias, in the anode.

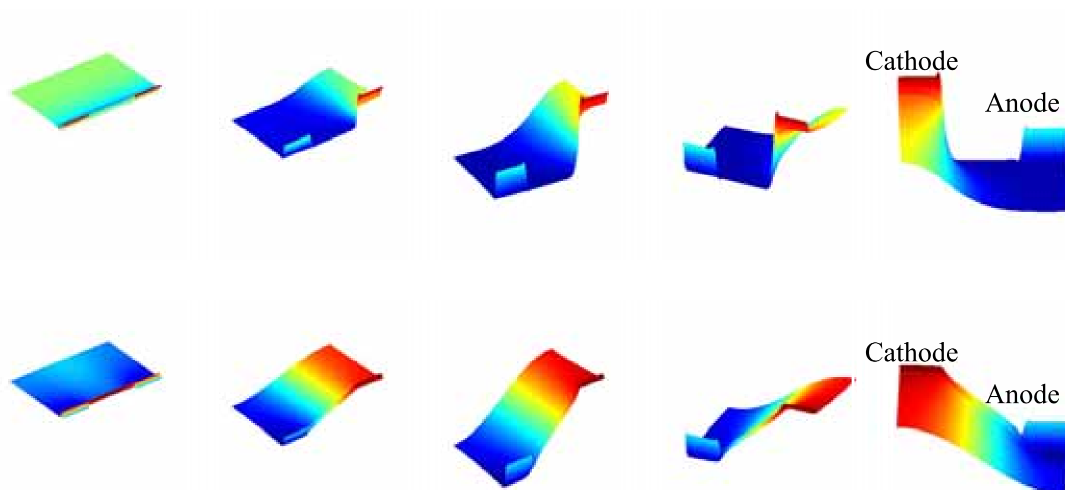

Figure 2.9. The evolution of the conduction band with external voltage for doped (upper row) and undoped device (bottom row). The external voltages applied from left to right are 1, 2, 3, 4, 5-V respectively for both upper and bottom rows.

The potential behavior can be better explained with the two dimensional potential evolution with external voltage. Figure 2.9 shows the doped and undoped device subject to external voltage of 1 to 5-V at a step of 1-V under different perspectives of view. The development of the two dimensional

potential profiles are clearly presented in this figure for both doped and undoped structures.

Electron Concentration: Figure 2.10 compares the corresponding electron concentration in the undoped and the δ-doped structures. The distributions of electron concentration for both doped and undoped structure are obtained from the self-consistent 2-D conduction band profile.

In undoped structure, even though the carrier concentration at the interface is higher than in the bulk, the electrons are far beyond confinement, since AlGaAs and GaAs layer are both undoped, and carrier transfer is only due to the difference in electron affinity.

However, a prominent contrast can be observed in the δ-doped structure, where, the 2DEG is evident due to the strong energetic pull transferring electrons from high bandgap, the δ-doped layer, to the low bandgap material side of the interface. The 2DEG layer is well confined within a distance of about 100-Å. As stated in previous section, the high electron concentration at the heterojunction screened further extension of the depletion region in the 2-DEG.

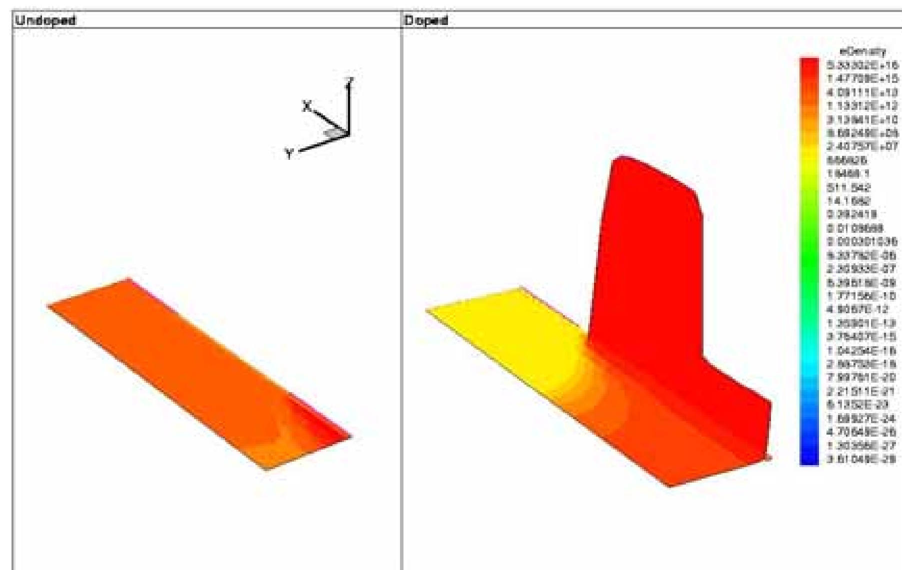

Figure 2.10 Three dimensional view of static electron concentration for the δ-doped (right) and the undoped HMSM (left). Cathode is at the left; anode is at right. High concentration of 2-DEG exists even under the lateral bias. Coordinates are the same as Figure 2.9.

The argument of the existence of 2DEG is found valid by examining the detailed conduction band of the doped sample. Figure 2.11 shows cuts of the conduction band along the direction of growth. They are respectively from cathode, anode and the middle of the device. We can find a well defined triangular potential well at the interface from *x=0* to *x=100 Å*, existing underneath the anode and the middle of the device. The first small notch is where the δ-doping layer is located. The Fermi level is calculated and suggests the energy subbands in the triangular well are populated, while the δ-doping layer is fully depleted. It conveys a piece of information that no parallel conduction occurs at the δ-doping layer. This implies good design since the parallel conduction is undesired in the detector as it creates leakage current in the dark.

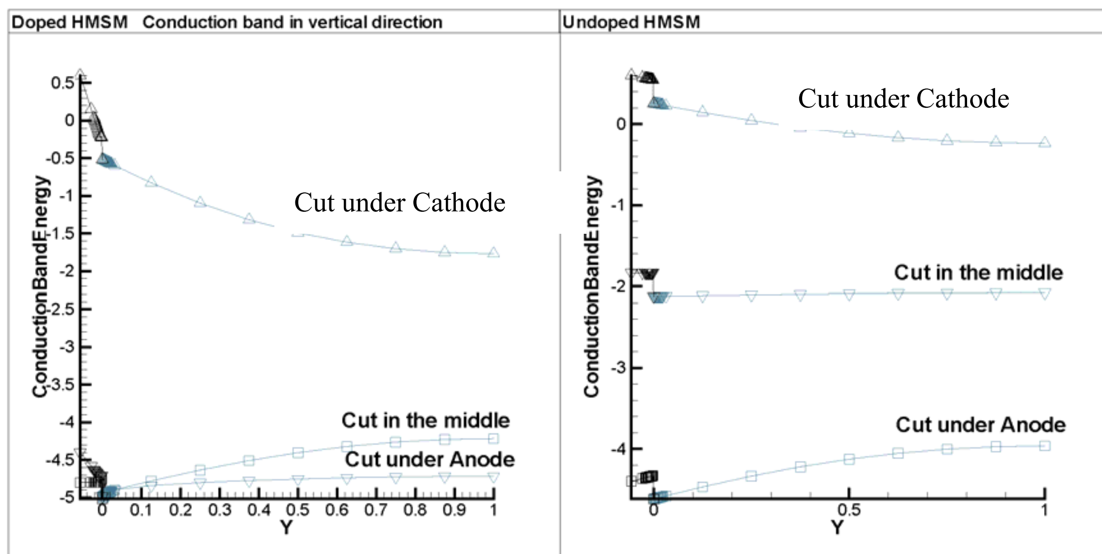

Figure 2.11 Three cuts of the conduction band along the direction of growth for the δ-doped (left) and undoped device (right).

It is the existence of 2DEG that significantly changes the dynamic behavior of the device. It is well known that a homogeneous conductor realizes a constant potential and provides a perfect shield

against the quasi-static electric fields due to its great accommodation ability to the electrons. To some extent, the 2DEG layer with a high electron concentration can be considered a sheet of conductor, though not an ideal one due to limited density of states with little potential variation within it. The 2DEG plane shields the lateral component of the electric field for the active region, in other words, the lateral electric field in the region below the 2DEG layer is not subject to the influence of the field above which is introduced by applied bias. The detailed screening effects of 2DEG are discussed in [65]. The results of the screening effect is that it changes the two dimensional potential distribution hence the field orientation in the active region as we discussed previously.

Electric Field: Electric field distribution is particularly important for MSM because it is the key parameter having influence on the average transit time of carriers. Figure 2.12 shows two dimensional field distributions.

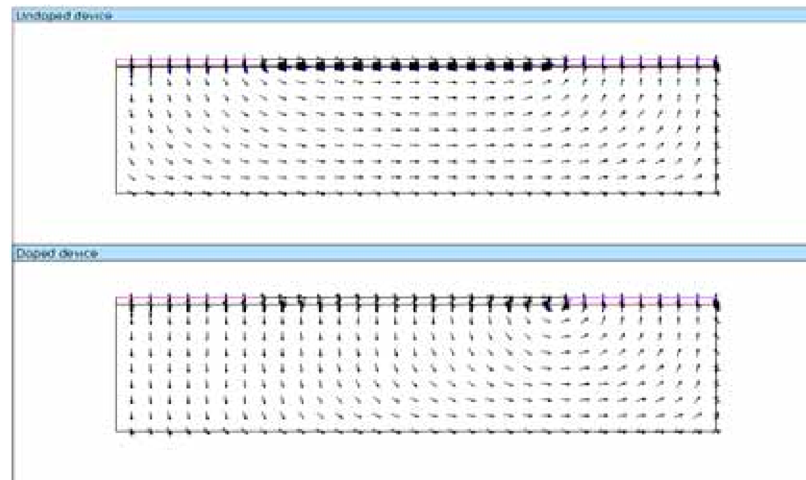

Figure 2.12 Two dimensional electric field distributions for the δ-doped (bottom) and undoped device (top).

It is observed that in the undoped device, the electric field is more symmetrically distributed

which is consistent with expectation because of the uniform drop of potential between the anode and the cathode. As far as the direction is concerned, the field in the undoped device is oriented horizontally in the bulk of active region. In contrast, the δ-doped device presents a relatively vertically oriented field, which is gradually led to the lateral direction when approaching the bottom of the active region. The vertical field under the anode looks more evident than under the cathode, which is consistent with conduction band profiles recalling that the abrupt drop of potential occurs at the cathode side. Following the electric field, electrons travel straight upward to the 2DEG in the doped device rather than move laterally first and then upward to the contacts in the undoped device. Having reached the 2DEG, electron's motion is greatly facilitated by the fact that they are majority carriers, that is, this sheet of carriers can be treated as quasi equipotential conductor, which shields the lateral component of the electric field in the active region. Therefore, only the vertical field is developed in the region below the 2DEG. It should be mentioned that the same electric field forces the holes deeper into the device; hence the tail of response is adversely affected. Ways of enhancing the hole transport must be explored further.

Since the δ-doped device assumes a vertical rather than a lateral field in the undoped device, we are able to analyze the trajectory of photogenerated carriers. The transit times for two structures, viewed as an average time spent by carriers traveling from where they are generated to the contacts, are found to be different according to the various geometries. The δ-doped device favors the geometry configuration with small depth and is not sensitive to the gap, and vise versa in an undoped device small gap is favorable. For our device, with a finger gap of 4-μm and depth of 118-nm in the active region, the δ-doped structure has obvious advantages over the undoped one. As mentioned above, structures with small depth are easier to fabricate than with small length. Large finger gap devices

expose more area uncovered by the electrode thus allow more radiation coupled to the device directly without suffering the reflection loss due to electrodes. Provided the larger finger gap devices have the same dynamics with the small finger gap ones, we are able to keep the speed of the device with enhanced quantum efficiency and responsivity by design of larger finger separations.

Detailed simulation shows a strong field toward the interface, around $1.6\text{x}10^5$ *V/cm*, existing in the 2DEG layer and fading rapidly within 100-Å in the δ-doped device. Apart from that, the maximum electric field, regardless of direction, occurs at the region under the cathode, and it decreases gradually to the anode as well as to the bottom. However, the maximum field in the undoped device is located in the middle of the sample, and fades somewhere in the region under contacts. The average values of the electric field are comparable for two samples in the active region, and most of the time, electrons travel at the saturation velocity. The static field and potential thus found are used next to calculate the dynamic behavior of optically generated carriers.

2.3.2 Dynamic behavior

2.3.2.1 Introduction of Ramo's theorem and its validation

In simulation, there are two methods fore determining the photocurrent. First is that the instantaneous current taken by electrode is counted in proportional to the number of the electrons received by the electrode per second. The current in external circuit due to one unit charge is counted once both carriers from an electron-hole pair reach their respective electrodes. Second is the that current in external circuit is induced as soon as the carriers are generated and separated from each other, and start to move at certain velocity. In this way, the current is created as long as carriers approach to the electrode, not necessarily reaching it. The contribution of one unit charge to the photocurrent is accumulated step by step with respect to time by each movement of the carriers until

they are collected by the electrodes, rather than in the first case, one unit charge is counted when and only when the electron-hole pair reach their corresponding electrodes. Figure 2.13 illustrates the two methods of counting of photocurrent as one electron-hole pair is concerned. In the Figure 2.13 (a), the electron hole pair is generated at $x=a$. The first method counts the charge in the current as a whole after a certain delay, which is the transit time spent by the carrier in the material, as shown in Figure 2.13(b). The second method counts the current during the whole transit process, as shown in Figure 2.13(c).

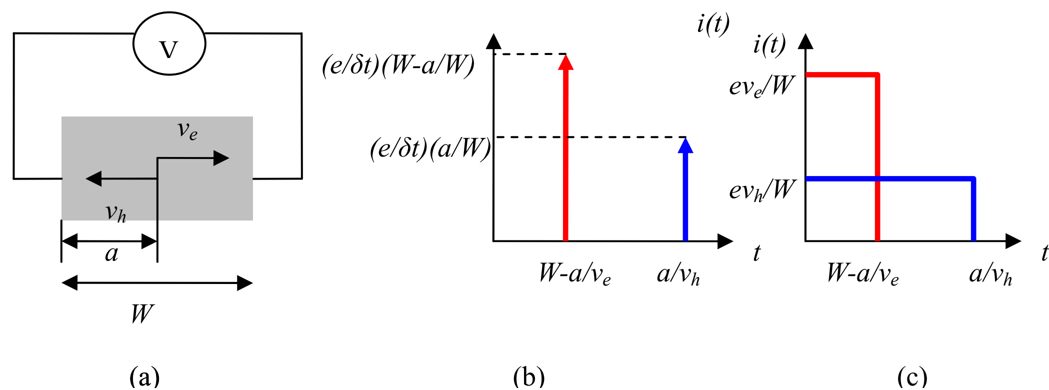

Figure 2.13 (a) Illustration of the photocurrent in structure by (b)Counting current by charge collection at the electrode (c)Counting current during the whole transit time.

Ramo's theorem defines current using the second method. The external circuit induces photocurrent once the charge in the bulk of the detector moves at a certain velocity. This particular process, namely, the external circuit sensing the movement of the carriers in the semiconductor material, takes a dielectric relaxation time, σ / ε [66], where σ is the conductivity of the medium, and ε is the dielectric constant. This parameter reflects the speed of response of the semiconductor material to the external electrical field and relates to the dielectric properties of the semiconductor

material. The complete delivery of the charge to the external circuit by movement of carriers in the photodetector takes an extended time, which is the transit time, spent by the carriers from where they are generated to the corresponding electrodes, in the bulk material of the semiconductor photodetector.

This method of counting the current has an inherent merit of being able to show the quanta effects by counting fractions of one unit of charge at a time, namely, electrons are treated as quanta of charge. In this way, the behavior of the individual quanta is presented directly rather than through moments of a statistical distribution [67].

Major simulation methods employed to study the time response of the photodetectors, are Ensemble-Monte-Carlo (EMC) treatment [50, 51], quantum mechanical treatment [49, 53] and transport based on Ramo's theorem [52].

The EMC method [68-70], providing the exact numerical solution to the Boltzmann transport equation, is a complete analysis of transient carrier motions, which is able to incorporate the band structure of the materials and microscopic models. Characteristics of the time response of an MSM have been systematically reviewed in [51]. Detailed dynamic behavior analysis has been made by employing two-dimensional Monte Carlo simulation, as studied in [51, 71], with the help of the energy band structure of material and scattering mechanisms in the material. This method is particularly accurate and useful for cases involving non-equilibrium dynamics, where the carrier-carrier scattering events have to be incorporated. However, these methods are relatively complicated and time consuming in studying the behavior of the device.

It has been shown [49] that the a quantum mechanical treatment using numerical solutions of time-dependent Schrődinger equation as the dimension of the structure under investigation goes below 100-nm is required, since the sizes of electrons and holes are not negligible any more compares to the

finger separations. The carriers are better to be represented by the Gaussian wave packets rather than the single particles. At regimes without quantized size effect, quantum mechanic treatment does not yield results of interest. Considering our case, the dimension under investigation of the absorption region is around 4-μm in length, which is able to avoid the necessity of quantum mechanic treatment.

Ramo's theorem is clear and straightforward in principle. Its realization in a real device is relatively simple and effective compared with the methods discussed above. Even though Monte Carlo proves itself a comprehensive way of simulation approaching the real case in terms of physical mechanisms, Ramo's theorem is adequate for our device simulation so far as the intensity of incident photons does not reach the saturation level; a behavior that can be verified from linearity responsivity measurement. Even if intensity saturation is reached, it can be self-consistently included by modifying the static field due to changes caused by separation of optically generated carriers. On the other hand, the applied voltage does not create high field effect, and the level of carrier concentration in the absorption region is low, which also rules out the need for complex EMC method in the simulation of absorption region due to its large computation and time consumption. We should note that by using Ramo's theorem, only drift current is taken into account, which is accurate for MSM absorption region simulation because the diffusion component is small compared with the drift component, thus it plays a minor role in carrier transport. The results from Ramo's theorem for MSM simulation have been shown to be comparable to Monte Carlo results with much reduced computation complexity [52].

2.3.2.2 Model description

Ramo's theorem was first proposed in 1930's [22]. Its one dimensional application for current calculation is introduced in [72] and the two dimensional model was derived by equating the work done by motion of charge, $-q\vec{E}dx$, with the energy provided by the external circuit, $i(t)Vdt$. The

formula can be written as [52] :

$$J_{ph} = \sum_{q} q\vec{v}(\vec{r})\frac{\vec{E}(\vec{r})}{V} \quad (2.5)$$

where, J_{ph} denotes the induced density of current, $\vec{v}(\vec{r})$ is the velocity of a moving carrier; it equals to $\mu(\vec{E})E$ at low field and saturates at high field. E is the component in the direction v of that electrical field which would exist at the electron's instantaneous position. V is the applied bias. The total induced current can be calculated by summing over all the charges, namely electrons and holes, in the active region. The equation involves the usual assumptions that induced currents due to magnetic effects are negligible. It should be noted that counting current by collection of electron-hole pair only take into account the current due to motion of electrons and holes. Ramo's formula incorporates the displacement current as when the self-consistent electrical field is included.

Ramo's theorem counts the current induced by carrier motion. An important concept implied here is that the carriers contribute to the current as soon as they move and do not contribute once they stop. Hence, in the δ-doped structure, when carriers move upwards to the 2DEG, they are stopped by a barrier, namely the conduction band offset between cap layer and active region. In this case carrier velocity equals zero and carriers do not make any contributions to the induced current. Also, total charge induced by electron-hole pair equal q when and only when both carrier types reach contacts.

Here we use the Ramo's theorem only in the absorption region. As photogenerated carriers reach the 2-DEG by following the vertical field, a different transport mechanism applies, which we will discuss in chapter 5.

The incident light is characterized by wavelength, power, as well as pulse width, which are used for absorption coefficient and light intensity calculations. In our simulation, we adopt the same parameters as our measurements, which are a wavelength of 850nm, power of 0.1-W from a

multimode optic fiber, and a pulse duration of 100-fs. Since the generation time is very small, at the fs level, we consider carriers to be generated instantly. The initial electron-hole pairs are distributed exponentially along the direction that the light is traveling through and uniformly laterally, that is,

$$\begin{aligned} n(y) &= n_0 \exp(-\alpha y) \\ n(x) &= const. \end{aligned} \tag{2.6}$$

where α is the absorption coefficient, and *y* is the depth of device.

2.3.2.3 Simulation results of dynamic behavior

Dynamic simulation is first performed by feeding the static two-dimensional electrical field vectors, which is exported from ISE simulation results along with the built-in mesh grids. Figure 2.14 presents the 2-D fields we used for simulation for both undoped and doped device in view of 3-D, 2-D and 2-D vector. The photocurrent is then calculated by summing over the contributions from every carrier while it is in motion according to equation (2.5). After each time step, the charge distribution in the unit cell is recalculated and updated. The field dependent velocity is employed [73]. The absorption coefficient model and field dependent mobility is incorporated in the simulation. Owing to limitations in computer power and capacity, the dynamic simulation of the transport is confined to a mesh grid of 200x21. The time evolution of electron and hole distribution for the undoped and δ-doped devices is shown in Figure 2.15 and Figure 2.16, respectively.

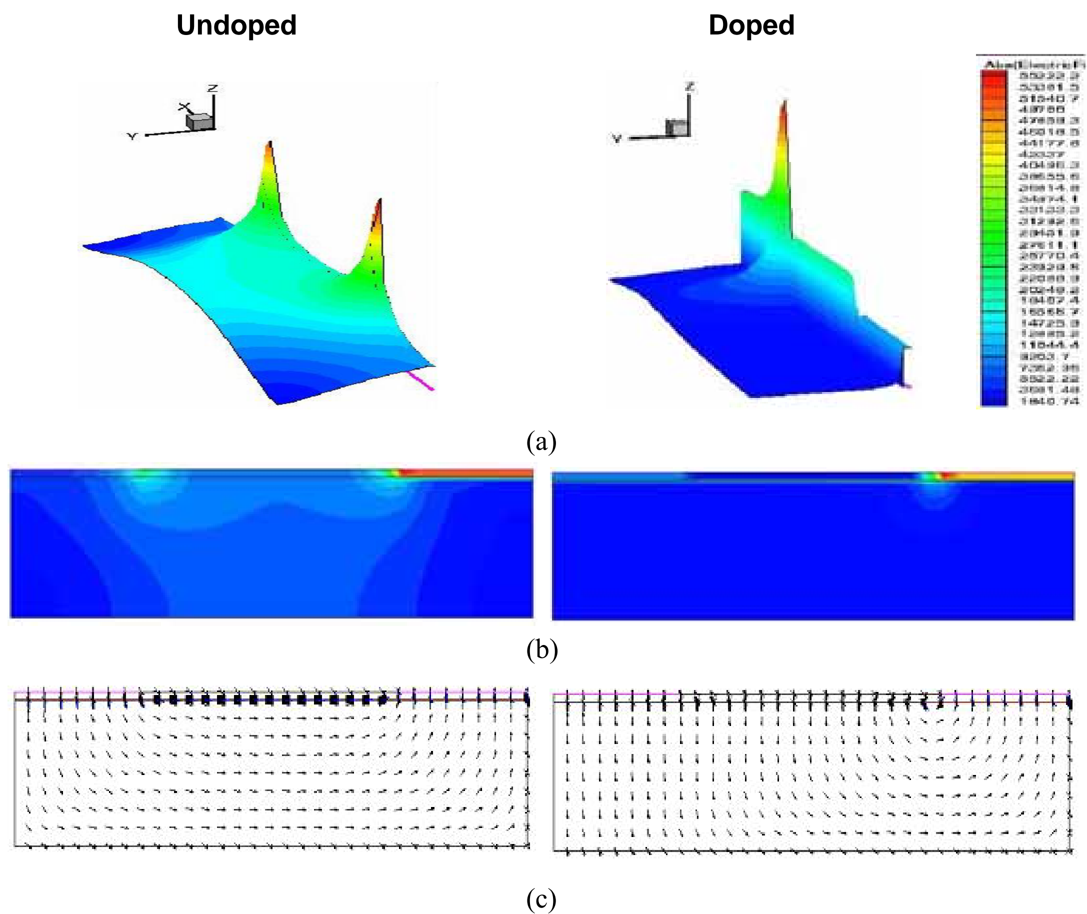

Figure 2.14 The electrical field used for dynamics calculation. Left column is for undoped device; right column is for doped device. (a) 3-D view of intensity (b) 2-D view of intensity (c) 2-D view of vector.

Two contacts are located at the top of each figure. Active regions start from $y=0$ to $y=1$ μm. The negative part of y axis is the barrier enhancement layer. The anode goes from $x=1$ to $x=2$ μm, and the cathode goes from $x= -1$ to $x= -2$ μm at the top of each figure. Electrons move toward the anode and holes move toward the cathode.

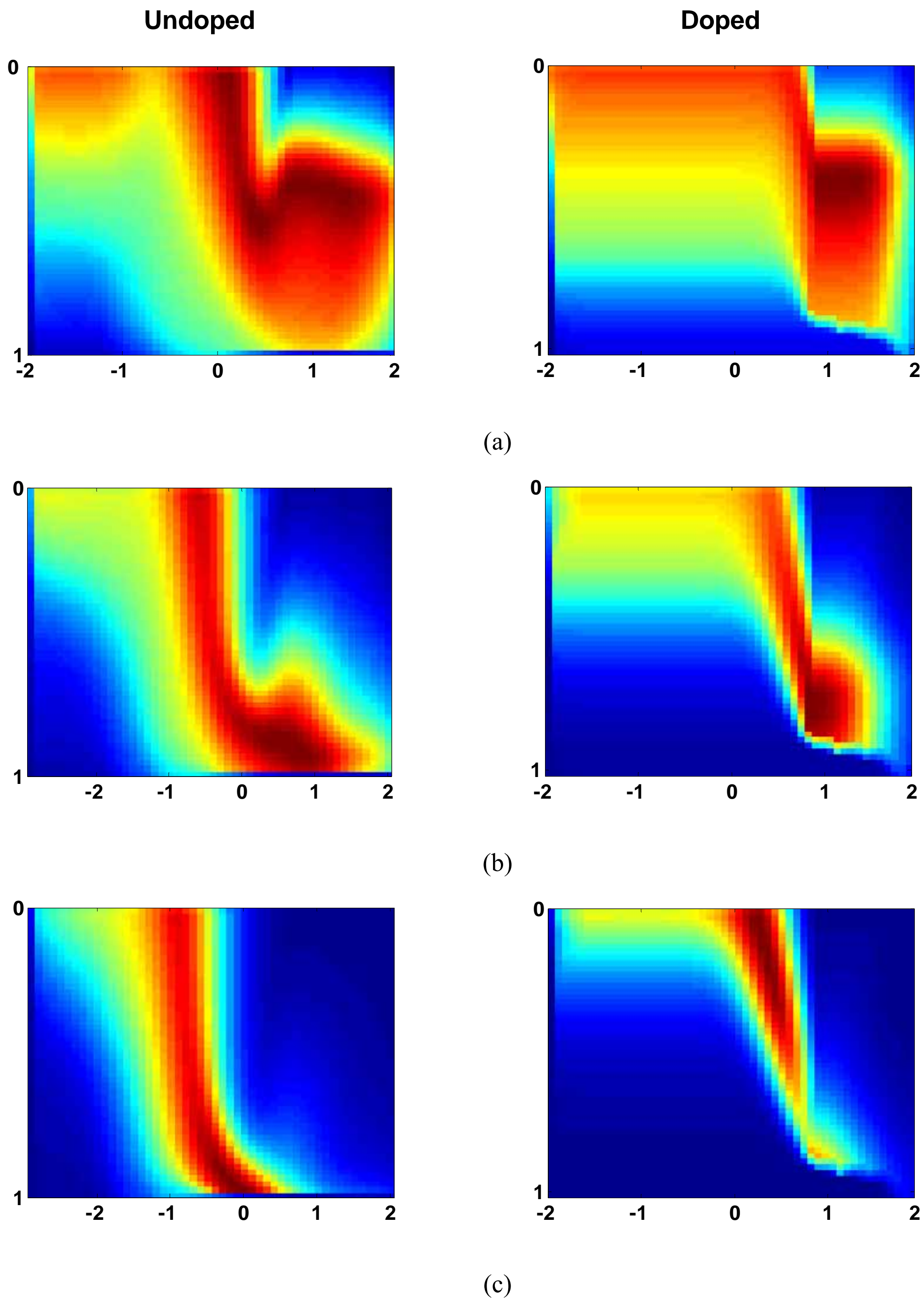
Undoped
Doped
0
1
-2
-1
0
1
2
(a)
(b)
(c)

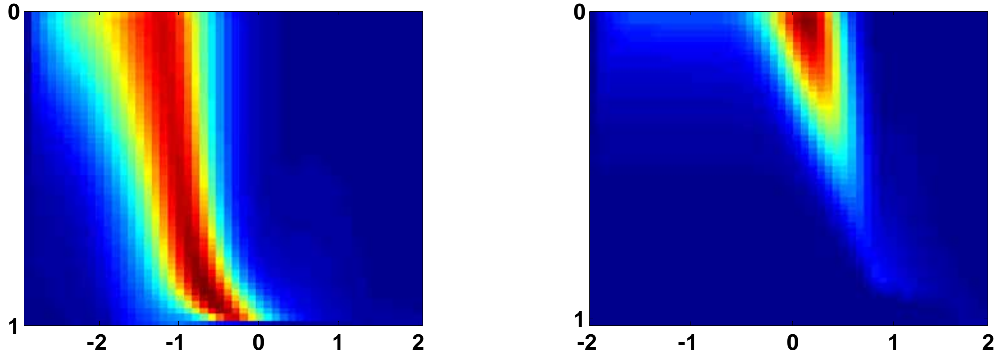

(d)

Figure 2.15 Electron distribution of undoped (left column) and doped (right column) W2G2 HMSM with 5V bias. There figures show the carrier distribution at (a)3-ps, (b) 6-ps, (c) 9-ps, (d) 12-ps intervals. (Scales in the figures are in unit of μm).

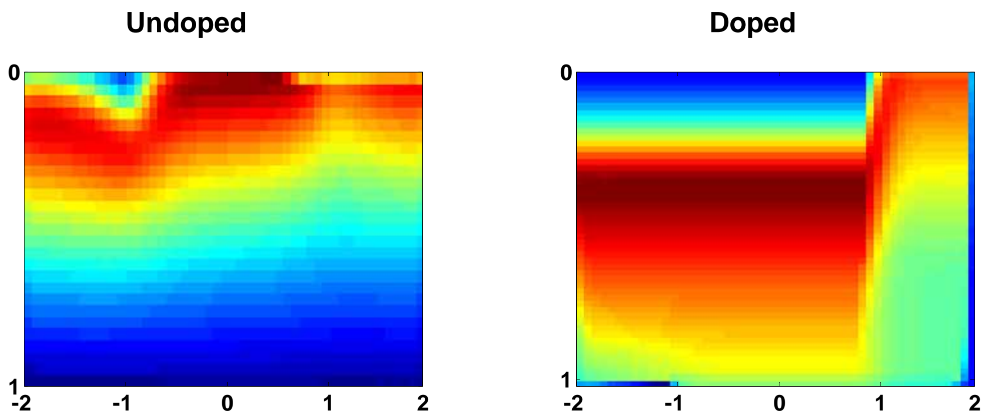

(a)

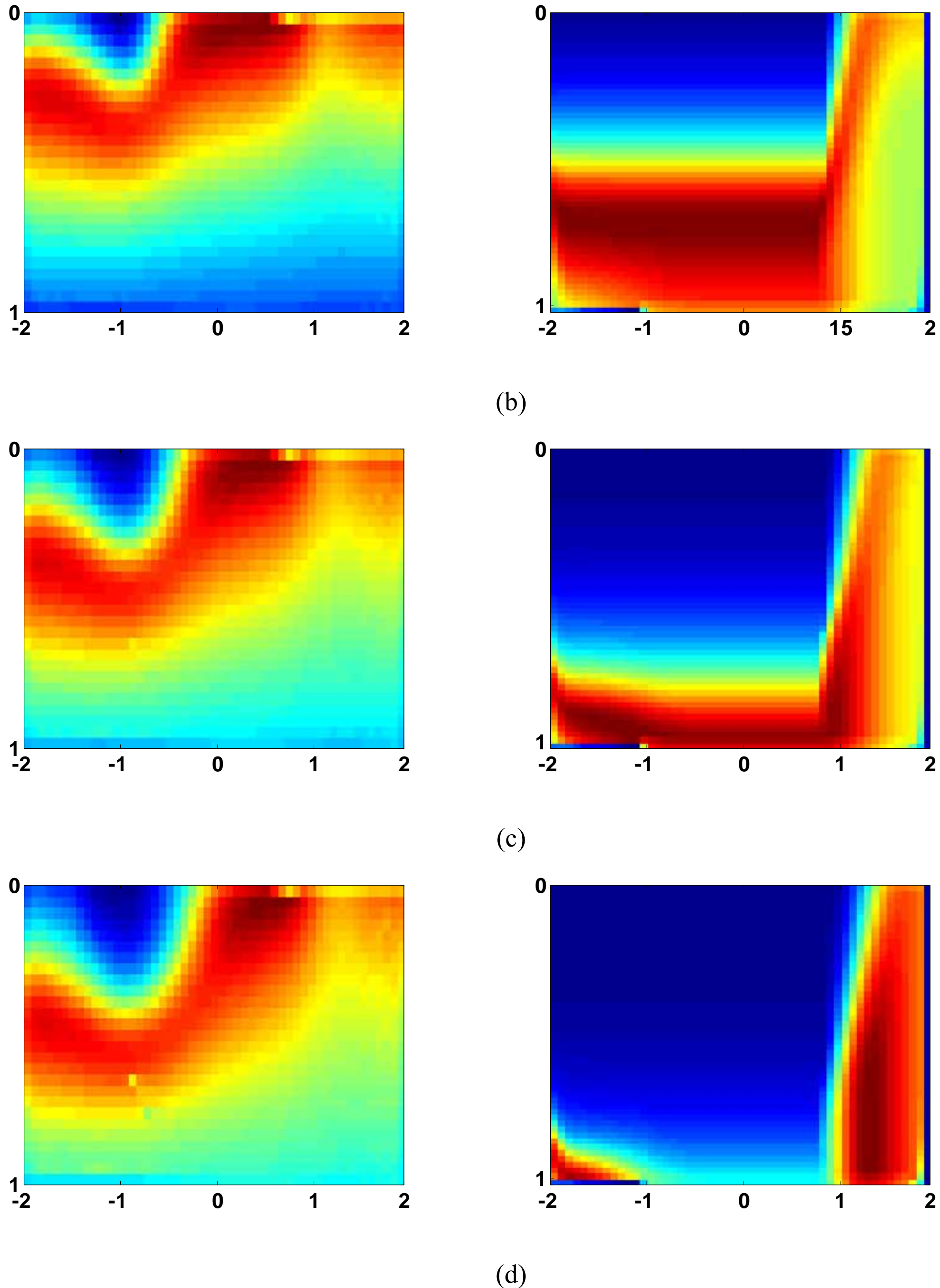

(d)

Figure 2.16 Hole distribution of undoped (left column) and doped (right column) W2G2 HMSM with 5V bias. There figures show the carrier distribution at (a)3-ps, (b) 6-ps, (c) 9-ps, (d) 12-ps intervals. (Scales in the figures are in unit of μm).

At t=0, electron-hole pairs are distributed in the active region with concentration decaying exponentially stated by the absorption model, not shown in above pictures. At t=3 ps, the electrons subject to the vertical field move directly upward to the anode in the δ-doped structure, however in the

undoped structure, electrons shift laterally toward the anode. Under the cathode region, electrons move downward in both doped and undoped structure and no great difference between them. In the undoped structure, at time interval of 6, 9, and 12-ps, we see a distinctive trend of motion of electrons laterally toward the anode. In the doped structure, electrons continue move upward. At t = 12-ps, only a small portion of electrons left in the device, rather than in the undoped structure, the electrons are still migrate laterally. This observation is due to the difference in lateral and vertical dimensions, 2 and 1 μm respectively in the simulation.

At t=3-ps, holes in doped structure move all the way down to the bottom of the device; in undoped device, the speed of the motion is not fast enough that holes only migrate a small distance away from the anode. One of the major differences from electrons is the speed of the holes are slower than electrons. During the same time interval, 3, 6, 9, 12-ps, more holes than electrons are left in the structure. In the undoped device, we observe nothing more than the slow migration, however, in the doped device, at t=12-ps, holes migrated to the bottom of the active region, and after that, they are expected to move all the way up to the cathode under the region covered by the cathode. This observation suggests a doubled distance of transit for holes in the doped structure, which inevitably results in extended tail in the time response.

This simulation thus shows the trajectory of carriers, which follow the field lines. It should be noted that at each mesh boundary a new velocity is calculated according to field-drift velocity dependence. The motion of charged carriers eventually creates the time response which will be shown below. From the above simulation, for the total transient time response, the major contribution comes from electrons at first, and then holes since electrons move faster than holes and are collected earlier. This dependence suggests that the dynamic behavior is mostly determined by the characteristics of

electron dynamics at the first several picoseconds, after that hole dynamics dominate.

Charge motion in the device leads to current conduction in the external circuitry according to Ramo's theorem [22]. Individual component of current due to electrons and holes, as well as total current is shown in Figure 2.17, comparing δ-doped and undoped devices.

Figure 2.17 is the results of calculated intrinsic time response. The electron response of the undoped device is slower than the δ-doped, but holes are relatively faster. The total time responses for the two structures under survey present obvious difference attributed to the different contributions from electrons and holes. Total time response of the δ-doped structure has a faster initial response due to the electrons but long tail due to the holes, the undoped device shows a feature of slower initial response with faster decay. The FWHMs of intrinsic response are 8.2 ps and 2.4 ps respectively for the undoped and the δ-doped structures, which take the saturation velocity into account. We also notice that the peak value of the current in the δ-doped structure is smaller than the undoped one, which can be explained by the carrier collection efficiency. Because of the existence of a barrier at the interface of the active layer and the barrier enhancement layer, the carriers then fall into the 2-D gas. Transport in the 2-D gas will be addressed in the Chapter 5.

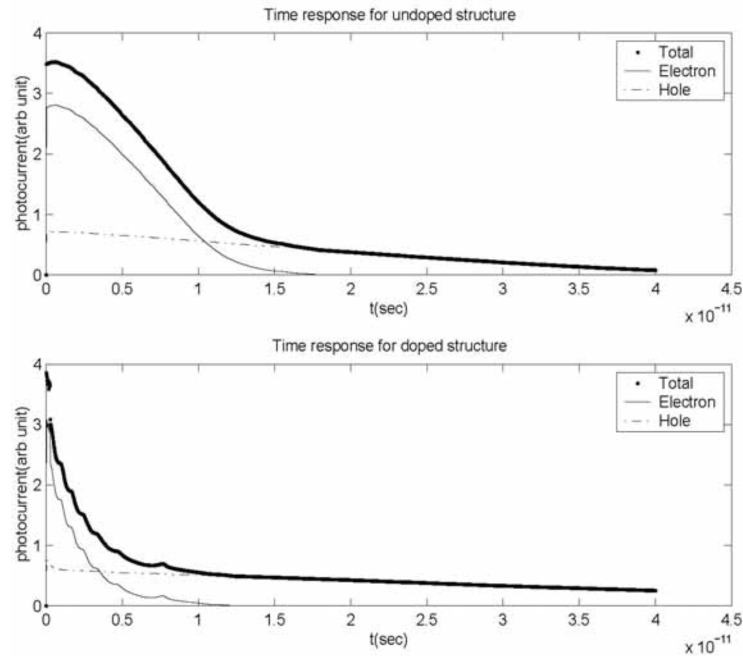

Figure 2.17 Time response comparison between doped (bottom) and undoped (top) device with separated contributes from electrons and holes.

The step-wise behavior shown in δ-doped time response is an artifact of simulation; it is the results of the number of electrons being limited, and the fact that they are collected quickly with respect to time constants of the simulation. Using larger numbers will smooth this response.

Figure 2.18 compares the time response of photocurrent contributed by electrons from different device geometries, i.e. 2 and 4-μm, respectively. We observe, as expected, the 4-μm device exhibit similar time response as 2-μm device as far as the electron contributions is concerned. This result is consistent with what we previously observed experimental data in Table 2.1, where the finger gap of 2 and 4-μm devices exhibit similar FWHM. It verifies our proposal that the vertical field transform the device behavior which allows the same dynamics occurs for different finger separations when only the electron is considered. However, before we can realize such a device, the slow holes issue has to be solved.

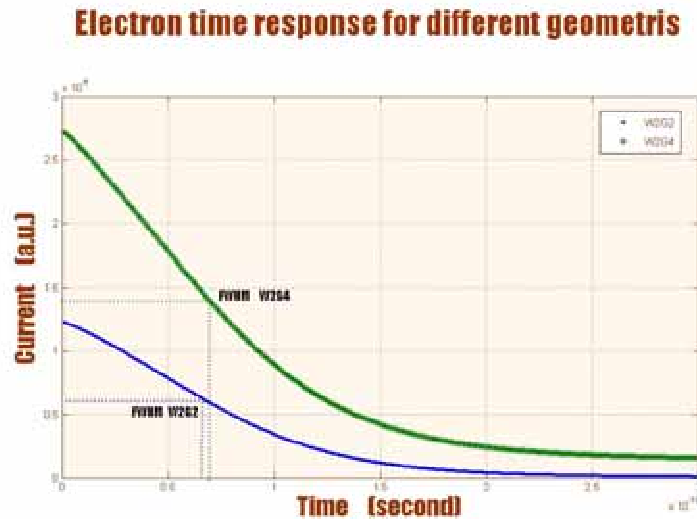

Figure 2.18 Comparisons of time responses due to electrons for figure gap of 2 and 4-μm devices.

2.4 Conclusion

Static device simulation based on Schrödinger and Poisson's equation was combined with dynamic response formulation to study the effect of an internal field in the behavior of a heterojunction MSM. We observe that the introduction of δ-doping significantly changes the two dimensional field profiles from a laterally oriented field to a vertical one, which affects the trajectory of photogenerated carriers. This greatly modifies the transit time, which is the decisive factor for dynamic response, namely the speed performance of photodetector. By analyzing the dynamic behavior of the two structures, the time response for a δ-doped structure was found to have fast initial response due to the structure advantage on electron transport, but a long tail due to the degraded hole transport compared with the undoped structure. This means that by collecting the holes at the bottom of the device or by introducing centers for quick recombination of holes, low frequency components of device behavior may be eliminated. We also show that an MSM with a vertical field is insensitive to device lateral geometry as far as the dynamic behavior is concerned, which is consistent with our

measurement results. A great improvement in high speed performance can be expected without scaling if the bottleneck of hole collection can be overcome.

This simulation is valid until carriers reach the 2-D gas. A more complete picture will evolve when transport within 2-D is considered in the Chapter 5. Nevertheless, we can argue that the electron that reach 2-D will contribute to the current since DC current measurements show similar, if not better, responsivity between doped and undoped devices.

CHAPTER 3: 2DHG DEVICE DESIGN AND PERFORMANCE

The previous chapter reports on fabrication and simulation of the simulated two-dimensional-electron-gas (2DEG) based photodetector. As reported in Table 2.2, the time responses of two devices with different finger separations showed similar FWHM. Simulation results suggest that 2D electron gas created a vertical field which facilitated the electron collection. This observation brings our attention on two issues. One is the vertical field originated from the 2-DEG transforms the transit path in the absorption region from a lateral developed to a vertical one, which greatly facilitate the dynamic transport of long device, namely large finger separation device; the other is the same vertical field, in turn, hampered slow carrier transport, since they move all the way opposite to the bottom of the device and the transit path is even longer than in lateral field device.

Two major problems remaining are, (1) can we take advantage of the same field to collect the slow carriers? Therefore, the long tail in the time response plot can be enhanced for larger bandwidth performance, and (2) what is the role that 2-D gas play in collecting the majority carriers. As we mentioned before, the vertical field pulls the majority carrier to the 2-D gas, and how the 2-D gas collecting the carriers remains unrevealed. This chapter, along with the Chapter 5, will discuss the two issues separately.

To investigate the slow carrier dynamics, we designed and fabricated 2-DHG based heterostructure MSM photodetectors for 850-nm wavelength detection. The fabrication was done by Fabio Quanranta and Eric Gallo in Italy. In this chapter, the device design and performance will be addressed in detail. The results of current-voltage characteristics, current spectrum, optical reflectivity, time response will be presented and discussed.

3.1 Two-Dimensional-Hole-Gas (2-DHG) Device Design and Fabrication

The detailed design will be fully addressed in Chapter 6, where, the design guidelines, criteria and considerations will be investigated systematically. In this chapter, our major effort focuses on presenting the design for optimization and simulation results.

3.1.1 Device Design and Optimization

The objective of the 2-DHG MSM-PD device design is to create a layer of two-dimensional-hole-gas along the heterojunction where the active absorption region and barrier enhancement layers meets. It is also necessary to develop enough vertical field directed toward 2-DHG to reduce the hole transit path in the device. The design of the device comprises the designs for modulation doped heterostructure, DBR quarter-wave stacks, optical cavity for the absorption region, and the barrier enhancement layer. For the purpose of comparison, we would like to keep the features of previous 2-DEG device to the extent possible.

Heterostructure design: In order to create high sheet density of the 2-DHG, two schemes have been proposed. One is based on strained $In_xGa_{1-x}As$ material, where the in-plane effective mass of the hole in this material is less than in usual GaAs due to the strain [74], and the valence band offset of the AlGaAs/InGaAs/GaAs is larger than the usual AlGaAs/GaAs due to the small bandgap of the InAs material. The other scheme is based on $Al_xGa_{1-x}As$/GaAs heterostructure, where the valence band offset helps confine the 2-DHG. The advantage of this scheme lies in the fact that the epilayer structure is simpler since there is no need to introduce extra materials and layers, and the growth and fabrication technology for this structure is mature.

By choosing appropriate component of In-, InGaAs material grown on GaAs is subject to biaxial compression strain, lifting the degeneracy of the light and heavy hole valence bands, thus giving rise to lighter effective mess of holes [75], provided the layer thickness is kept small and the resulting

strain not relieved by high density of dislocations [76]. The alteration of the energy band structure due to the strain creates a lower in-plane hole effective mass. Such lighter holes have been observed directly [77].

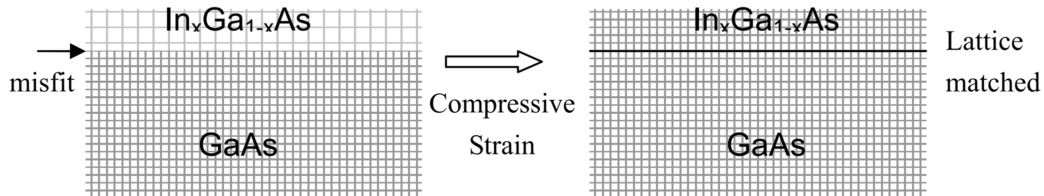

Figure 3.1 Illustration of InGaAs compressive strain on GaAs substrate.

Figure 3.1 illustrates the epitaxial layer arrangement for lattice-matched and the compressive coherent strain cases with in-plane compression of the lattice constant in the epitaxial layer and out-of-plane expansion.

Given the information above, we simulate several $Al_xGa_{1-x}As/In_xGa_{1-x}As/GaAs$ heterostructures with different Al- component, i.e. *x=0.3, 0.47*, and In- component, i.e. *x = 0.2, 0.35*, with ISE software. The simulation conditions remained the same as previous 2DEG device. The energy band structures of the one of the samples, from the ISE simulation, are shown in the Figure 3.2. Figure 3.2 is the energy band diagram of the device cut in the middle of the device, where *x=0*, along the layer growth direction *y*. Here y=0 is the heterointerface of $In_xGa_{1-x}As$ /GaAs. We notice that the quantum wells are well established, which is the prerequisite for a well defined 2-D gas. However, the flat conduction and valence band in the absorption region suggest that there is no vertical field developed in *y* direction toward the 2-DHG, since the field is obtained by the slope of the potential. In other words, the photogenerated carriers cannot be swept out of the absorption region by vertical field and the

transit path remains the distance of finger separation, though the quantum well is able to confine the 2-DHG and create high hole concentration and low hole in-plane effective-mass, which might allow the 2DHG to collect the photogenerated carriers effectively.

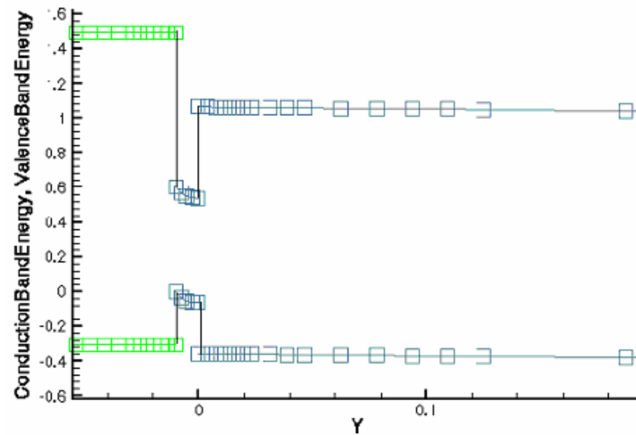

Figure 3.2 Energy band diagram for $Al_{0.3}Ga_{0.7}As/In_{0.35}Ga_{0.65}As/GaAs$ heterojunction.

Therefore, the scheme of employing $In_xGa_{1-x}As$ layer has to be replaced with the second scheme, which attempts to create the 2-DHG directly from $Al_xGa_{1-x}As$ /GaAs, and reach a maximum hole concentration in the 2-DHG layer without parallel conduction in the doping layer. The major considerations for modulation doped heterostructure design are the doping level and thickness of the spacer layer to achieve optimized tradeoff between carrier concentration and mobility.

A typical Al- component of $x = 0.5$ for 2-DHG [78] [79] is used to create large valence band offset, and experimental results demonstrated a ΔEv of 0.21-eV [80]. Several simulations refined with ΔEv of 0.21-eV by adjusting the electron affinity were performed to optimize the design.

Doping Profile: Here we compared the atomic-plane doping (APD) [81, 82] profile with uniform doping profile in terms of the effectiveness of the modulation doping. The typical geometry of W2G2

structure is used. Figure 3.3 plots the hole densities for both uniformly doped and δ-doped device. The plot cut the device in the middle, where *x=0*, along direction *y,* where the *y=0* is the heterointerface of $Al_xGa_{1-x}As$ /GaAs. The sheet doping levels are $1x10^{12}$, $2x10^{12}$, $4x10^{12}$ and $6x10^{12}$ /cm^2 respectively for both doping profiles. Figure 3.3(a) is hole densities under the uniform doping, Figure 3.3(b) under APD. We observe an obvious higher 2D concentration in the APD profile.

The two peaks in the δ-doped diagram are where the δ-doping layer and the 2DHG are located, respectively. For the same doping level, we observed higher 2-DHG hole peak density in the δ-doped device than in uniformly doped, hence, δ-doping is a more suitable choice. More discussions about advantage of the APD will be addressed in the Chapter 6.

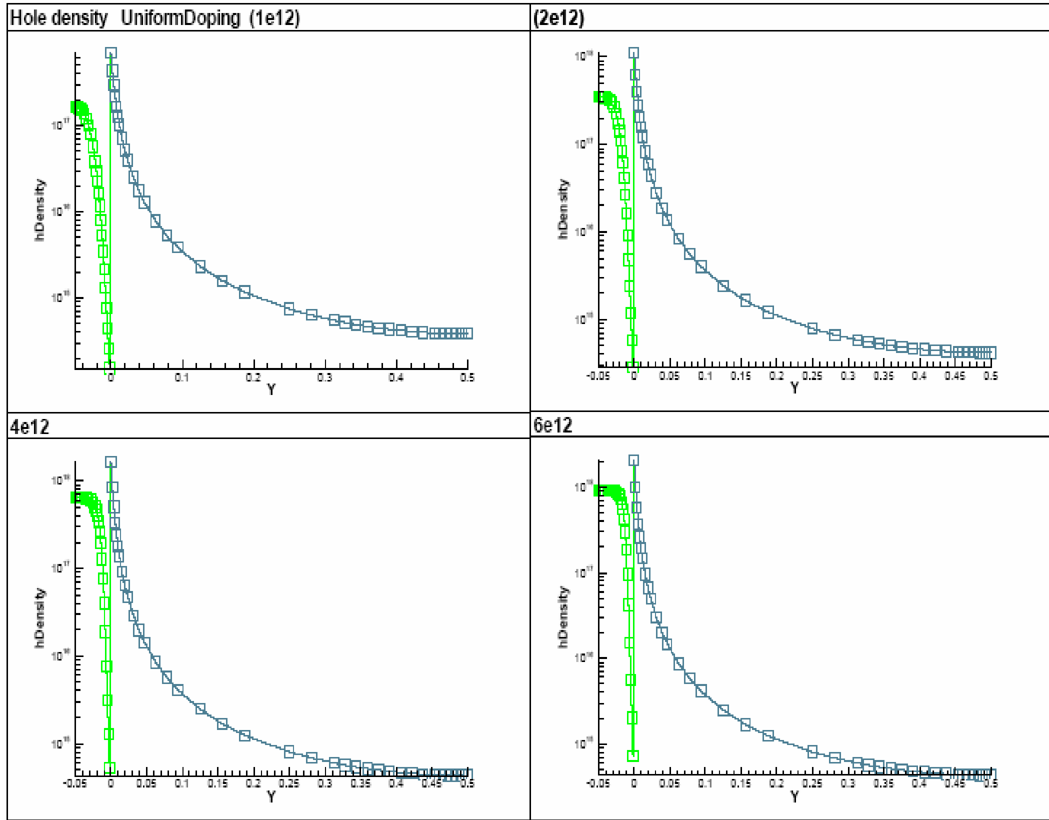

(a)

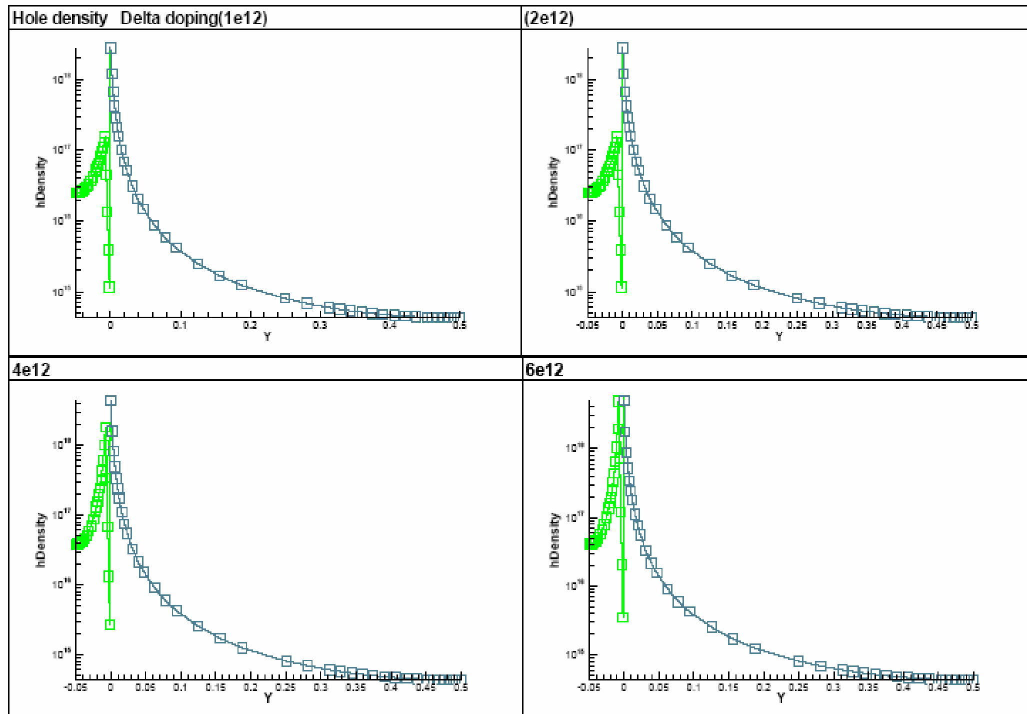

(b)

Figure 3.3 Doping concentrations of the 2-DHG for different delta doping level with (a) Uniform doping (b) Delta doping.

Doping level: To determine the appropriate doping level, we simulated several different doping levels ranging from $1x10^{12}$ to $5x10^{12}$ $/cm^2$. This is performed in order to monitor the number of electrons that remain in the doping plane. As we observed from previous plot that at doping level of $6x10^{12}$ $/cm^2$, the δ-doping layer has the same hole density as the 2-DHG. It means, given the same Fermi level, the potential at the top of the valence band of the 2-DHG is the same as that of the δ-doping layer. This may result in unwanted parallel conduction in the device, which may greatly increase the dark current and decrease the delectability. Figure 3.4 plots the ratio of peak hole density and peak δ-doping concentration at different doping levels. The ratio of hole density in the well and doping density is given. The best doping level thereby is found from the plot to be around $2x10^{12}/cm^2$, where the highest ratio of 2-DHG versus the δ-doping layer is reached.

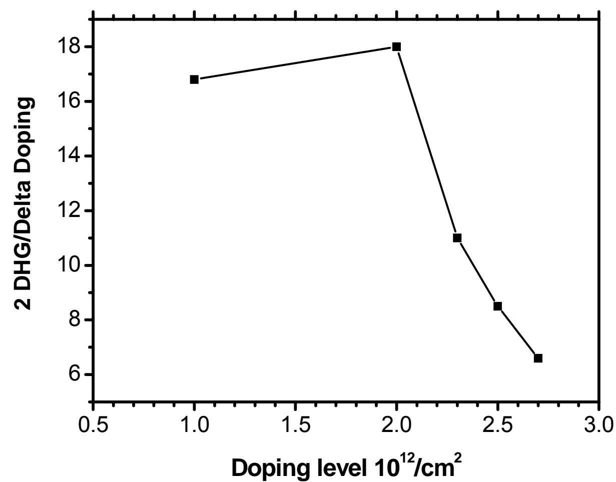

Figure 3.4 The ratio of 2DHG and δ-doping concentration at different doping levels.

Spacer: Thickness of the spacer layer is an important parameter in terms of the trade-off between the carrier concentration and carrier mobility in the 2-DHG. At the δ-doping level of $2x10^{12}/cm^2$, we simulated several thickness of the spacer layer in order to study the influence of the spacer layer on the

carrier concentration. As a matter of fact, the high mobility in the 2D gas is due to the lack of carrier-impurity scattering events since the doping atoms are spatially separated from 2-D gas. Therefore large spacer layer decreases the effectiveness of carrier transfer but is able to enhance the mobility in principle. A balance needs to be found, where, the spacer layer gives high carrier density without lost of mobility advantage. Figure 3.5 (a) presents several hole density distributions along the growth direction. Figure 3.5(b) plot the peak hole density with respect to the spacer layer. The ratio between the 2-DHG and delta-doping layer is plotted as well. Figure 3.5 indicates, at 7-nm, the ratio reaches a maximum, which is the balance point we are looking for.

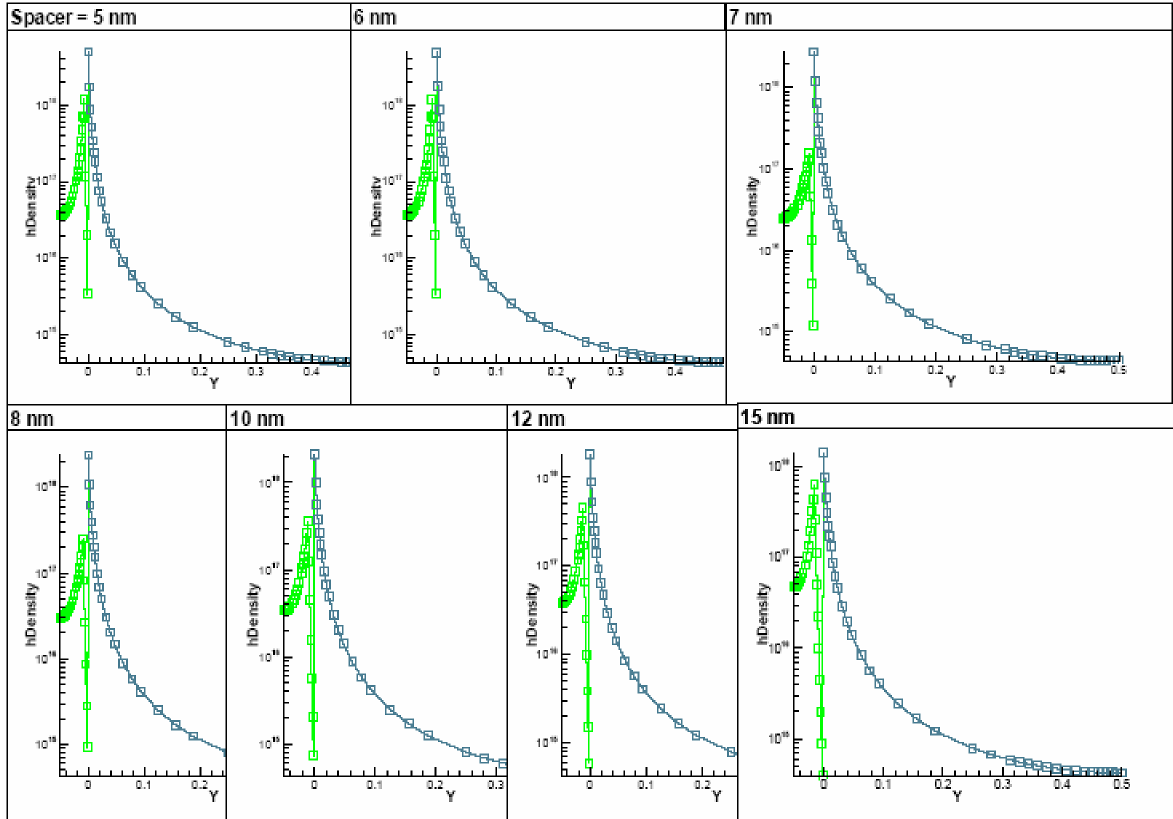

(a)

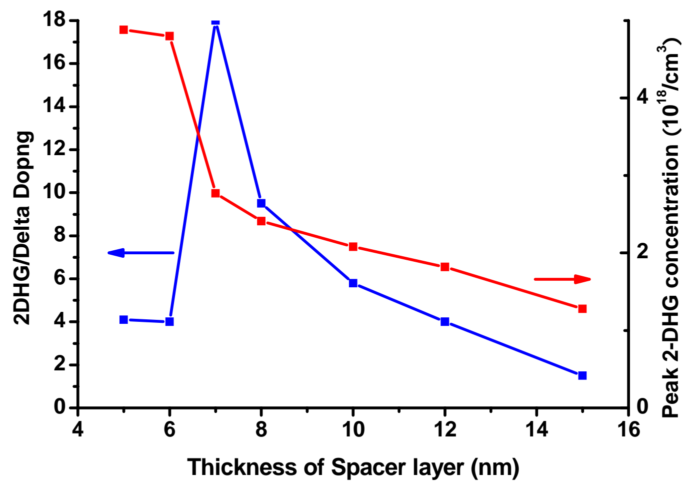

(b)

Figure 3.5 (a) Hole concentration distribution in the 2DHG at different thickness of spacer (b) Peak 2DHG concentration and ratio of 2DHG/δ-doping at different thickness of spacer.

Vertical field: Previously, we investigate several simulation results for optimized modulation

doping structure, which attempts to establish an excellent quantum well to host 2-DHG. Another property of interest is the vertical field.

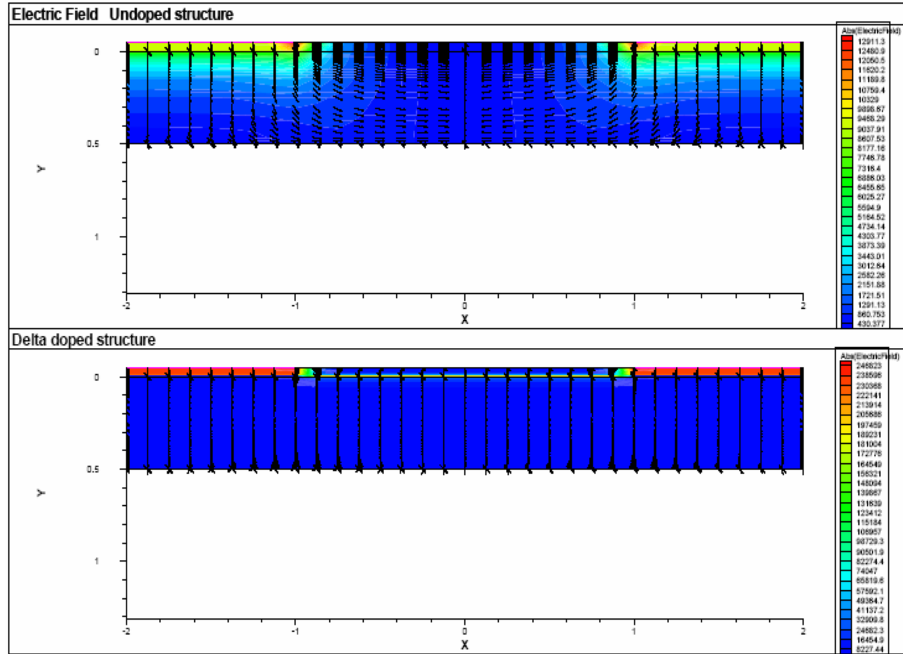

Figure 3.6 Two dimensional field vector distributions in the doped (bottom) and undoped (top) device at equilibrium.

Figure 3.6 compares field vectors for doped and undoped structure. Both figures present the cross section of the device. We observe an obvious vertical field developed in doped device and lateral field in undoped.

Based on these simulation results, the layered structure for a 2-DHG device is determined as follows:

Table 3.1 The Layered structure for 2-DHG device.

Layer #	Thickness	Material	Specification
7	500 Å	$Al_{0.5}Ga_{0.5}As$	Barrier enhancement layer
6	Be Delta doped		1~2.5*10^{12}/cm2
5	70 Å	$Al_{0.5}Ga_{0.5}As$	Undoped
4	117.5 nm	GaAs	Absorption layer
3	59.6 nm (x15)	$Al_{0.24}Ga_{0.76}As$	15 wells for Bragg Reflection
2	67.6 nm (x15)	$Al_{0.9}Ga_{0.1}As$	15 wells for Bragg Reflection
1	200 nm	GaAs	Buffer
0	2"	GaAs	Semi-insulating Substrate

3.1.2 Device Fabrication

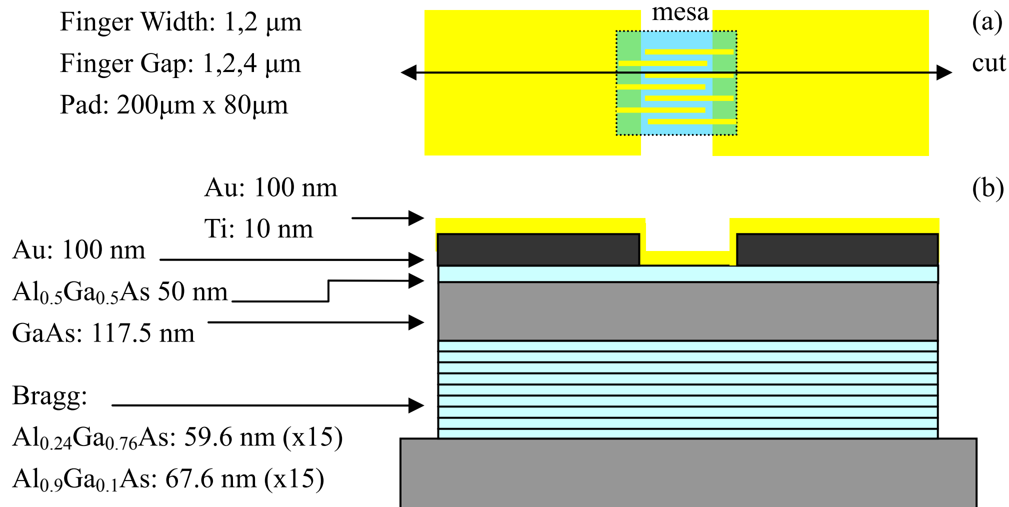

Figure 3.7 (a) Top view of the device with electrode (b) Cross section of the device on wafer.

The device consists of two Schottky contacts on the top of a δ-layer modulation doped AlGaAs/GaAs heterostructure. The wafer for the devices fabrication was grown by MBE on a (100)-oriented semi-insulating GaAs substrate. The schematic of the cross section and the top contact of the device are shown in Figure 3.7. The area of each contact is 200x80 μm^2, and the device active

area is 40x40 μm^2 with the number of fingers varying for different electrode geometries.

The wafer was grown by IQE, Inc. A 200-nm GaAs buffer layer was grown on the 2” GaAs semi-insulating substrate. The $Al_{0.9}Ga_{0.1}As/Al_{0.24}Ga_{0.76}As$ DBRs, with thickness of 67.6-nm and 59.6-nm, respectively, for the purpose of optical reflection, were grown on the GaAs buffer, followed by a GaAs absorption layer 117.5 nm thick, with the $Al_{0.5}Ga_{0.5}As$ barrier enhancement layer 50nm thick above it. Al- component of 0.5 was designed to increase the valence band offset up to 0.21eV [80] for better confinement of the hole gas. A Be atomic-planar-doping (APD) in the barrier enhancement layer is 7 nm away from the AlGaAs/GaAs heterointerface with nominal density of $2.5x10^{12}/cm^2$. This δ-modulation doped heterostructure creates 2D hole gas along the heterojunction. Finally, a 5-nm thick top layer of highly Be-doped GaAs was added to facilitate the formation of the Ohmic contacts when necessary.

The device was fabricated by Consiglio Nazionale delle Ricerche (CNR)/ Istituto per la Microelectronica ed Microsistemi (IMM) in Italy. Fabrication followed standard procedures, including optical lithography, metal evaporation and lift-off. 200-nm SiN was deposit for planarization. The interdigitated electrodes were deposited with a Ti/Pt/Au multilayer, forming Schottky contacts to the semiconductor.

The detailed growth layer structure is shown and the thickness of epilayers is verified by SEM cross-sectional images below. Figure 3.8 shows the layered structure with measured thickness from high doped wafers.

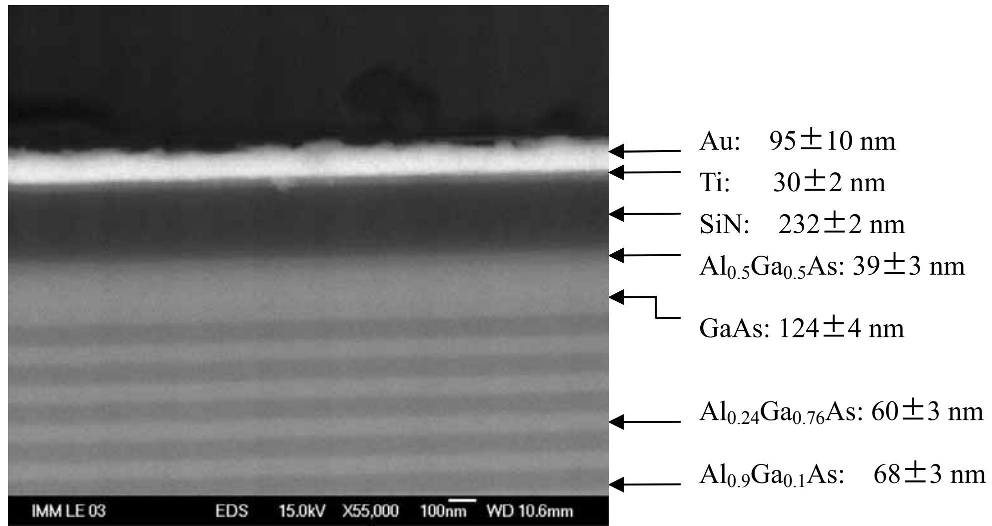

Figure 3.8 SEM pictures of the epilayer structure, courtesy of CNR-IMM.

Several SEM images of mesa isolated fabricated device are shown below. Figure 3.9 illustrates interdigitated contacts. The top-left is the side view, top-right is the close-up top view, bottom-left is the close-up side view, and the bottom-right is the top view of the fingers with contacts on the mesa.

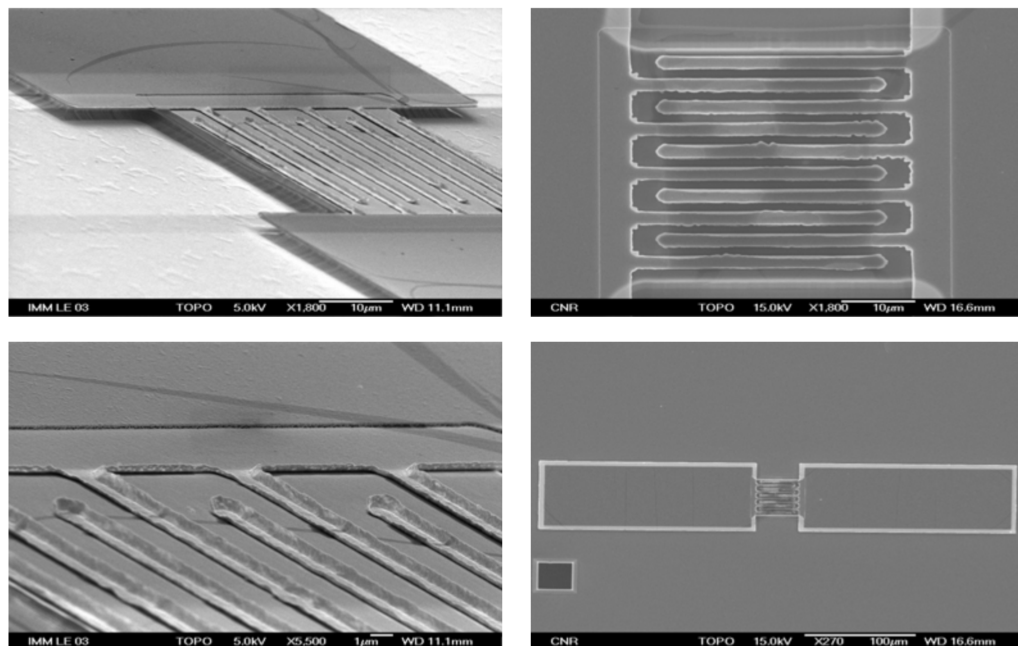

Figure 3.9 SEM pictures of the interdigitated fingers, courtesy of CNR-IMM.

3.2 Dark and photocurrent performance

The current-voltage characteristics relates to several aspects of performance in the photodetector. The dark current is the leakage current generated by the bias voltage applied to the device without being subjected to illumination. Large dark current generate shot noises and affects important figures of merit, such as, signal-to-noise-ratio (SNR), noise equivalent power (NEP) and sensitivity.

The low dark current allows MSM-PD maintain a sufficiently low minimum detectable power level for low noise and high sensitivity applications. The MSM-PD electrodes are made with two blocking Schottky contact on the undoped semiconductor layer. The Schottky barrier height plays an important role to modulate the dark current. The unique dark current in the device is due to Schottky contact acting with the layered two-dimensional structure, mostly the 2-D gas. The I-V characteristics exemplify more complicated behaviors. Figure 3.10 shows the simulated 2-DHG device under equilibrium for δ-doping level of $2x10^{12}/cm^2$.

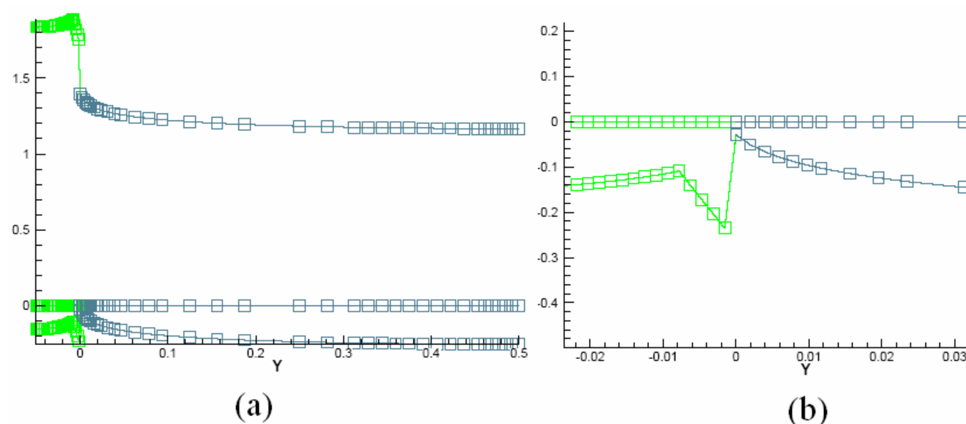

Figure 3.10 (a) Simulated energy band diagrams under equilibrium (b) A close-up look at the heterointerface.

Figure 3.11 draws the paths of current flow in the 2-D(top) based on above simulation results.

The schematic diagram of energy band is drawn when it is expanded from 2-D into 1-D with the current flow, under equilibrium (middle) and applied bias (bottom).

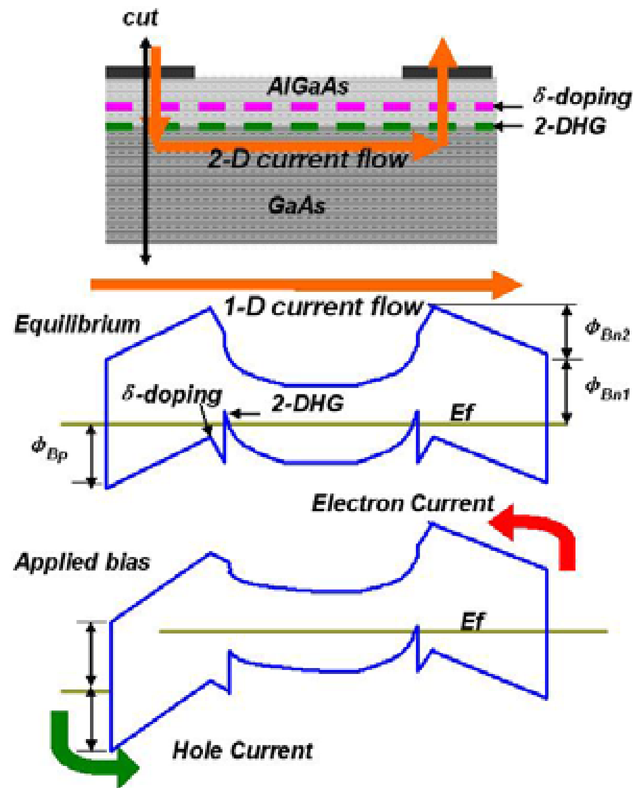

Figure 3.11 Extension of the 2D path of current flow to the 1D.

For MSM structure, most of the voltage applied drops across the reverse biased junction. As we see from the middle and bottom picture in Figure 3.11, the electron current that flows through the forward biased junction remains unchanged since the barrier for electrons does not vary with the applied bias under forward biased junction. The I-V relationship reflects the hole current mostly. The barrier for holes is Φ_{Bp} as shown in Figure 3.11. Before the 2-DHG under anode is depleted, the hole current overcomes the barrier Φ_{Bp} falling into the 2-DHG and conducting through the channel, as indicated by path A in Figure 3.11. As the 2-DHG under anode has been completed depleted, the

hole current transport vertically through the 2-DHG and then transport in the GaAs layer laterally as indicated by path B in Figure 3.11.

As we previously introduced, the dark current of the MSM structure is mainly controlled by the reverse biased Schottky junction. The I-V behavior of a Schottky diode can be characterized with two parameters: the ideality factor, barrier height. Beyond that, the shape of the electrostatic potential of the Schottky barriers is also important since the overall current through a barrier is a sum of two contributions, (i) thermal emission current and (ii) the tunneling current. Whereas the first is determined by the height of the barrier, the second by the overall shape of the barrier profile, and can be neglected in most of the cases.

According to the thermionic emission theory, the MSM-PD dark current for the metal with barrier height φ_{Bp} decreases exponentially with the increase of φ_{Bp}. Usually, the effective barrier height is introduced, which has to be overcome by the carriers to enter the transport process, therefore the I-V relation can be expressed as [16]:

$$I = AA^{*}T^{2}\exp\left(-\frac{\Phi_{beff}(V)}{k_{B}T}\right)\left\{\exp\left(\frac{qV}{k_{B}T}\right)-1\right\} \qquad (3.1)$$

where, k_B is the Boltzmann constant, T is the temperature, A is the electrode area, A^* is the effective Richardson constant, which is assumed remaining intact by tunneling effects, and V represents the applied bias. It is been well established that the effective barrier height is affected by the image force effect function, which is dependent on the electrical field close to the Schottky contact. Therefore it is also a function of the applied bias voltage. Different from depleting a piece of uniformly doped semiconductor, the applied bias, in our case, has to deplete the 2-DHG vertically firstly, and then deplete the GaAs laterally; it is a two-stage process.

In contrast to Si, the Schottky barrier height on GaAs is nearly unaffected by using different

Schottky metalizations. The strategies to lower the dark current are developed toward varying the potential profile and enhance the barrier height. Barrier enhancement layer is employed to increase the height of Schottky barrier[83]. Previous work in our group also demonstrated that the electron cloud in parallel with electrode contact was able to enhance the barrier height of the Schottky as well [84].

3.2.1 Dark Current Characterizations

Our previous 2-DEG photodetector demonstrate a dark current of 10-pA for the geometry of W2G2 device at bias voltage of 10-V. However, our 2-DHG MSM exhibit an extremely low dark current of less than 2-pA for low-doped device and 10-pA for high-doped device, as shown in the Figure 3.12, for the same geometry and same voltage.

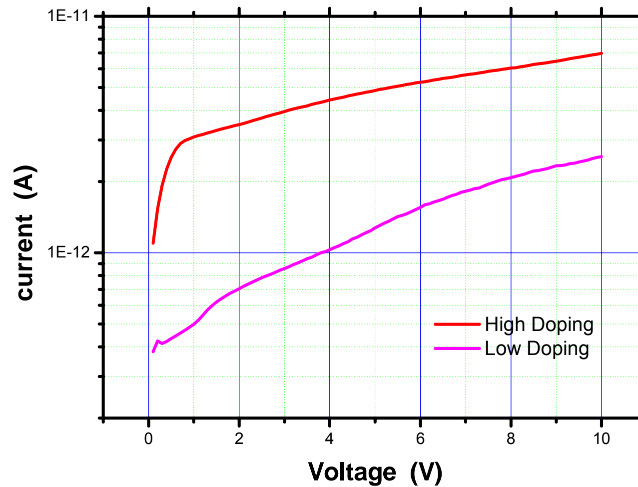

Figure 3.12 Dark current for W2G4 device on low doped and high doped wafers.

In Figure 3.12, the I-V characterization from the high doping devices shows two stages, which is predicted by the previous energy band diagram analysis. The first stage I-V is due to the depletion of 2-DHG underneath of anode, and the second due to the lateral depletion in the GaAs thereafter. As we

can tell from the I-V curve, the slope of current changes at V=0.7V, where the 2-DHG under the reverse biased junction has been completely depleted. This can be further verified by the C-V characteristics which we will address in the next chapter. For low doped device, the 2-DHG has been depleted at equilibrium due to the small carrier density, hence we do not see the stage due to vertical depletion of the 2-DHG.

The extremely low dark current is attributed to the heterodimensional contact of 3-D metal with the 2-D gas [84, 85], where, I-V characteristics is formulated by the method of quantum-mechanical transmission,

$$J_{g\to m} = q\frac{2}{h^2}\int T(E_x)f_g(E)[1-f_m(E)\frac{\partial E}{\partial p_x}dp_x dp_y] \tag{3.2}$$

where, $J_{g\to m}$ is the current created by carrier transporting from 2-D gas to the 3-D metal, $T(E_x)$ is the transmission coefficient representing the probability that an electron with energy E_x is able to overcome the barrier, $f_g(E)$ is the Fermi distribution function, h is the Plank's constant, E is the electron energy, p_y is the electron moment component normal to the direction of the current flow, and E_x is the carrier kinetic energy in the x-direction. The $T(E_x)$ can be determined by WKB approximation [86] is expressed as:

$$T(E_x) = \exp[-\frac{2}{h}\sqrt{2m}\int(\sqrt{qV(x)+E})dx] \tag{3.3}$$

where, $V(x)$ is the potential profile of the Schottky-2D gas junction along x-direction.

Eventually, the general expression of the net current is derived, by taking two components flowing in opposite directions into consideration:

$$J = J_{g\to m} - J_{m\to g} = \frac{q\sqrt{2m^*}}{h^2}\int_{E_0}^{\infty}[f_g(E)-f_m(E)]\times\{\int_0^{E-E_0} T(E-E_0-E_\perp)(E_\perp)^{-\frac{1}{2}}dE_\perp\}dE \tag{3.4}$$

where, $E_\perp$ represents the component of the energy associated with the direction parallel to the barrier, E_0 represents the first quantized energy band in the 2-D gas system. Interestingly, this universal expression reduces to conventional thermionic emission expression when the Fermi distribution is replaced by the Boltzmann distribution and the incident carrier carry energy greater than the barrier height.

The ratio of current in 3D-3D contacting system to 3D-2D system can therefore be obtained:

$$r = \frac{I_{3-D}}{I_{2-D}} = \frac{L}{h}\sqrt{2\pi m^* kT}\,\exp(\frac{E_0}{kT}) \tag{3.5}$$

where L is the contact length, and E_0 is the first subband energy level in 2-D system.

The formulism suggests the major difference of 3-D metal contact to 2-D gas from the 3-D structure lies in the subband splitting in the 2-D gas, which elevates the effective barrier height, thus allow less carrier to enter into the transport process. And the formulism also predicts dark current of orders of magnitude less in 3D-2D system than in 3D-3D.

3.2.2 Photocurrent

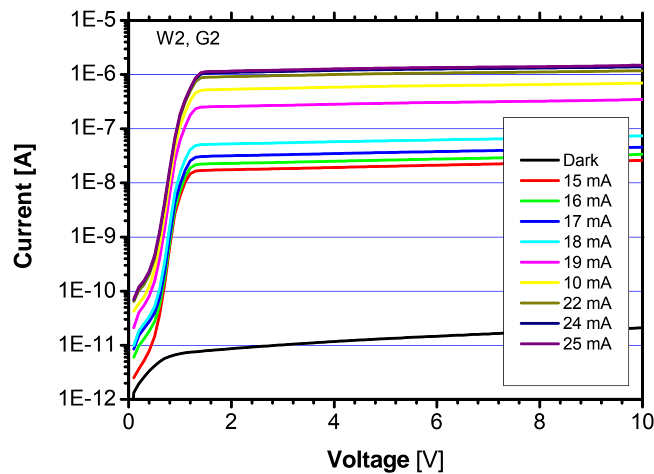

Figure 3.13 Photocurrent at different input optical powers for W2G2 device.

Figure 3.13 plots the photocurrent for W2G2 device based on the measurements performed at CNR IMM. We observe a 4 or 5 orders of magnitude of increase when the device is under illumination. The photocurrent reaches saturation as the external voltage greater than 1.5-V, and before that it exhibits strong exponential behavior, which confirms the well formed Schottky contact on the device.

3.2.3 Responsivity

Figure 3.14 plots the photocurrent with respect to the incident optical power. The measurement was adjusted at wavelength where the maximum photocurrent occurs, namely 795-nm. The corresponding responsivity is thus obtained to be 7×10^{-3}A/W. We observe the super-linear behavior of the responsivity even at large optical power up to 500-μW. The low responsivity can be explained by the incomplete depletion in the absorption region due to the spreading of the 2-DHG. On the other hand, it expands the linear regime of the responsivity, allowing the device accommodating higher input power.

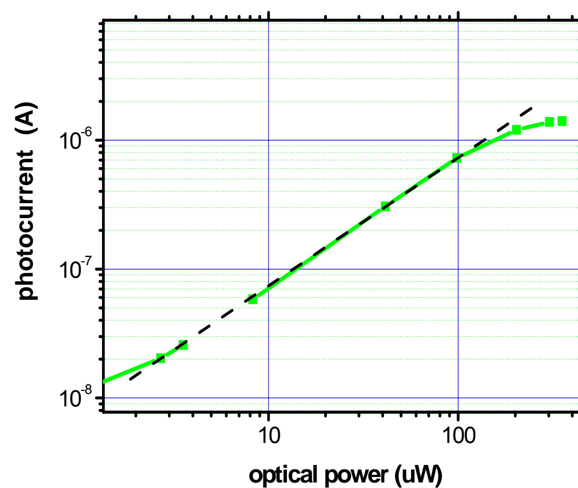

Figure 3.14 Photocurrent subject to different incident optical power for high doped W2G2 device at V= 5V. The linear fit of the curve is also shown.

3.2.4 Current spectrum

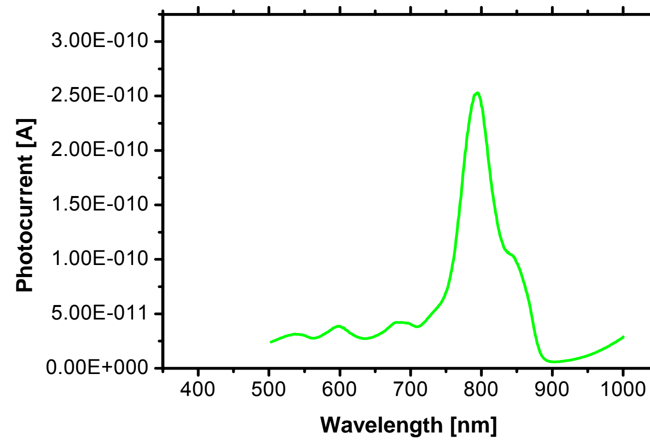

Figure 3.15 The photocurrent spectrum for low doped W2G2 device.

Figure 3.15 plots the current spectrum with wavelength ranges from 400 to 1000-nm. The current spectrum shows a prominent peak at 795-nm, where the reflectivity of the wafer reaches minimum. Contrary to previous 2-DEG device, the 2-DHG current spectrum misses the peak at absorption edge of the barrier enhancement material. This can be explained in a manner that the wavelengths of interest do not fall into the resonant wavelengths selected by the cavity. In another word, the standing wave of large amplitude in the cavity can be absorbed by neither material in the absorption region nor the material in barrier enhancement layer.

3.3 Optical Structure Characterization

3.3.1 Introduction

Our device is intentionally designed to obtain the maximum coupling of optical field with resonant-cavity-enhanced (RCE) and distributed-brag-reflector (DBR) structure. The asymmetric

Fabry-Perot (FP) cavity, depicted as in Figure 3.16, has low reflectivity front mirror, basically air, and high back reflector, namely DBR.

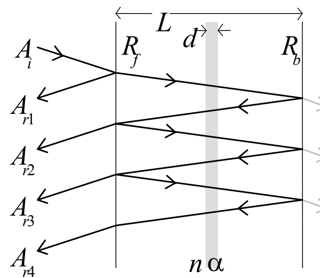

Figure 3.16 Schematic diagram of Fabry-Perot Cavity.

By appropriate design of the thickness of the quarterwave layers, the peak reflectance region can be tuned to the desired wavelength.

3.3.2 Reflectance Simulation

The Reflection spectra is calculated with transfer matrix method (TM) [87]. The treatment shows how to obtain the reflectance and transmittance of arbitrary, finite multilayers and was employed to compute the reflectance of dielectric stacks. The basic formalism yields the amplitude of the electromagnetic field of monochromatic waves reflected by and transmitted through the multilayer structure. The solution is achieved through propagation of the fields in the homogeneous layers, and the continuity of the tangential components of the electric and magnetic fields at the interfaces. Propagation for non-normal incidence can be incorporated. Figure 3.17 plot the schematic diagram of transmitted and reflected waves at the interface.

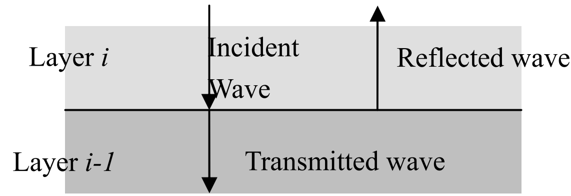

Figure 3.17 Wave transmission and reflection in a single layer.

For a single layer, single interface, the electrical and magnetic components of the wave in the upper interface of the material relates to components in the lower interface by the transformation matrix *Mi*:

$$\begin{bmatrix} E_{i-1} \\ H_{i-1} \end{bmatrix} = M_i \begin{bmatrix} E_i \\ H_i \end{bmatrix} \tag{3.6}$$

where, *i* is the subscripts refer to the number of layer, and M_i is calculated as

$$M_i = \begin{bmatrix} m_{11} & m_{12} \\ m_{21} & m_{22} \end{bmatrix} = \begin{bmatrix} \cos(d_i) & -jZ_i \sin(d_i) \\ -j\dfrac{\sin(d_i)}{Z_i} & \cos(d_i) \end{bmatrix} \tag{3.7}$$

where, $d_i = \dfrac{\lambda}{4n_i}$ is the quarterwave thickness, n_i is the refractive index. The reflection coefficient and transmission coefficient are then readily given by:

$$r = \frac{(m_{11} + m_{12}Z_0^{-1})Z_0^{-1} - (m_{21} + m_{22}Z_0^{-1})}{(m_{11} + m_{12}Z_0^{-1})Z_0^{-1} + (m_{21} + m_{22}Z_0^{-1})} \tag{3.8}$$

$$t = \frac{Z_0^{-1}}{(m_{11} + m_{12}Z_0^{-1})Z_0^{-1} + (m_{21} + m_{22}Z_0^{-1})} \tag{3.9}$$

where, $Z_0 = \sqrt{\mu_0/\varepsilon_0} = 377\Omega$ is the intrinsic impedance of the free space. Hence the reflectance, R and the transmittance, Γ, are defined as,

$$R = |r|^2 \tag{3.10}$$

$$\Gamma = |t|^2 \tag{3.11}$$

Expanding the result to a periodic dielectric multilayer, depicted in Figure 3.18,

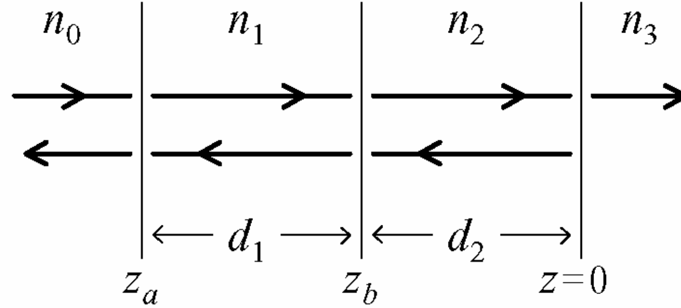

Figure 3.18 Transmitted and reflected waves in a multilayers structure.

the total reflectance can be calculated

$$\begin{pmatrix} B \\ C \end{pmatrix} = \prod_{i=1}^{q} M_i \begin{pmatrix} 1 \\ n_{subs} \end{pmatrix} \tag{3.12}$$

$$Y = \frac{C}{B} \tag{3.13}$$

$$R = \left(\frac{1-Y}{1+Y}\right)\overline{\left(\frac{1-Y}{1+Y}\right)} \tag{3.14}$$

where, Y is the optical admittance, and R is the reflectance.

We simulate reflectance properties of our layered structure using above methods including the wavelength dependent absorption coefficient in the absorption region, the wavelength dependent refractive index in the absorption region, the wavelength dependent refractive index in the barrier enhancement layer, and the wavelength dependent refractive index in the DBR layers. In the calculation, the refractive index in the $Al_xGa_{1-x}As$ material is a key parameter which affects the final results. The behavior of the $n(\lambda,x)$ is known to depend strongly on the values of critical points in the alloy compositions and band structures. Comprehensive refractive index data are available for GaAs [88, 89] and AlAs [90]. Data for $Al_xGa_{1-x}As$ exhibited discrepancies among different groups' measurements as reported in the literature [91] [92] [93]. The method of using the direct band gap rather than aluminum mole fraction as index of refractive index exhibits consistency of data among

experiments [94]. Another key parameter is the wavelength dependent absorption coefficient; Here, we use the widely cited data from Casey [95].

We fit those data using polynomial of degree of three, the wavelength dependent parameters were calculated for our structures as follows:

(1) Wavelength dependent absorption coefficient in absorption region:

$$\alpha = (63 \times E^3 - 309.8 \times E^2 + 563.1 \times E - 345.8) \times 10^5 \quad (3.15)$$

(2) Wavelength dependent refractive index

$$n_a = 0.27 \times E^2 - 0.3736 \times E + 3.43 \quad (3.16)$$

(3) Wavelength dependent refractive index for barrier enhancement layer

$$n_b = 0.1534 \times E^2 - 0.1288 \times E + 3.1327 \quad (3.17)$$

(4) Wavelength dependent refractive index for DBR

$$n_l = 0.16 \times E^2 - 0.22 \times E + 3.0238 \quad (3.18)$$

$$n_h = 0.21 \times E^2 - 0.2 \times E + 3.2326 \quad (3.19)$$

The lower case *l* represents the layer with lower refractive index and *h* represents the higher one.

Simulation results show that the reflectance spectrum is quite sensitive to the wavelength, especially the peak and side peaks of reflection. In most of the cases, the short wavelength regime, thus large photon energy regime, is affected more by the refractive index and absorption coefficient.

3.3.3 Reflectance Spectra Characterization

Figure 3.19 shows the measured reflectance spectrum compared with simulation results, which shows strong consistency between them except at long wavelength regime. We attribute the difference between the measured and the simulated to the absorption in the barrier enhancement layer and DBR layers. The major peak is at 840-nm. The measured spectrum shown below is obtained after moving

the top p+ cap layer. The asymmetric reflectance spectrum is due to the asymmetric reflectivity at the front and back mirror ends. The measured reflectance is quite similar for both high doped and low doped wafer; we attribute the minor difference to the carrier concentration related refractive index. This means that differences between doped and undoped structure are not due to optical properties; rather due to the electrical ones.

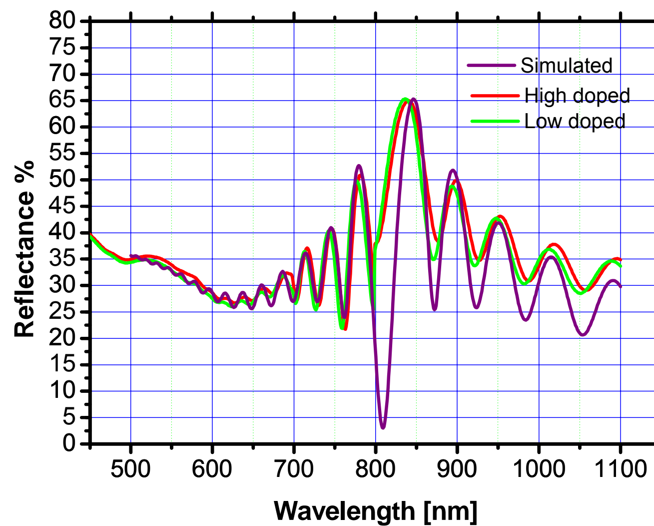

Figure 3.19 Experimental reflectance on high doped and low doped wafer compares with the simulated reflectance.

3.4 Time response

3.4.1 Introduction

We have previously fabricated and reported 2-DEG based photodetectors [35]. The time response for different finger distances, i.e., 2 μm and 4 μm, exhibit same FWHM, which suggest the fast electron transport is not limited by the finger separations. Simulation results reveal it is the vertical field that facilitates the electron transport, at the same time, it degrades the hole transport. As a result,

the vertical field created by 2-DEG can help the transport and collection of electrons. This observation motivates us to study the hole transport behavior in 2-DHG device.

3.4.2 Simulation Results

The electrical properties are simulated by commercially available software ISE-TCAD. All previous simulation conditions mentioned in chapter two have been persevered; the alterations we have made are (1) the depth of the device is 117-nm, which is the real device dimension, (2) ΔEv of 0.21-eV given Al- component of 0.5 in the wide bandgap material. As we discussed before, the Ramo's theorem is employed to simulate the dynamic behavior of photogenerated carriers in the active absorption region. The electrical properties from ISE-TCAD were fed in.

3.4.2.1 Electrical field

The electrical field vector has been shown in the previous section. Figure 3.20 gives the detailed x and y component of the electrical field vector in three dimensional view. Figure 3.20(a) is the Ex component, (b) is the Ey component. Y is the wafer growth direction.

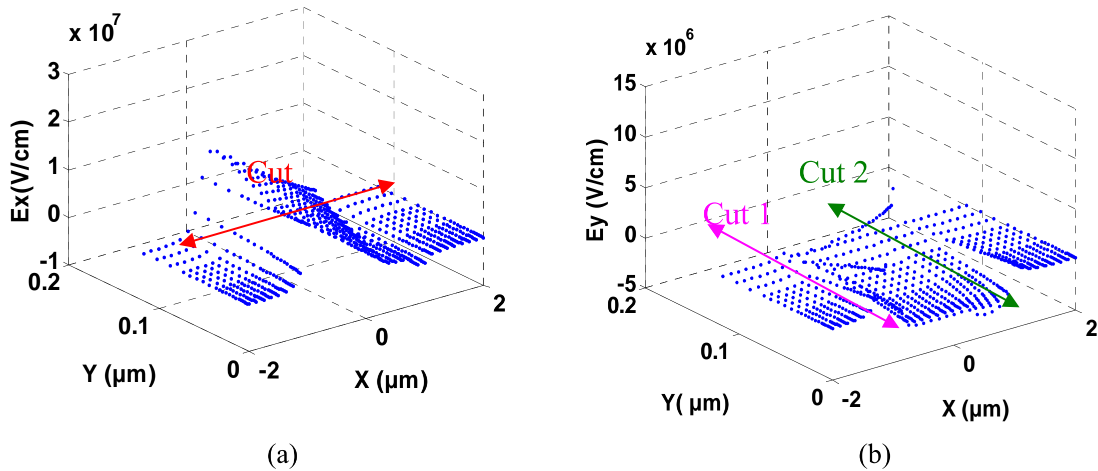

Figure 3.20 Three dimensional view of the electrical field in (a) *Ex* component (b) *Ey* component.

Figure 3.21 shows the ISE simulated two-dimensional electrical field cut in lateral and vertical direction respectively under different external voltages, as the cuts shown in Figure 3.20. The Figure 3.21(a) exhibit lateral field cut in the middle of the absorption region, as show in Figure 3.20(a), in parallel with the epilayer. Leftmost 1 μm is the anode, the right most 1 μm is the cathode. The voltages are 1, 5, 10, 15, 20-V respectively. In view of MSM structure, the cathode side is reverse biased Schottky junction and cathode is forward biased. The peak of the electrical field is right underneath the edge of the electrode. We observe that the lateral fields vary with the applied bias proportionally, and they extend to the cathode gradually in accordance with the applied bias. One more observation is, even under external voltage of 20-V, the depletion region of the reverse biased Schottky junction just extend to the “reach through” [24] regime; hence the current transport in the MSM structure is still controlled by the reverse biased junction below 20-V. Figure 3.21 (b) shows the vertical field cut right under the anode, the cut 1 as shown in Figure 3.20 (b), which is similar to the lateral depletion that the vertical field grows with external bias voltage.

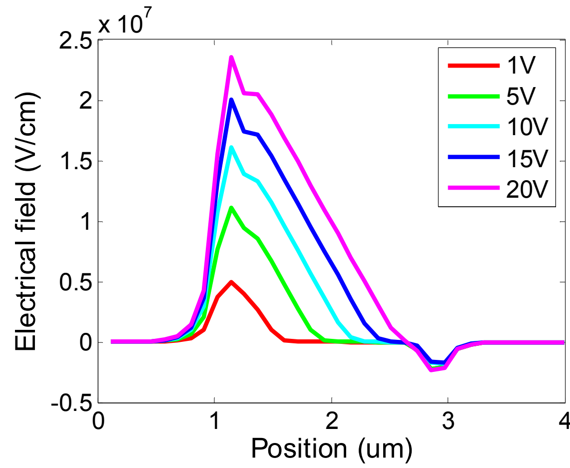

(a)

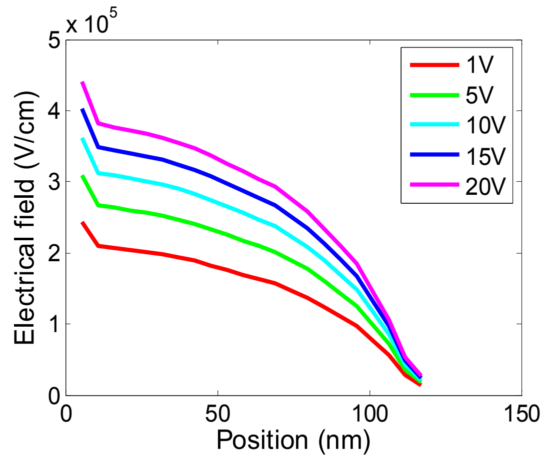

(b)

Figure 3.21 (a) Lateral field cut in the middle of the absorption region (b) Vertical field cut underneath the anode.

Figure 3.22 exhibits vertical field cut in the middle of the finger gap, the cut 2 as shown in Figure 3.20(b), along the growth direction in the active absorption region. Zero in the axis is where the heterointerface locates; 118-nm is the bottom of the absorption region. In contrast to the lateral field, vertical field experiences a sudden variation in terms of distribution with respect to the external bias. At low bias, i.e. less than 5V, the vertical field is strong at the region close to the junction, but decays gradually as it extends to bottom of the absorption region. At higher bias, i.e. above 10V, the vertical

field is more evenly distributed in most of the absorption region, and rapidly decays to a low value.

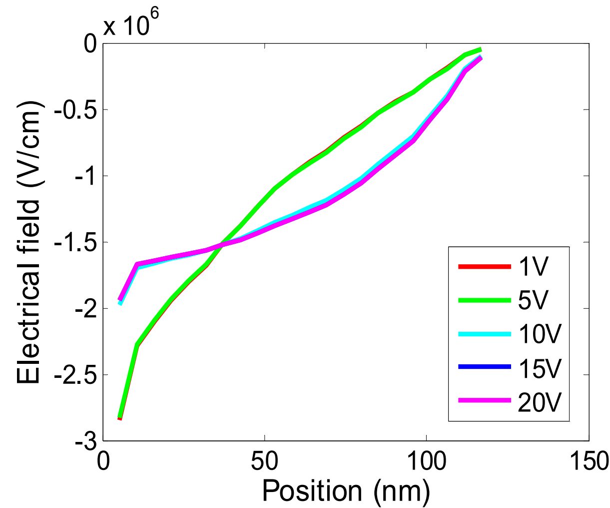

Figure 3.22 Vertical field cut in the middle of the absorption region.

We combine the voltage dependent lateral and vertical field together, the 2-D electrical fields have the tendency that are developed more laterally directed as going deeper into the bottom of the absorption region.

3.4.2.2 Contributions from both carriers

Under the electrical field shown above, the evolution of the electron and hole concentration and corresponding transient contributions to the photocurrent are shown in Figure 3.23 and Figure 3.24, respectively. The carrier intrinsic time response was calculated using two-dimensional Ramo's theorem.

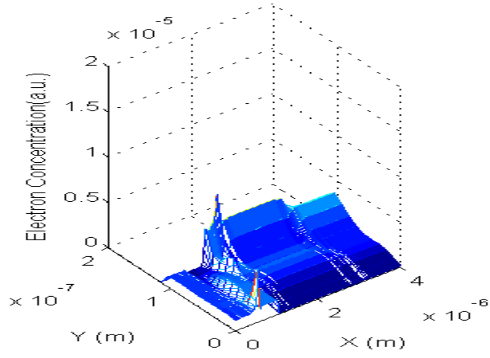
x 10^-5
Electron Concentration(a.u.)
x 10^-7
Y (m)
x 10^-6
X (m)

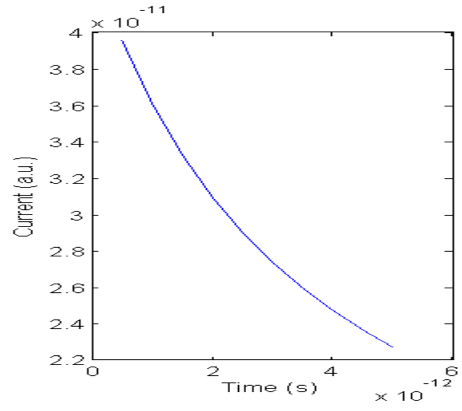
x 10^-11
Current (a.u.)
Time (s)
x 10^-12

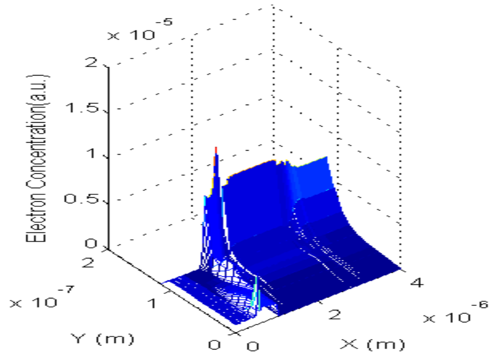
x 10^-5
Electron Concentration(a.u.)
x 10^-7
Y (m)
x 10^-6
X (m)

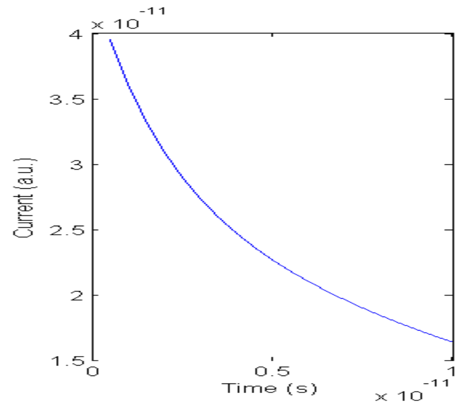
x 10^-11
Current (a.u.)
Time (s)
x 10^-11

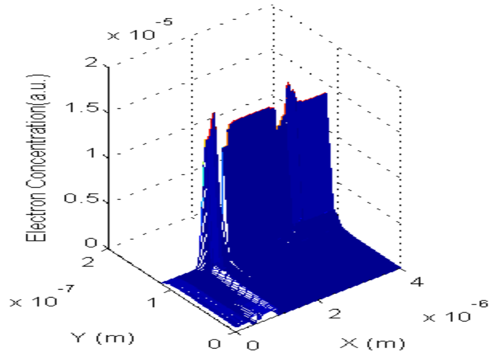
x 10^-5
Electron Concentration(a.u.)
x 10^-7
Y (m)
x 10^-6
X (m)

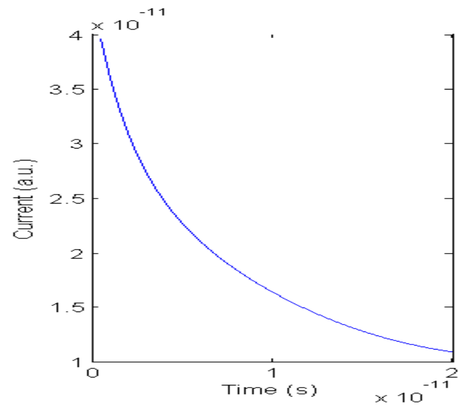
x 10^-11
Current (a.u.)
Time (s)
x 10^-11

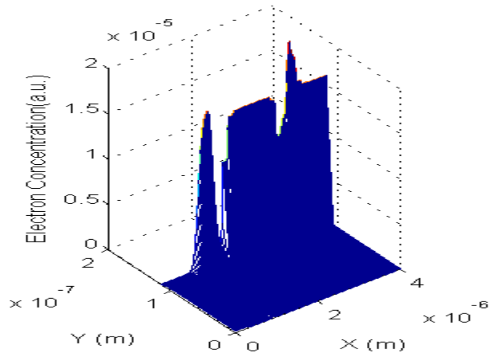
x 10^-5
Electron Concentration(a.u.)
x 10^-7
Y (m)
x 10^-6
X (m)

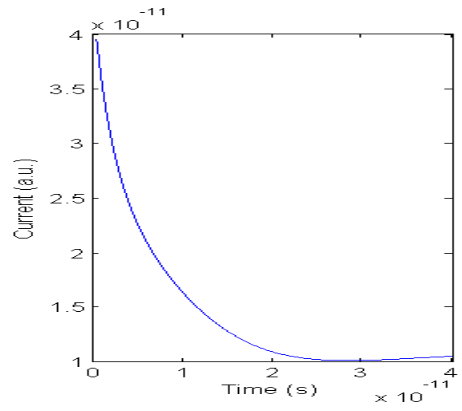
x 10^-11
Current (a.u.)
Time (s)
x 10^-11

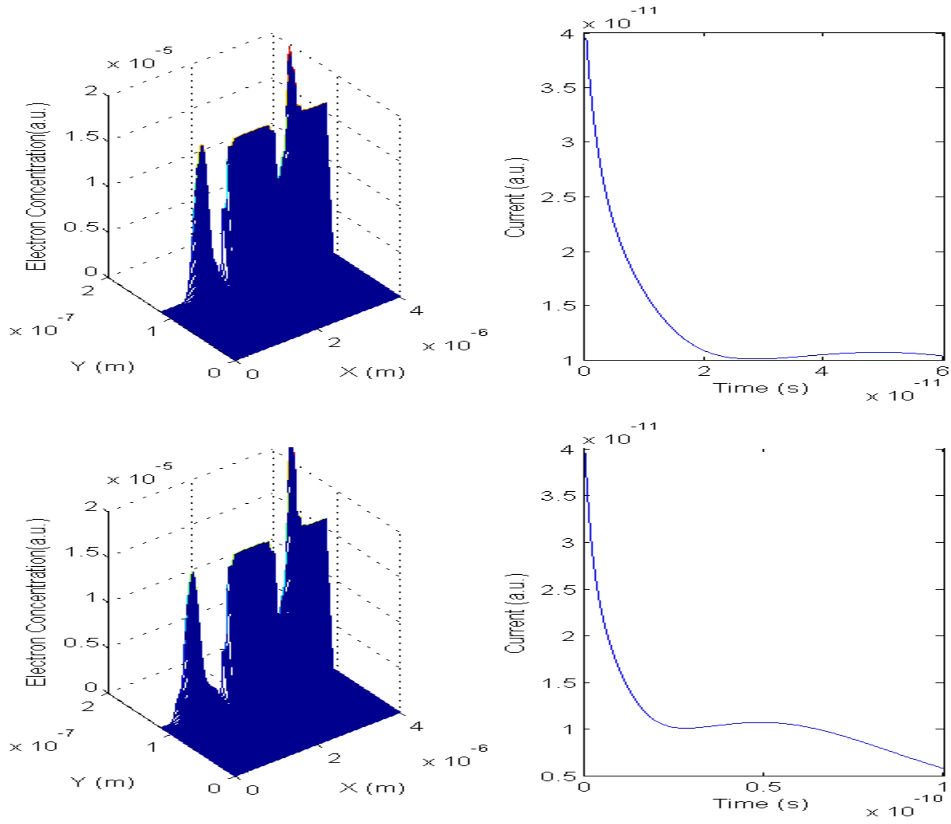

Figure 3.23 Evolution of the electron concentration and corresponding contribution to the photocurrent.

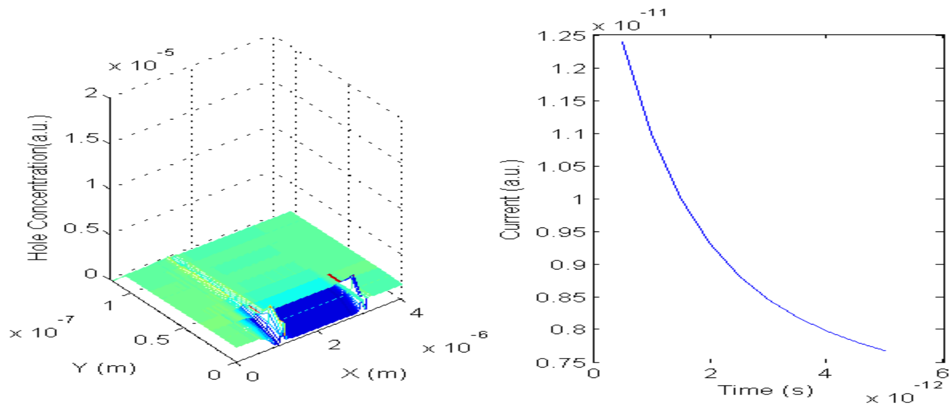

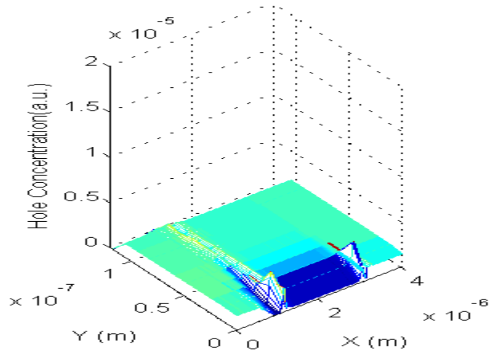
x 10^-5
Hole Concentration(a.u.)
x 10^-7
Y (m)
X (m)
x 10^-6

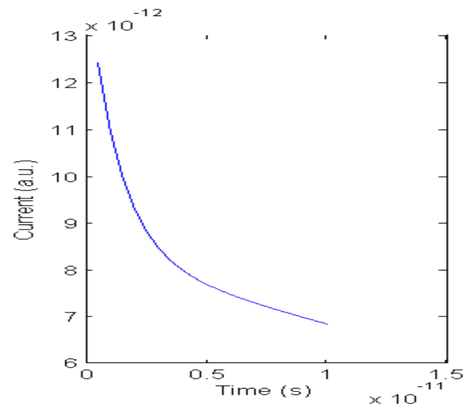
x 10^-12
Current (a.u.)
Time (s)
x 10^-11

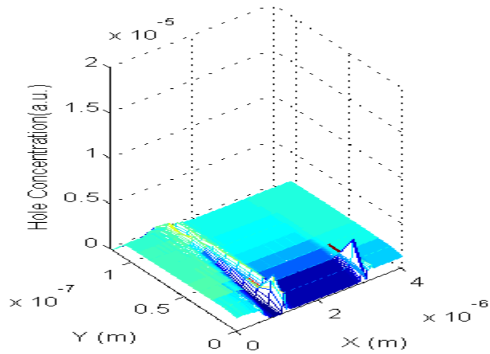
x 10^-5
Hole Concentration(a.u.)
x 10^-7
Y (m)
X (m)
x 10^-6

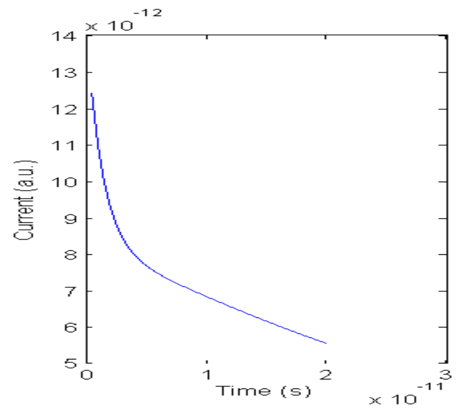
x 10^-12
Current (a.u.)
Time (s)
x 10^-11

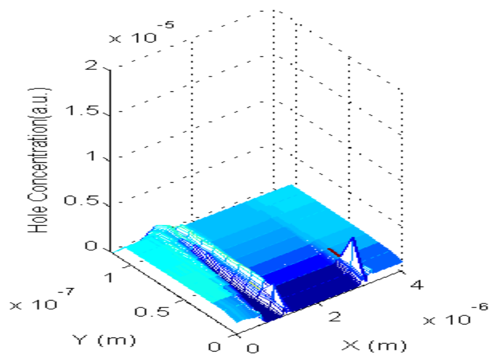
x 10^-5
Hole Concentration(a.u.)
x 10^-7
Y (m)
X (m)
x 10^-6

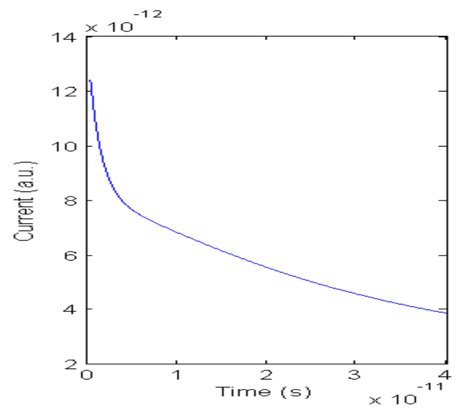
x 10^-12
Current (a.u.)
Time (s)
x 10^-11

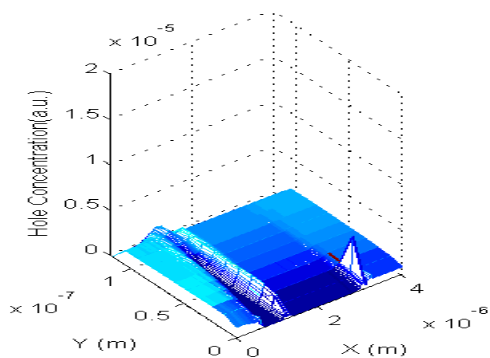
x 10^-5
Hole Concentration(a.u.)
x 10^-7
Y (m)
X (m)
x 10^-6

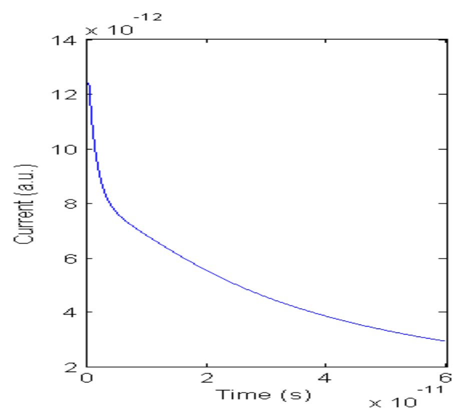
x 10^-12
Current (a.u.)
Time (s)
x 10^-11

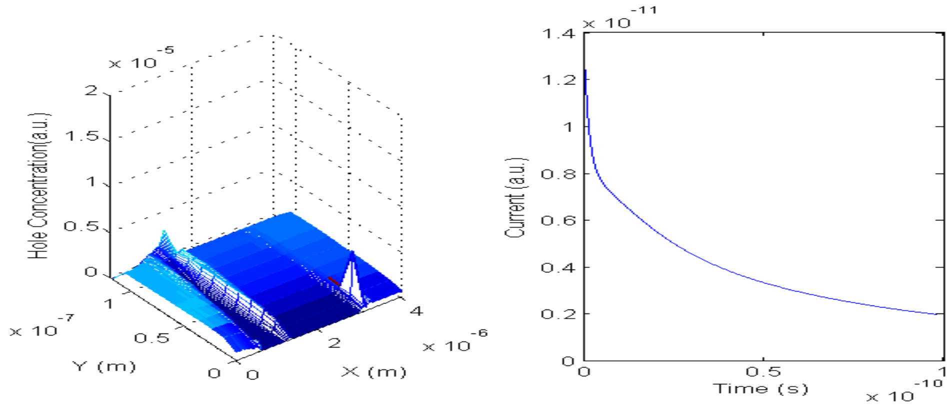

Figure 3.24 Evolution of the hole concentration and corresponding contribution to the photocurrent.

We observe that, within the first 2-ps, motion of photogenerated carriers, both electrons and holes, creates the first peak immediately after their generation due to vertical movements of carriers, as shown in Figure 3.23 and Figure 3.24. More interestingly, contrary to all previous time response, a second peak is generated from electron motion thereafter due to the electrons motion in the complete depletion region.

Given the 2-D electrical field distribution above, we divide the absorption region into two adjacent regions as shown in Figure 3.25(a), the complete depletion region of Schottky junction right underneath the anode, which extends accordingly to the external voltage; and the vertical field region filled with 2-DHG extensions or background doping. The simulation result verifies the existence of the two regions, as shown in Figure 3.25(a), which is the two-dimensional potential distribution at external voltage of 5V. Figure 3.25(b) also illustrates the 2-D electrical fields and movement of the electrons and holes in the absorption region schematically.

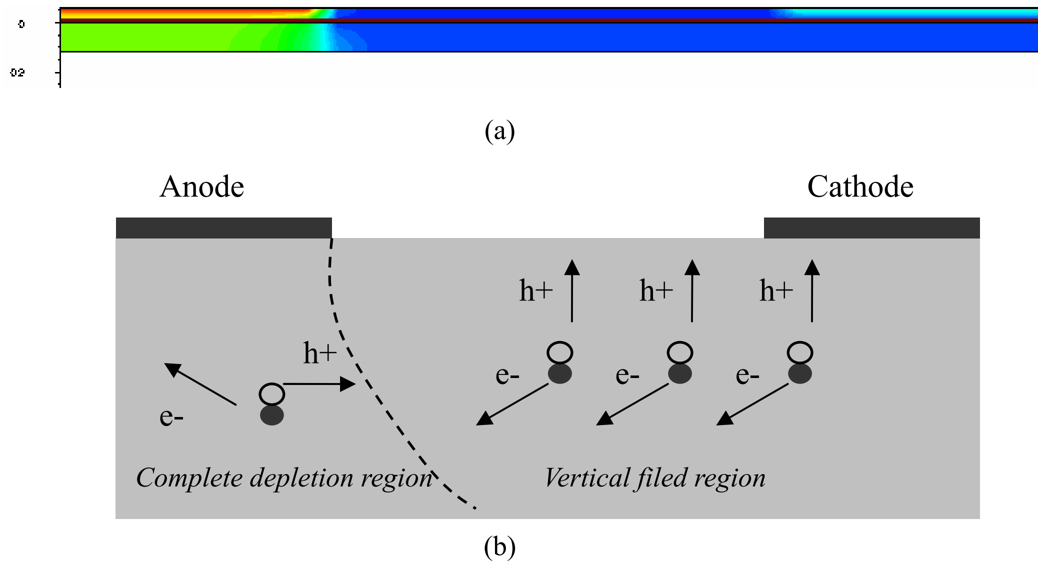

Figure 3.25 (a) The schematic diagram of carrier movement in the absorption region (b) Two-dimensional view of the potential distribution at V=5.

Here we analyze the contributions of electrons and holes from above two regions to photocurrent in detail. After the generation of electron-hole pairs, electrons move to the anode and holes move to the cathode. Electrons generated in the complete depletion region are collected by the cathode and make contributions to the first peak of the photocurrent. Electrons generated in the vertical field region firstly follow the vertical field move toward the bottom of the absorption region, making contributions to the first peak of current, then subsequently enter the complete depletion region creating the second peak. Holes generated in the vertical field region make contributions to the first peak of the photocurrent by drifting toward the 2-DHG. The holes generated in the complete depletion region make contributions to the first peak and stop making contributions since they are trapped at the bottom of the absorption region due to the extremely small vertical field. The peak in hole concentrations at the bottom is the singularity point in mathematics since the small field there can not dissipate the carriers effectively. Physically, those carriers are trapped there. Those trapped carriers do not make contributions to the photocurrent, which is one of the reasons that we expect small responsivity in the

measurements.

Complete time response of both electron and hole were calculated as follows. Comparison of time responses between doped 2DHG devices and undoped devices are shown in Figure 3.26 under 5V external voltage. The contributions from electrons and holes are separated as shown in (a) electrons, and (b) holes, respectively.

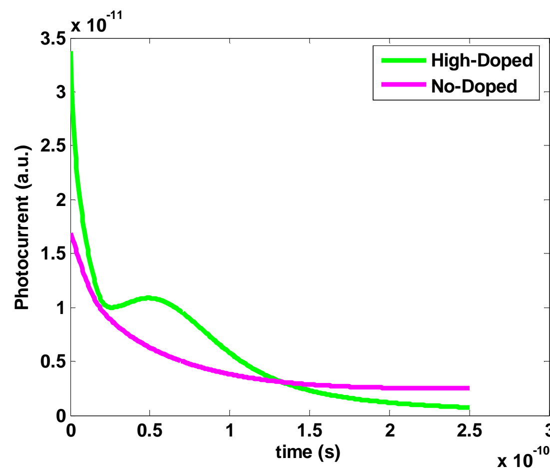

(a)

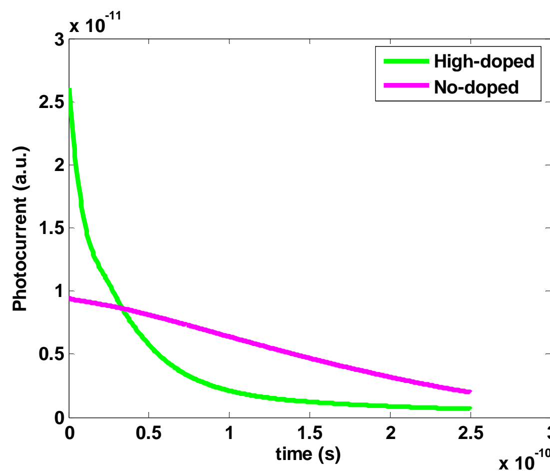

(b)

Figure 3.26 Time evolution of electrons (a) and hole (b) in doped and undoped devices.

The results of time response shown above are the intrinsic response, which do not contain other

components, such as, circuit parasitic parameters and measurement system responses. That is also the reason that we do not see the rise time, contributed by the system, appearing in the time responses. The figure in comparison of the electron contributions, shown in Figure 3.26(a), plots a two-stage response, namely two peaks of photocurrent appearing at time axis sequentially, in doped device, as we analyzed above.

Figure 3.26(b) shows the comparison of the photocurrent contributions from hole for doped and undoped devices. It indicates an obvious abbreviated tail in the time response for doped device. This is exactly what we expected for the hole dynamics. As we find out, hole transport is greatly enhanced in the time response, though the electron experienced long time.

3.4.2.3 Summary

The area of complete depletion region, developed underneath of anode, extends toward the cathode in accordance with the applied external bias.

We see two peaks in time response. The first peak is due to the transport of carrier in the vertical field region and the second due to the subsequent drifting of electron to the complete depletion region.

3.4.3 Experimental results, Observations and Analysis

The high-speed time response measurements were performed by Dr. Marc Currie and Eric Gallo at Office of Naval Research in Washington D. C., using a mode-locked Ti: Sapphire laser, operating at a repetition rate of 76-MHz that generated radiation with pulse width of 100-fs at a wavelength of 850-nm. For this 2-DHG device, we do not expect high-speed response since the device is designed to study the slow carrier dynamics at the expense of sacrificing the fast component, contribution from electron transport. However, the long tail in the response due to holes, the slow carriers, is meant to be reduced.

In any time response, as the simulation predicted, we observe photocurrent peaks at two different time spots. Figure 3.27 plot the time response at 10-V for low doped W2G2 device in time domain Figure 3.27(a). Frequency domain response based on Fourier transform of time domain is shown in Figure 3.27(b). The 3-dB frequency is 2.8 GHz.

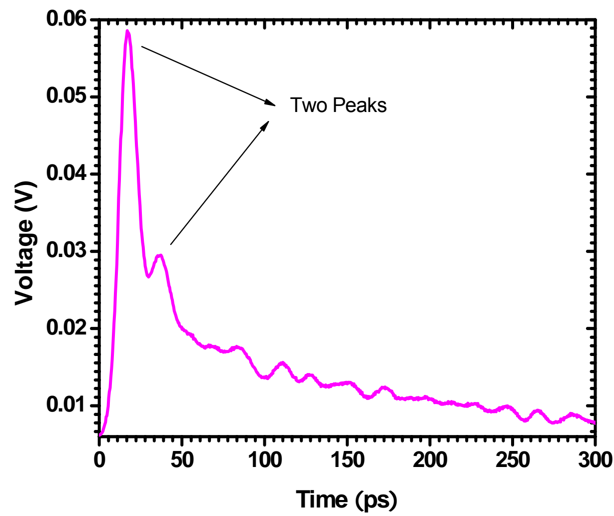

(a)

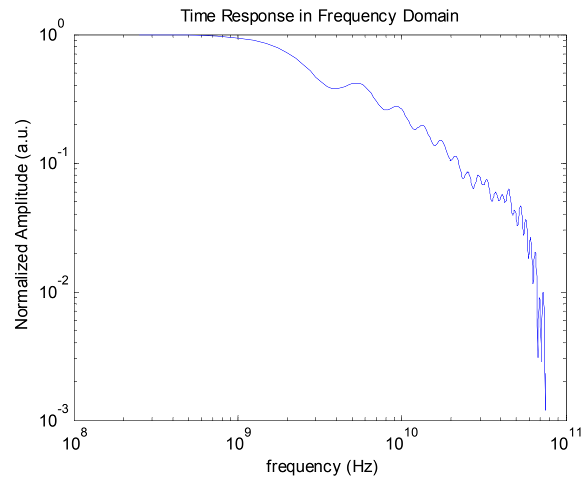

(b)

Figure 3.27 (a) Transient time response for W2G2 device at voltage of 10 V (b) Corresponding response in frequency domain.

As previously shown in the simulation, the absorption region can be divided into two regions according to the electrical field distribution. The motion of photogenerated carriers, both electrons and holes, in the vertical field region constitutes the major component of the first peak in the time response. As the electrons drift out of the vertical field region, they enter into the bottom of the complete depletion region subsequently; therefore, they create the second peak.

Amplitudes of the photocurrent in the time response for 2-DHG device present a voltage dependency; however, the FWHM of the first peak remains unchanged. Figure 3.28(a) plots the time response at different external voltages for W2G2 device on low doped wafer, (b) plots the corresponding normalized response. We observe from the figures that the amplitude of the first peak increases accordingly to the voltage applied ranging from 3-V to 20-V in Figure 3.28(a). The normalized signals in Figure 3.28(b) show that the FWHMs of the first peak are about 12-ps for any external voltages applied. The rise time is about 10-ps.

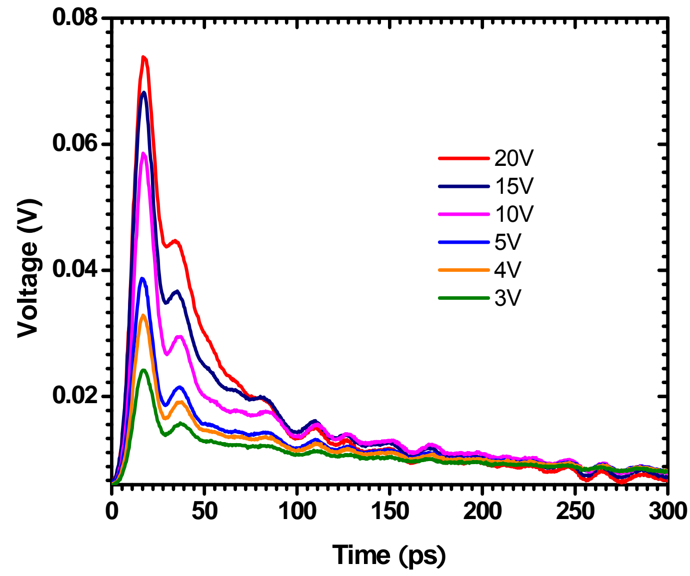

(a)

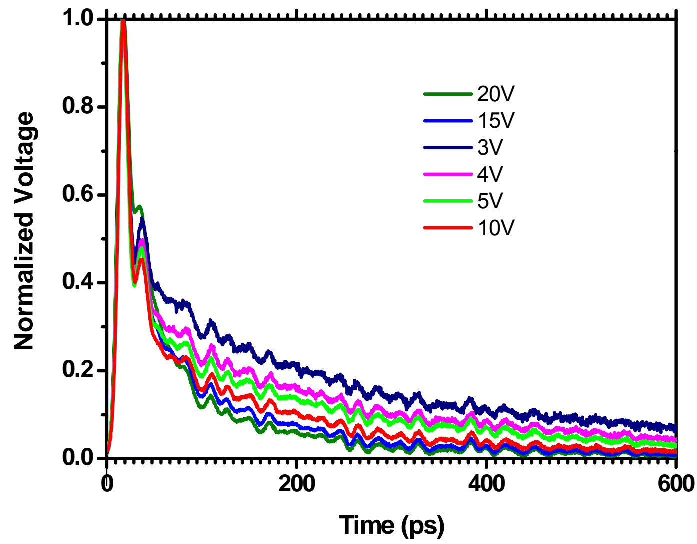

(b)

Figure 3.28 (a) Time response at different external voltage (b) the normalized response.

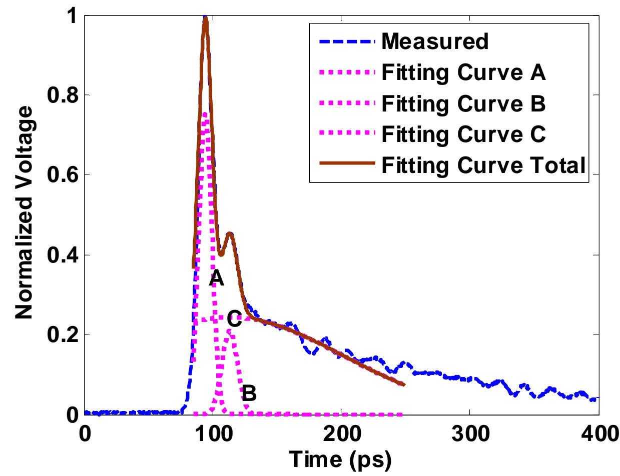

Figure 3.29 Three components of the time response.

To give a more quantified analysis, we break the time response in Figure 3.28(a) down to three components for all voltages. As shown in Figure 3.29, the time response under voltage of 15-V can be represented by three Gaussian distributions with different sigma σ, which represents the FWHM information for each component. We fitted all the curves in Figure 3.28(a) and listed the σ as follows.

Table 3.2 Parameters for curve fitting of time response with Gaussian distributions.

Voltage (V)	σ_A(ps)	σ_B(ps)	σ_C(ps)
20	5.1	8.0	45
15	5.1	7.0	70
10	5.0	6.1	80
5	4.8	5.6	95
4	4.8	5.6	110
3	4.8	5.6	120

As we note from the table, the first peak, represented by curve A, shows similar σ_A for all voltages, as we observed in Figure 3.28(b), though minor difference still exists between high and low external voltage. The σ_As under higher voltages exhibit somewhat larger value, and we attribute that difference to the distribution of the vertical field along the growth direction in vertical field region. As we see in Figure 3.21(b), the vertical field under higher external bias does vary from that under low bias.

As a matter of fact, the first peak consists of 4 components; which corresponds to the electrons and holes generated at complete depletion and vertical field region, respectively. As we see in simulation results Figure 3.25(a), most of carriers are generated at vertical field region, the time response is determined by the dynamic behavior of the carrier in that region. The vertical field does not vary with the external bias, as shown in Figure 3.22, thus the dynamics of carrier exhibit similar FWHM under different applied bias. Furthermore, the FWHM of the first peak is dominated by the hole dynamics since it is slower than electrons, as they were subject to the same vertical field.

The extension of the field is not uniformly in the absorption region due to the screening effect of the 2-DHG. As shown in Figure 3.30. Figure 3.30 (a) shows the simulation results of the two dimensional potential distribution under different voltages with real device structure. The extension of front line of depletion region is extended toward the cathode. To better present the trends of extension of potential, we used absorption thickness of 1-μm. Figure 3.30 (b) shows the simulation results of the potential as applied voltage goes to 5V, though the extent of the extension might have minor difference for thinner device.

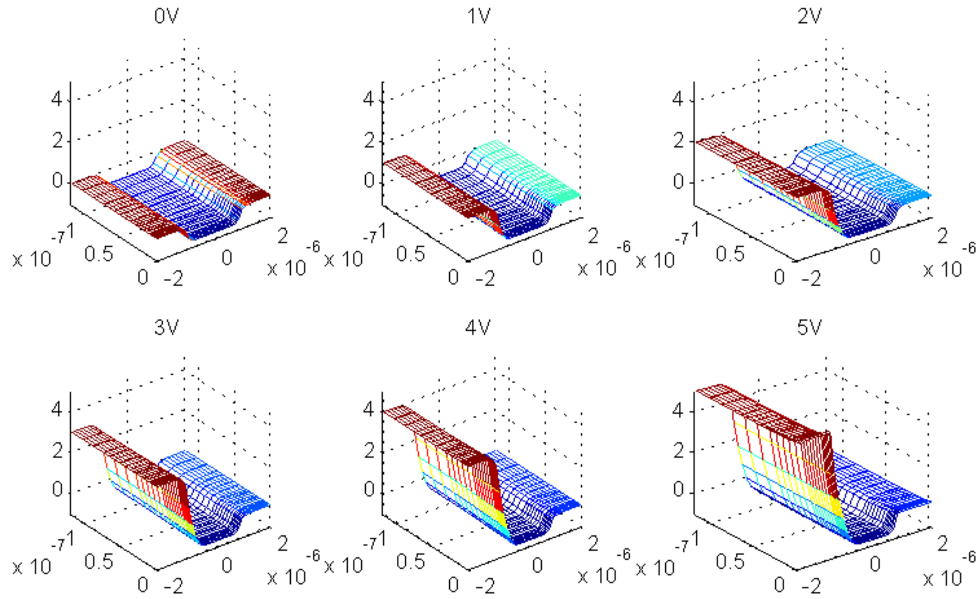

(a)

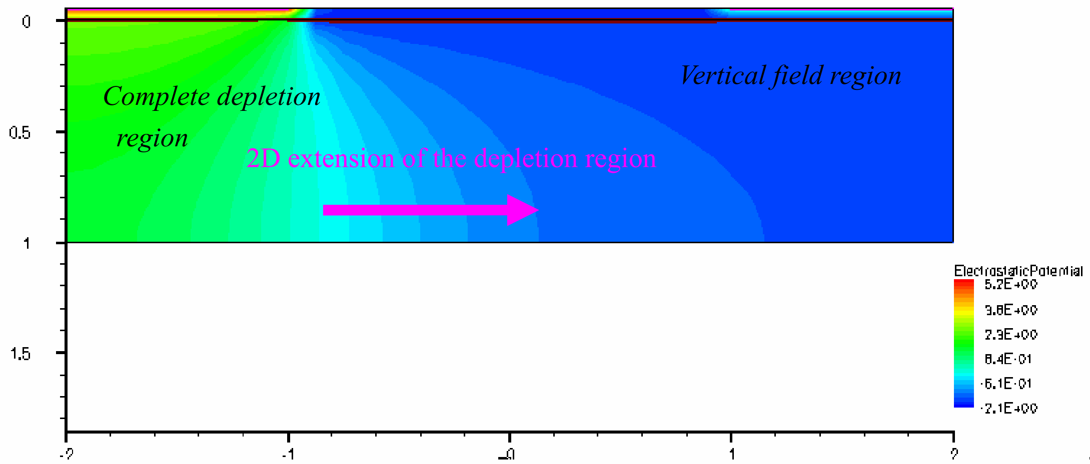

(b)

Figure 3.30 (a) 2-D extension of depletion region with increased external voltages for absorption thickness of 118-nm (b) for absorption thickness of 1-μm.

The carriers generated in the complete depletion region give rise to the difference in magnitudes of time response when they are subjected to the different external bias. As we see, in low doped device, the depletion region does extend laterally with external bias. The complete depletion region covers ever larger area, thus longer transit time experienced by the carriers in that region, as the device is

subjected to larger external bias. On the other hand, the electrical field in that region, both lateral and vertical components of the fields, increase, which we have observed previously in Figure 3.21. The increasing field compensates the extended transit time, thus more carriers in the vertical field region move at faster speed contributing to the increasing amplitude in the current response.

The fall time of the second peak is inversely proportional to the external voltage applied. Figure 3.31 plots the normalized second peak for low doped W2G2 device. We notice that the fall time is strongly influenced by the voltage, the higher the external voltage, the faster the decay. The time response takes longer and longer time to decay as external voltage decreases.

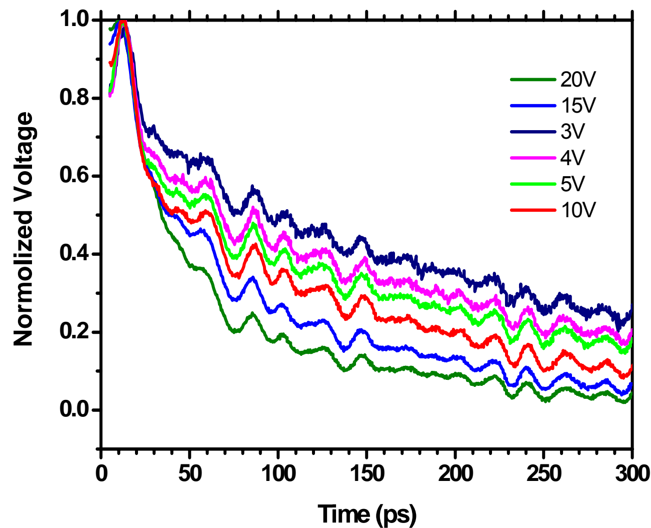

Figure 3.31 Normalized second peak for W2G2 device on low doped wafer at different voltages.

The dynamics of the second peak is largely due to the electron moving in the complete depletion region. The tail can be decomposed into two distinct components as shown in Figure 3.29. One is mainly due to holes, generated in the complete depletion region migrate, to the vertical field region,

represented by curve B in Figure 3.29. The dynamics represented by σ_B show similar trends as the first peak represented by σ_A; that is, σ_B is larger under higher voltages applied. The reason for that is also due to the distribution of the vertical field when the device is subjected to different external voltages in that region. The other component of the second peak, represented by curve C in Figure 3.29, exhibits obvious voltage dependence. This is due to the electrons generated in the vertical field region entering into the complete depletion region. There are large amount of electrons generated in the vertical field region drifting to the bottom of the device; it takes them a long time to drift along the lateral field at the bottom of the device and subsequently entering into the complete depletion region. The time scale is about several tens of picoseconds.

The response for different geometries is compared in Figure 3.32 for low doped W2G2 and W2G4 devices. The external voltage for both devices here is 20-V. In terms of the second peak, the longer device, G4 namely, shows larger amplitude than G2 device.

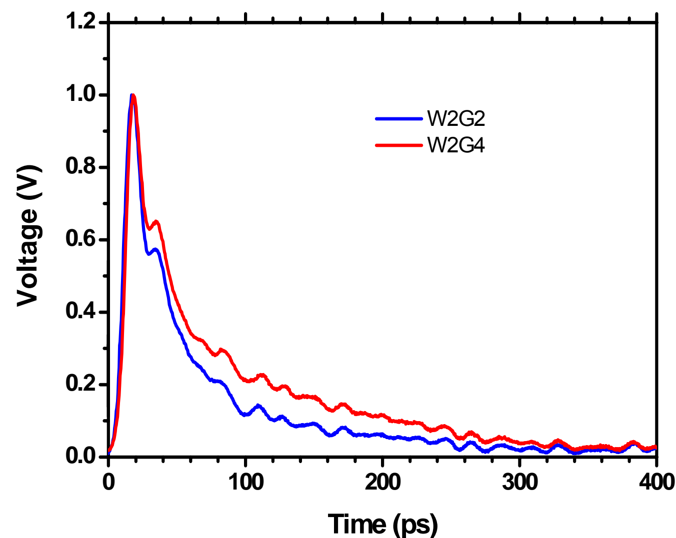

Figure 3.32 Normalized time responses for geometries of G2 and G4 devices on low doped wafer.

From the normalized response, we observe that the dynamics of the first peak are the same for both G2 and G4 devices. However, G4 device exhibit an obviously longer tail compared to the G2 device. And under normalized condition, the amplitude of the G4 device is greater than G2 as the second peak is concerned.

The first peak is related to the thickness of the absorption region, and is not affected by the dimensions of finger gap in view of the back-to-back Schottky configuration. The second peak is due to holes transit in the vertical field region and electron transit in the complete depletion region. We can see the slope, indicated by the black solid lines, of the first stage for the W2 and the W4 devices do not show too much difference, that is mainly because that the hole dynamics in the vertical field region are less subjected to the influence of device lateral dimensions. The slope of the second stage for the W4 device differs from that of the W2 one, since the electrons move at bottom of the device subject to the lateral field, which does vary from finger gap to finger gap.

Observations in this figure verify our previously analysis regarding the electron and hole transport in the absorption region.

For devices on highly doped wafer, all the time response traces present a much larger second peak in terms of the amplitude than devices on low doped wafer. The second peak almost dominates over the first peak in the responses. Figure 3.33 shows the time response for high doped W2G4 device under different external voltages.

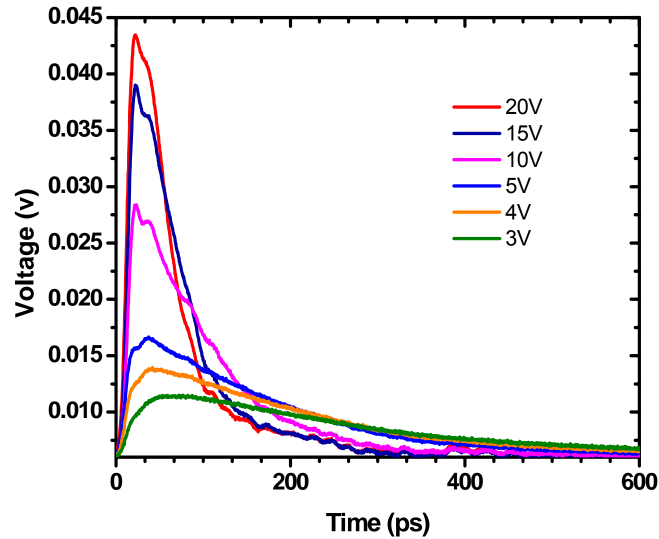

Figure 3.33 Time response for high doped W2G2 device under different external voltages.

As in the low doped device, high doped device also exhibit two peaks. The peak positions at time axis are the same for all the current at different voltages. Considering the amplitude of the two peaks, the second peak is explicitly stronger than the response from the devices on low doped wafer. The first peak shows similar FWHM and the fall time of the second peak decreases significantly as voltage increases. As voltage reduces, the second peak gets increasingly dominant over the first. At V=3V, the first peak has been completed overshadowed, and can not be differentiated from the time response any more.

The major difference of the high doped device from low doped device is their modulation doping levels, thus the 2-DHG concentration and vertical field in the vertical field region. Due to the high doping level in the δ-doping layer, the hole concentrations in the 2-DHG are higher than in low doped wafer. As a result, the complete depletion region covers less area than in low doped device due to the difficulty in depleting higher carrier concentration. This can be verified by comparing the simulated

lateral electrical field in the device between two structures. Figure 3.34 gives the electrical field cut in the middle of the absorption region, corresponding previous Figure 3.21 for low doped device. In this case, more electrons transport from the vertical field region to the complete depletion region and create higher amplitude of second peak of current compares to the low doped device.

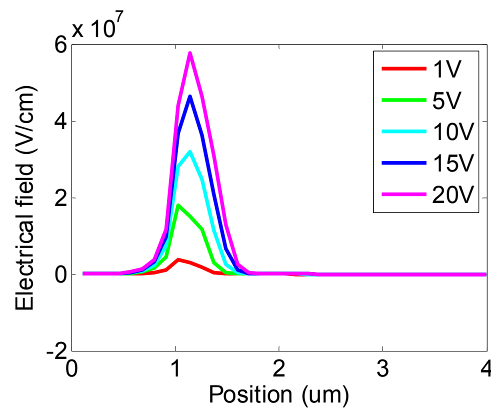

Figure 3.34 Lateral component of the electrical field cut in the middle of the high doped device

3.5 Conclusion

In this section, we presented experimental time response data, and analyzed them based on previous simulation results. The analysis is consistent with the observations we made from experiments.

We identified two major transport processes, in a consecutive manner, in the transient response as the 2-DHG photodetector subject to a pulse light. One is largely due to carriers moving in the vertical field region. The other is due to holes generated in the complete depletion region drifting to the vertical field region, and electron generated in the vertical field region drift to the complete depletion region.

The second peak in the time response can be further decomposed into two major components;

those are (i) a faster process, photogenerated holes moving under the force of the vertical field, and (ii) a slower process, photogenerated electrons drifting toward anode along the lateral field. Holes follow the vertical field; the dynamics of which does not vary too much with the applied field and dimensions of the electrode. Electron moving inversely along the lateral field, which is developed mostly at the bottom of the absorption region, contributes to the long tail, and its time response subject to the applied field and dimensions of the device.

Based on the above analysis of the experimental results, several conclusions can be drawn. In our experimental results, the time response of the second peak experienced a long fall time, which is due to the electron drift at the bottom of the absorption region, rather than slow holes transport as in all previous devices.

The 2DHG device created a vertical filed, which facilitates the hole collection and offer the potential to reduce the long tail in the time response.

The 2DHG is not well confined at the heterojunction and a lateral field is developed at the bottom of the absorption region. It creates a long traveling distance for electrons, thus is one of the major reasons of slow response in the 2DHG devices.

CHAPTER 4: CAPACITANCE-VOLTAGE CHARACATERISTICS

We have very interesting observations regarding the capacitance-voltage (C-V) characteristics from the 2-DHG device. The devices show very high Cmax/Cmin ratios and sensitivities. The optical modulated C-Vs present even more sophisticated profiles. With all the interesting electrical and optical properties, the 2-DHG device can be used as components in microwave and millimeter-wave circuits with extended applications beyond photodetectors.

C-V characteristics are one of the most important characterizations in semiconductor devices, such as metal-oxide-semiconductor (MOS) device. A variety of parameters can be determined by the C-V profile, such as, the insulator thickness, substrate doping, and threshold voltage in the MOS device[96]. The C-V profiling can also be used to determine the valence and conduction band discontinuities for heterostructure[97, 98].

C-V profile of the semiconductor device can also be used as varactors in parametric amplifiers and various frequency converting circuits [99], i.e. mixers, multipliers, VCOs, and tuned matching networks [100]. A large C_{max}/C_{min} ratio and a high quality factor Qc are desired properties in applications such as LC-tank voltage-controlled-oscillator (VCO) shooting for maximum frequency tuning. The high non-linearity and high sensitivity are desired for applications such as high order frequency multipliers. Symmetric C-V characteristics are desired for odd harmonic frequency generation.

4.1 Application for High Frequency Multiplier

In this Chapter, we present the C-V characteristics of our 2-DHG device, which turns out to be extremely suitable for applications in high odd-order frequency multipliers, where the symmetrical C-V remove the necessity for second-harmonic idler circuit or dc bias. Previously, Schottky diodes

[101] have been used for this purpose, however, heterostructure-barrier-varactors (HBV) offer the potential for better overall performance in terms of conversion efficiency and operation frequency due to their symmetric CV relation, which circumvents the idler and bias circuits in a multiplier, and their power handling capabilities. The first HBV was reported in 1989 [102], thereafter, a number of frequency triplers and quintupler have been reported based on this structure. Lheurette [103] reported enhanced nonlinearity C-V characteristics HBV in 1998. Meola [104] reported improved frequency tripler with HBV in 2000. Vukusic at. el. [105] reported HBV triper at frequency of 102 GHz with efficiency fo 21% in 2006. Xiao at. el. reported InP HBV quintupler at frequency up to 210 GHz with efficiency of 5% in 2004 [106]. More recently, heterostructures combined with Schottky contacts have also been reported. Marso at. el. [107] reported MSM-2DEG varactor with a Cmax/Cmin ratio up to 100 and a sensitivity up to 11. Anwar at el [108] reported optically controlled Schottky/2DEG varactors with capacitance variations of 30% from gate modulation in 2001.

The 2-DHG Schottky MSM structure compared to previous 2DEG devices, the charge distributions in various layers, and in the absorption region, are different, which eventually results in higher sensitivity of the C-V. The improved electrical and optical performances of these devices will be discussed. The devices demonstrate high nonlinearity and very low leakage current, allowing for high power conversion efficiency in frequency multiplier applications. Moreover, since the device was designed as photodetector, optoelectronic experiments show the non-linear C-V characteristics can be controlled by the intensity of optical radiation. It offers the potential for applications in optoelectronic mixing in Willimeter wave Integrated Circuit (MMIC) and Radio Frequency (RF) circuits [109]. The planar MSM structure allows them to be monolithically integrated into III-V technology.

4.2 C-V Characteristics

Capacitance-voltage measurements of the device were performed with a HP4284A precision LCR meter. Capacitance of device was obtained by subtracting the stray capacitance contributions. The measurements on both high doping with the δ-doping level of $2x10^{12}/cm^2$ and low doping of $5x10^{11}/cm^2$ were performed.

The C-V characteristics of the devices are shown in Figure 4.1. It was measured at probe frequency of 10-kHz. The external voltage swept from -5V to 5V. The two C-V curves were from the high doped (HD) and low doped (LD) devices.

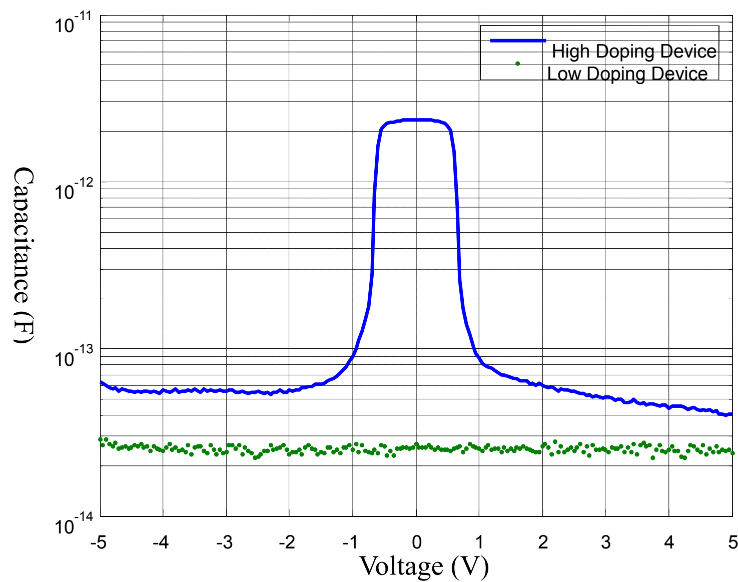

Figure 4.1 Capacitance-voltage characteristics of the high and low-doped devices in the dark at probe frequency of 10 kHz.

We observe significant differences between them in terms of C-V shape and values. The capacitance of the HD device has a peak of 2 pF and remains flat until about 0.7V, then sharply drops to a relatively low value of less than 0.02 pF, depending upon the electrode geometries. The ratio of

C_{max}/C_{min} at a probe frequency of 10-kHz was measured up to 113 for a device with no interdigital fingers due to its large electrode separations. The best results previously reported was around 100 by Marso based on MSM-2DEG structure with finger separations of 80-μm [106].

The varactor sensitivity is defined by $S = \frac{dC}{C}\frac{V}{dV}$. The sharp slope of the C-V as seen in Figure 4.1, gives a sensitivity of 35, which to our knowledge is the highest reported. This high sensitivity, based on highly non-linear C-V relation is particularly suitable for high order frequency multiplication applications.

4.2.1 Maximum Capacitance (Cmax)

The C-V profile is due to charge variations to the external applied bias. The difference between the C-V of HD and LD originates from the hole density in the two-dimensional gas. In LD, less charge is generated in the heterojunction, namely, the mobile 2-D gas has less density. The Schottky barrier height *Vs* itself is able to deplete it completely. Hence, we do not see any capacitance variations under external bias ranging from -5V to 5V. This is different for the case in HD. The flat peak at the low voltage suggest that the high density of 2-DHG requires an additional external applied voltage to deplete. The amplitude of C_{max} indicates the information of 2-DHG density. As the 2DHG carriers underneath of the contact are depleted, capacitance drops to a low value that is determined by the lateral depletion of the 2DHG. This will be shown in later simulation results.

In the HD device, the two-dimensional hole gas with its high sheet carrier concentration acts as an equipotential plane that confines the Schottky depletion zones to the region between the contact and the 2-DHG. The reverse biased Schottky and the 2-DHG right underneath it constitutes a planar plate capacitor. An applied bias voltage drops mainly across the reverse biased contact, leaving the capacitance of the forward biased contact invariant. Thus, a simple and straightforward estimation of

the C_{max} can be given [107]:

$$C_{\max}(0V) = \frac{\varepsilon_{AlGaAs} A}{d_{AlGaAs}} \tag{4.1}$$

where, the d_{AlGaAs} and ε_{AlGaAs} are the thickness electrical permitivity of the barrier enhancement layer, and A is the area of reverse biased electrode area. Given ε for $Al_{0.5}Ga_{0.5}As$ of 11.48 [73], measured thickness for $Al_{0.5}Ga_{0.5}As$ of 40-nm and area of half of 20x20 μm^2, the Cmax of our device is calculated to be 2.03-pF, which is consistent with the experimental measurements. In this simple model, only the charge contributions from the 2-DHG is accounted, and the capacitance is only a function of the area of the electrode of interest. This is consistent with what we observed in several C-V curves with different geometry configurations. It will be presented in Figure 4.2.

4.2.2 Minimum Capacitance (Cmin)

The capacitance of the reverse biased electrode remains constant until the 2-DHG is completed depleted; then drops sharply to capacitance minimum.

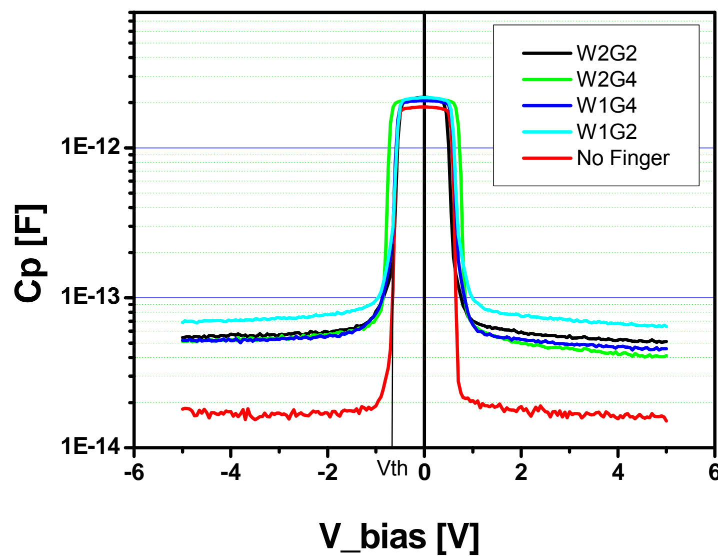

Figure 4.2 The C-V characteristics for different electrode geometries.

Figure 4.2 shows several electrode geometry-dependent C-V characteristics for HD. The W2G2 represents the finger width of 2 μm and finger gap of 2 μm, where the W stands for the finger width and G the finger gaps, the values are in the unit of micrometers. Minimum capacitances in this structure are quite dependent on the electrode geometry. We define a V_{th} the threshold voltage, such that as the applied bias exceeds it, the 2-DHG underneath the contact becomes completed depleted. The C_{max} remains invariant for most of the geometries as we predicted in the previous section. C_{min} differs from geometry to geometry. The lowest C_{min} is observed in the no finger device due to its electrode geometry configurations.

The influence of geometry to the C_{min} can be illustrated by the Figure 4.3. As the applied voltage exceeds the V_{th}, the depletion region penetrates laterally into the 2-DHG generating a capacitance C_{lat} that is in series with the $C_{schottky}$. As the external voltage is increased beyond the V_{th}, C_{lat} comes into play and dominants the capacitance behavior since $C_{lat} << C_{shottky}$ when $V > V_{th}$.

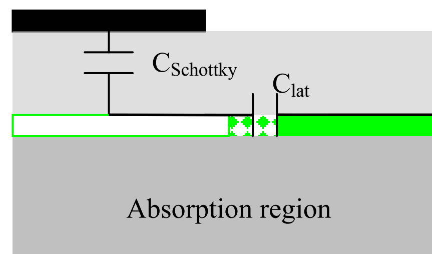

Figure 4.3 Lateral depletion of the 2DHG creating a capacitance determining the C_{min}.

The C_{lat} is related to the lateral depletion of the 2-DHG and can be derived from a model of 3-D metal contacting with 2-D gas [110].

The simplified model, presented by Gelmont [16], is drawn in Figure 4.4, a schematic diagram of

2-D gas contacting with 3-D metal. The model does not precisely describe the 2-DHG structure due to the way of Schottky contacting with 2-D gas, but it well represents the essence of case where a 3D metal meets a 2D gas.

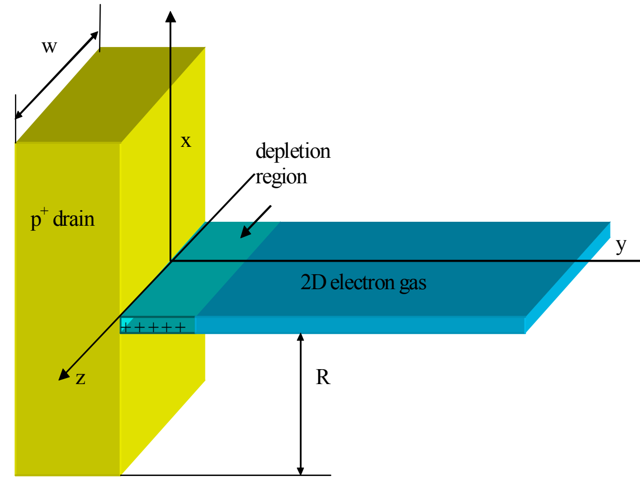

Figure 4.4 Simplified model of 2D electron gas – p-type semiconductor junction.

In Figure 4.4, R is half length of the contact, W is the width of the device, d_{dep} is the distance of the lateral penetration into the channel along y-axis, which can be calculated by:

$d_{dep} = \dfrac{2\pi V}{qN_s}$, where V is the voltage drop across the depleted channel region, and Ns is the 2DHG sheet carrier density. And the capacitance of 2-D gas due to the lateral depletion, the C_{lat}, related to the geometry of the device is derived as:

$$C_{lat} = \frac{dQ}{dV} = \frac{W\varepsilon}{\pi} \ln \frac{(R^2 + d_{dep}^2)^{1/2} + R}{(R^2 + d_{dep}^2)^{1/2} - R} \tag{4.2}$$

This Equation (4.2) explicitly relates the C_{lat} with the geometry of the electrode when $V>V_{th}$.

4.3 Optical Modulation of C-V

The optically modulated C-V characteristics were measured. One prominent observation of C-V under light is that, the sensitivity of the C-V characteristics can be controlled by the intensity of input optical power. The major reason for the observation of optically modulated behavior is that, the excess carriers, generated from the incident optical radiation, completely change the charge distribution in the device. The carriers have to rearrange themselves and reach a new thermal equilibrium with certain distributions in the device. Hence the charge variations with external bias differ from previous dark case, causing a totally different behavior of C-V profile.

Figure 4.5 shows C-V results under 850-nm laser at various intensity values at probe frequency of 10-kHz. It is observed that the sensitivity, namely the slope from the C_{max} to the C_{min} transition region of the C-V, is modulated by the intensity of the input optical power. High slopes are observed under lower intensities.

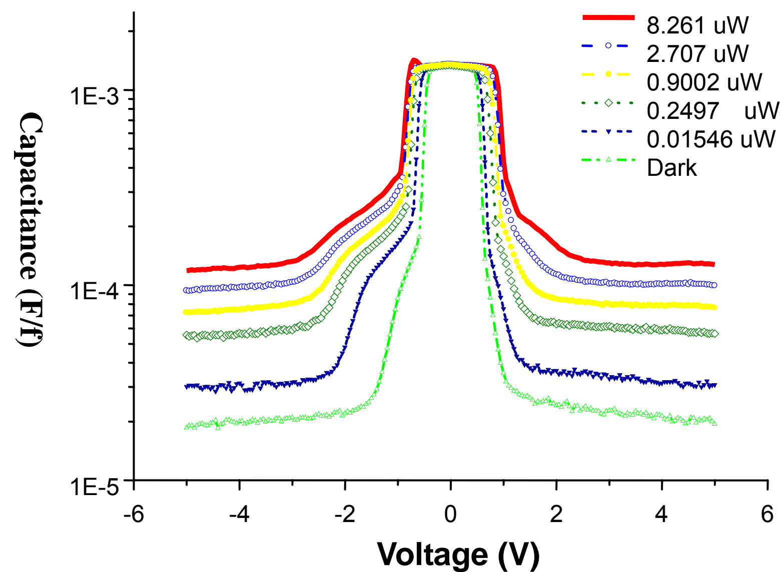

Figure 4.5 C-V characteristics under light at probe frequency of 10 kHz. The slope of C-V depends on the incident power levels.

Figure 4.6 shows the same modulation behavior at probe frequency of 1 MHz. As we see from above two optical modulated C-V characteristics at different probe frequency, they exemplify rich frequency dependent information. The C-Vs at both high and low probe frequencies show a tendency of slope increases around transition regions. At high probe frequency, as shown in the Figure 4.9, the flat top also present a slope variation with respect to bias voltage. This is because the frequency response of the 2-DHG underneath the electrode can not follow the high probe frequency. The increasing shunt resistance of the 2-DHG with voltage pushes the cut-off frequency to lower values, i.e. 1-kHz. This has been verified by previous Figure 4.2, where the frequency response of the capacitance decreases with the probe frequency, i.e at 1-MHz.

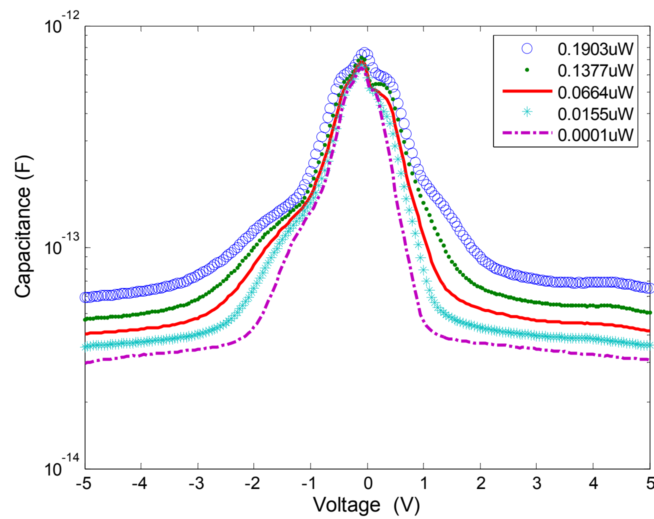

Figure 4.6 C-V characteristics under light at probe frequency of 1 MHz.

One more word regarding the optically modulated C-V characteristics is, we also observe the asymmetry at the peak of the C-V curve. The asymmetrical behavior is due to the trapped surface/interface charge. It has been experimentally demonstrated that, for p-type $Al_{0.5}Ga_{0.5}As/GaAs$

heterostructure, deep donor-like states are present, and are located immediately below the Fermi level in the spacer layer [111]. Under illumination, as the polarity of applied bias is switched, (the applied bias crosses 0V), the previously forward biased junction becomes reverse biased, and junction field at this reverse biased contact increases. The electrons photogenerated from these donor-like states present in the space layer are swept by the strengthened junction electric field into the quantum well and thereby recombine with holes in the 2DHG. This causes the reduction of the hole density in the quantum well. The reverse biased junction dominates the capacitance; therefore small variations in the 2DHG carrier density underneath the reverse biased junction create this observed asymmetric behavior.

4.4 Simulation and the Model

Device C-V behavior was simulated by ISE-TCAD using the small signal AC extraction based on a mixed-mode, where a circuit that combines devices from device simulator DESSIS in ISE is concerned. DESSIS computes the complex (small signal) admittance Y matrix, which specifies the current response at a given node to a small voltage signal at another node. The output contains the components of the conductance matrix and the capacitance matrix.

In this simulation, real device dimensions were used and the thickness of the active region was given at 117-nm. The simulated small signal C-V at a frequency of 10 kHz, compared with the experimental result, is given in Figure 4.7. The simulated result is consistent with the experimental one; the difference between the two is accounted for by the contact pads capacitance. The capacitance maintains at Cmax of 0.7-pF, and starts to drop to a Cmin of 0.04-pF at external voltage of about 1-V. To study the detailed C-V behavior, the potential and carrier distribution are investigated with the applied voltage increasing from 0 to 5-V.

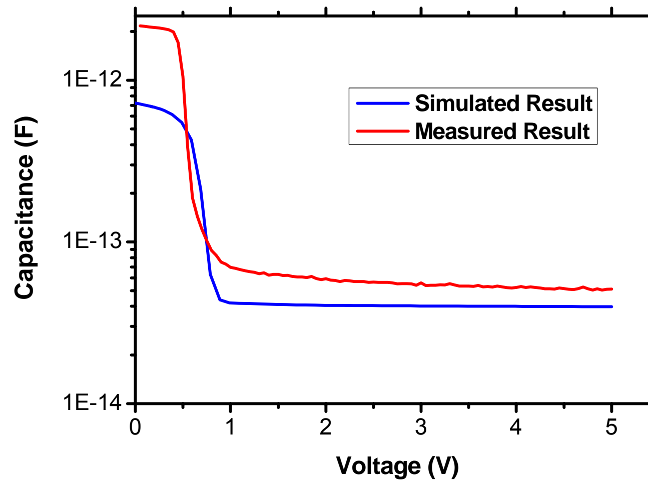

Figure 4.7 Simulated C-V characteristics for high doped W2G2 device.

Figure 4.8 (a) shows a two dimensional potential distribution of the cross section of the device at bias voltage of 5V. As seen in the figure, most of the voltage drops at the reversed biased anode electrode, with the depletion region extending vertically. The corresponding hole concentration along the growth direction cut in the middle of the device is shown in Figure 4.8(b), the two peaks represents the δ-doping and 2DHG respectively.

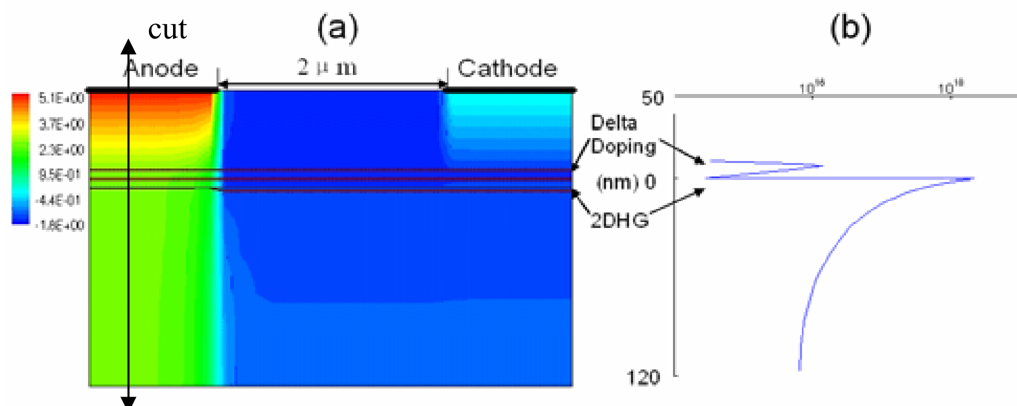

Figure 4.8 (a) Simulated potential distribution at 5-V bias voltage (b) Corresponding hole density at equilibrium.

Since the depletion region is developed underneath the anode, the corresponding variations of the hole concentration in that region is more of interest. To further understanding the C-V behavior, the hole concentration, cut underneath the anode as shown in Figure 4.8(a) is shown as follows. Figure 4.9 shows the corresponding hole concentrations at applied voltages of 0- 0.7V with a step of 0.1V.

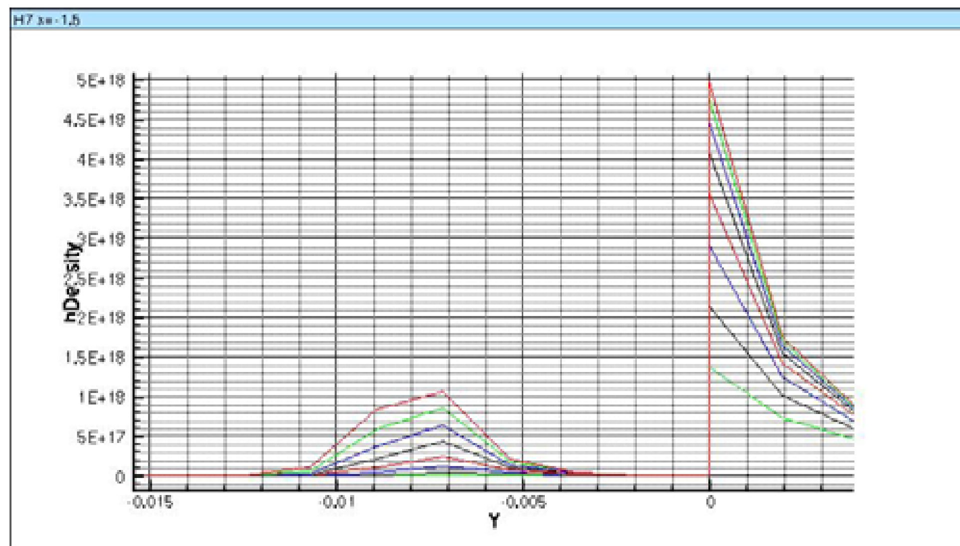

Figure 4.9 The hole distribution at voltage from 0 to 0.7V with step of 0.1V.

We can see that the holes concentrations in both delta doping and 2-DHG layer keep decreasing with applied voltage as V < 0.7-V. This is the stage where the capacitance remains at Cmax as shown in Figure 4.7. As the applied voltage increases above 0.7-V, the hole concentration have been deplete underneath of the anode, the capacitance sharply drop to a Cmin. At V=5-V, the holes underneath the anode have been completely depleted as seen from the potential distribution. Above observations suggest that C-V behavior is accounted for by the hole concentration in the delta and 2-DHG layer.

Based on above simulation results, we analyze 2-DHG structure and propose a model to describe the C-V behavior. An equivalent circuit of the 2-DHG structure can be represented by Figure 4.10.

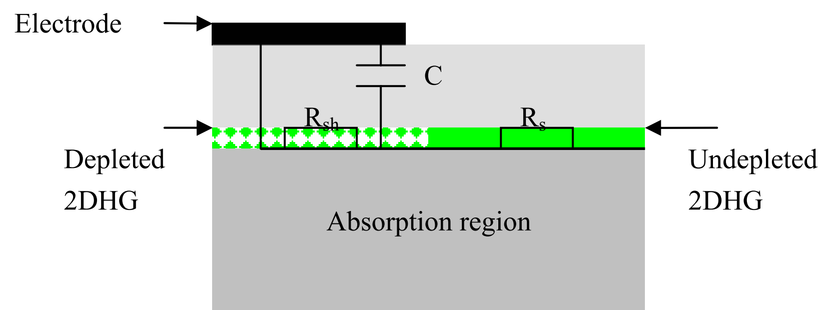

Figure 4.10 The equivalent circuit of the 2-DHG structure.

Figure 4.4 comprises all the components of the capacitor those contribute to the capacitance, which will be addressed below. R_{sh} shows the shunt resistance which is the depleted 2-DHG, the portion right underneath the contact. The R_s, series resistance, represents the undepleted 2-DHG, which affects the operation frequency of the device. Here we differentiate the R_{sh} with series resistance of the device R_s. The R_{sh} is in parallel with the capacitance, and is obtained by the probe frequency variation.

In previous similar structure varactors [107], CV behavior was modeled as parallel plate capacitors. In this case, all components of capacitance due to the more complicated charge distributions should be considered. These consist of C_0, C_{gas}, C_{delta} and C_{lat} components modeled as Figure 4.11, representing the capacitance due to background charge in the bulk, the mobile charge in 2DHG, and undepleted charge in δ-doped layers, and the lateral depletion of the 2-DHG, respectively. The background charge can include bulk unintentional doping and the photogenerated carriers in the bulk absorption region. R_0, R_1, R_2 are associate series resistors. R_{sh} is the shunt resistor of the 2DHG, as we discussed before. Since most of the charge variations with voltage occur at the reverse biased junction, the components from forward biased junction are omitted.

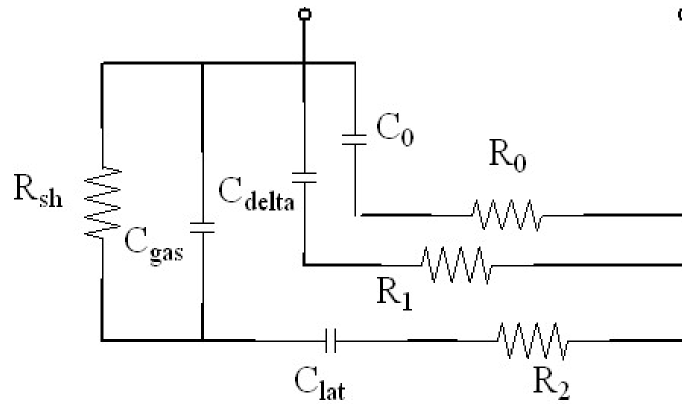

Figure 4.11 Proposed circuit model, including C0, C1 and C2, representing contributions from background charge, delta-doping layer, and 2DHG, respectively.

Under no bias, capacitance is at maximum due to combination of three stored charge sources, 2-DHG charge, δ-doping, and background charge. With bias, it remains constant until charges underneath the anode are depleted vertically. This regime corresponds to the flat peak in the C-V characteristics, and the charge variations are largely due to the δ-doping layer and the 2-DHG underneath the anode. With further increase of bias, as Figure 4.8(a) shows, δ-doping and 2DHG charge start to be depleted laterally by a small Debye length which make extremely small contributes to total capacitance. In this regime, C_0 the contribution from background charge becomes dominant, which determines the slope of the C-V profile from Cmax to Cmin. In our device the small bulk region possesses less background charge, resulting in high sensitivity of the device. The difficulty in lateral depletion of the 2DHG causes a steep drop of capacitance, which also accounts for this high sensitivity.

Further simulations also indicate that the shape of C-V can be engineered by the charge distribution between the δ-doping layer and the 2D gas. Figure 4.12 shows the C-V profiles with different charge distributions between δ-doping layer and 2-DHG. This was implemented in the simulation by changing the ΔE_v manually. The legend in Figure 4.12 represents ΔE_v of 0.09, 0.16, 0.25,

0.28, 0.30-eV, respectively.

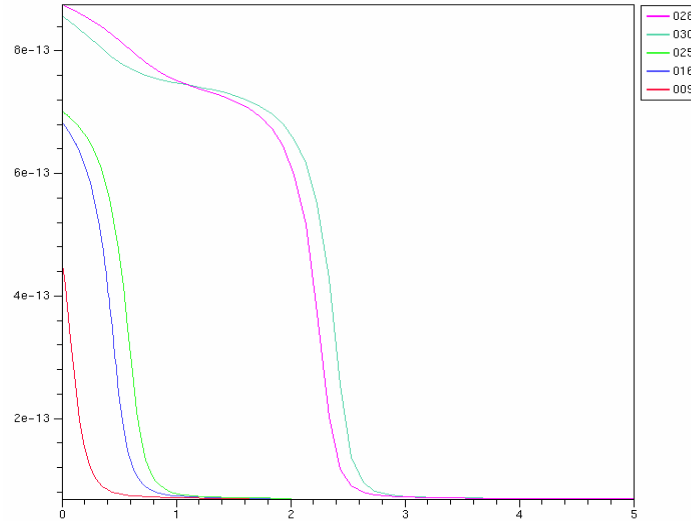

Figure 4.12 C-V profiles at different charge distributions between δ-doping layer and 2-DHG. The C-Vs presented corresponds to the heterostructure with ΔE_v of 0.09, 0.16, 0.25, 0.28-eV, respectively. X axis is the voltage, y axis is the capacitance.

The corresponding concentrations in δ-doping layer and 2-DHG are listed in the following table.

Table 4. 1 Hole concentrations in 2-DHG and δ-doping layer at different valence band offsets ΔE_v

ΔE_v(eV)	2-DHG(/cm^3)	δ-doping(/cm^3)
0.09	6.1x10^{14}	1.5x10^{16}
0.16	6.4x10^{15}	4.0x10^{17}
0.25	7.0x10^{14}	7.3x10^{17}
0.28	6.5x10^{17}	7.2x10^{18}
0.30	3.9x10^{17}	9.0x10^{18}

As we observe from the table, Cmax is directly related to the carrier concentrations in the charge sources, the higher carrier concentration, the higher Cmax. On the other hand, the higher concentration in the δ-doping layer 2-DHG shift the transition voltage from Cmax to Cmin. It can be understood in a way that, more voltage is required to deplete the charge. Enough carrier concentration in the δ-doping

layer and 2-DHG ensures to maintain a high level of Cmax. And higher concentration in the δ-doping layer may cause different C-V profiles at lower voltages.

Under illumination, photogenerated carries create more background charge, which essentially changes the charge distribution profile in the bulk, hence the voltage dependent charge variations, namely, the C-V characteristics. This, as shown in Figure 4.6, allows for the sensitivity of the varactor to be controlled by illumination. More importantly, since this is a photodetector device, it allows for interaction of optical and microwave signals. The extra background charge due to photogeneration, contributing to C_0, modifies the steep drop of capacitance. This explains previous optical power modulated C-V behavior.

4.5 Discussions

The C-V characteristics can be used to determine some structure parameters as we mentioned before, such as, the substrate doping, and threshold voltage in the MOS device [96], the valence and conduction band discontinuities for heterostructure [97, 98]. Here we take advantage of the C-V characteristics and discuss estimation of some parameters of the structure.

(1). 2-DHG sheet density: Due to the parallel conduction, the Hall measurements can not be used for an accurate estimation of the sheet carrier density and the carrier mobility [112-114]. The direct measurement of carrier densities and mobility requires more sophisticated facilities. From the C-V measurement results, we can briefly estimate the 2-DHG carrier concentration and the series resistance of the device.

An estimate of the 2DHG sheet density can be obtained from charge control model: $N_s qA = C_0 V_s$, where, Ns is sheet carrier density, A is the area of the device area, C_0 is capacitance measured at zero volt, Vs is the voltage swing required to deplete the 2DHG. These values

are obtained from measurement, where we estimated *Ns* for high doping device is $5.5\text{x}10^{11}/\text{cm}^2$. Considering the undepleted charge in Delta doping layer, this *Ns* may need to be adjusted to a lower value. This value is also consistent with the usual calculation for HEMT structures given the nominal doping level.

(2). Series resistance: the series resistance is comprised of three parts: contact resistance (*Rc*), (approximately 1Ω), channel resistance (*Rch*), and resistance of the Schottky junction metal(*Rg*), namely, *Rs = Rc+Rch+Rg*, where, *Rc* is negligible, *Rg* is technology-dependent and small, hence, the *Rch* is the dominant resistance in these devices and is the largest. In our device, *Rch,* is primarily represented by the 2DHG resistance outside of the depletion region and can be estimated from the sheet carrier density:

$$R_s \cong R_{ch} = \frac{1}{q\mu N_s}\frac{W}{LM} \tag{4.3}$$

where, *M* is the number of fingers, *W* is the width of finger length. Assuming a conservatively estimated mobility of 500-cm^2/V [115], we can estimate *Rs=113*Ω.

(3). Dynamic cut-off frequency: The dynamic cut-off frequency is defined as follows [116],

$$f_{RC} = \frac{1}{2\pi R_s}\left(\frac{1}{C_{\min}} - \frac{1}{C_{\max}}\right) \tag{4.4}$$

Given this capacitance-voltage behavior, the sheet carrier density is estimated to be $5.5\text{x}10^{11}/\text{cm}^2$ using the charge control model, thus a giving series resistance of around 113Ω. The Cmax and Cmin obtained from C-V profiles are 0.02 and 2-pF, respectively. Thus the dynamic cut-off frequency can be estimated to be around 69.7-G Hz.

(4) Shunt resistance: Since the shunt resistance is accounted for by the depletion of the 2-DHG and delta doping layer, it is, therefore, a function of external voltage applied. It varies in accordance

with the bias voltage. The value of shunt resistance can be obtained from probe frequency dependent C-V characteristics.

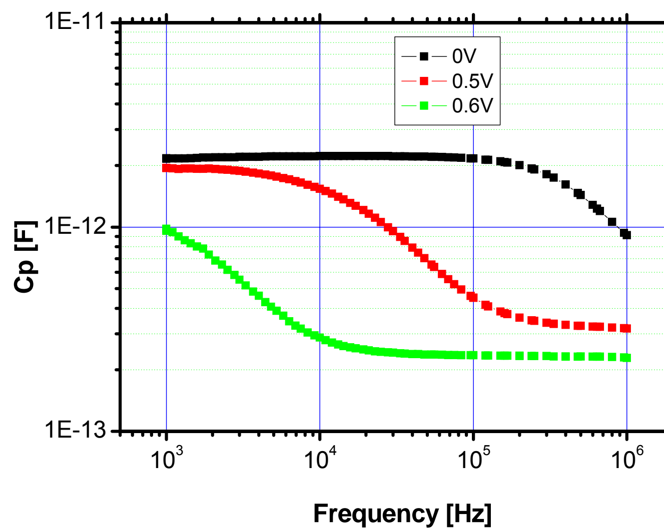

Figure 4.13 The probe frequency response of the capacitance for high doped W2G2 device.

Figure 4.13 plots the probe frequency response of the device capacitance. The three C-f curves in the figure represent the capacitance behavior subject to different external voltage 0, 0.5, and 0.6 V respectively, as the probe frequency sweep from 1 kHz to 1 MHz. All curves shows distinctive cut-off behavior. It suggests the carrier concentration underneath the contacts varies with the applied bias. The density of 2-DHG varies in accordance with the external bias, the larger the bias, the less density of the 2-DHG. The R_{sh} derived from this figure is $1.1\text{x}10^5$ Ω at zero bias.

4.6 Conclusions

We have fabricated an MSM-2DHG heterostructure varactor capable of monolithic integration with III-V technology. The device demonstrates an excellent C_{max}/C_{min} ratio of up to 113 and

extremely high sensitivity of up to 35, one of the best reported so far, making it a good candidate for use in high frequency multiplier design. Alternately, optical intensity modulated sensitivity allows for the potential of applications in optoelectronic mixing. We have proposed a model for the observed device behavior accounting for the source of capacitance, including the contributions from δ doping layer, 2D gas and background charge. The same principles can be applied to the design of a 2DEG device.

CHAPTER 5: CARRIER TRANSPORT IN TWO-DIMENSIONAL-GAS

As we demonstrated previously in Chapter 2, the experimental results of 2-DEG based Schottky heterostructure MSM photodetectors have shown speed of response faster than what is allowed by the transit time of the optically generated carriers. The static behavior simulations, including two dimensional potential and electrical field distributions were performed by commercial software ISE-TCAD, which have suggested that the 2-DEG existing along the interface of the heterostructure created the vertical field in the absorption region due to its screening effects. Above results indicate that the photogenerated carriers' transport is accomplished by two processes in sequence, first is the carrier transport in the absorption region following the vertical field and arriving in the 2-D gas, which is driven by drift and diffusion. The process is followed by the carrier transport along the 2-D gas, and eventually being collected by the external electrodes thus creating the photocurrent.

In Chapter 2 and Chapter 3, the transport in absorption region was simulated using Ramo's theorem. The time responses have proved that the vertical field facilitates the carrier transport in the absorption region. Further analysis is required to study the carrier transport in the 2-D gas. As we discussed before, Ramo's theorem is valid for dynamic behavior description in the regime dominant by drift and diffusion, however, as the dimension goes below 100-Å, such as the case in the 2-D gas, a more accurate method is attempted to achieve a more precise and comprehensive description. Thus a more complicated method, Ensemble-Monte-Carlo (EMC), was employed to study the carrier transport in the 2-D gas.

In this chapter, we will describe the application of Monte Carlo simulation method toward the dynamics of electron transport in 2-DEG in detail. Assumptions of the method will be addressed, and the formulations, procedures and implementations will be described. Lastly, the results will be presented followed by a discussion of application of the results to our physical model of the device,

eventually leading us to a full understanding of the device dynamic behavior.

5.1 Introduction

This chapter addresses the photogenerated carrier transport in two-dimensional gas systems. By two-dimensional system, we mean that the electrons or holes subject to the quantized energy levels in one direction but free to move in the other two spatial dimensions. The quantized energy levels are mostly created by dramatically varying electrostatic potentials in space and the continuity boundary conditions allow the existence of only discrete energy levels along that direction. These systems are not exactly two-dimensional due to the finite spatial extension of the wave functions in the third dimension. Physically, in semiconductor, the 2-D system is usually formed by heterostructure with large energy band offsets, which is able to generate enough potential variations in space, thus confine the movement of carriers to the vicinity of heterojunction, and allow for motion of the electron in a 2-D plane only. A typical AlGaAs/GaAs heterostructure with 2DEG is drawn in Figure 5.1.

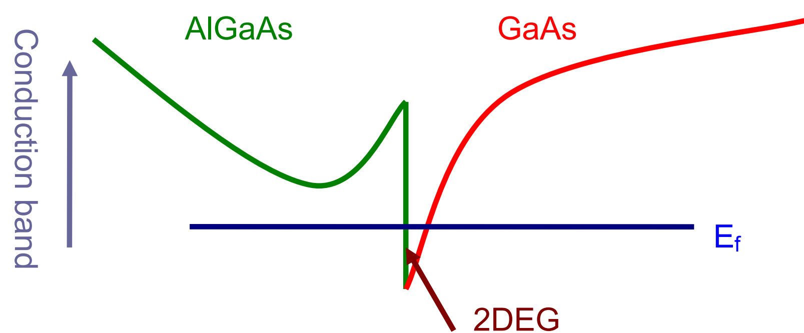

Figure 5.1 A typical conduction band diagram of AlGaAs/GaAs heterostructure with 2DEG at the interface.

Here, ΔE_c is conduction band offset, which combined with band bending in the GaAs side forms a

triangular potential well, hence confines the 2-DEG in the quantum well. The energy levels take the form:

$$E = E_z + \frac{\hbar^2}{2m^*}(k_x{}^2 + k_y{}^2) \quad (5.1)$$

where, E_z is the electronic quantum levels arising from confinement of potential well in z direction, and k_x and k_y are the wave-vector components for motion parallel to the heterointerface.

5.2 Photogenerated carrier transport in 2-D gas

In this section, a more precise calculation of electron transport properties for $Al_xGa_{1-x}As/GaAs$ single-well heterostructures will be studied by an EMC method. The electronic states of the quantum well are calculated self-consistently by incorporating the lowest five subbands. The subband energies and envelope functions in each subband are obtained numerically.

5.2.1 Electronic States

To obtain an accurate description of carrier transport in the 2-D gas system, it is essential to find the electronic states, the quantized subband energy levels and the corresponding wave functions indicating the electron density distributions, in the potential well by means of quantum mechanical calculations. In the triangular-well approximation, which is adopted in our treatment, the quantized energy levels are proportional to the inverse cubic root of the effective mass. We will account for size quantization effects in the Γ valley only, since the effective mass in the subsidiary valleys are larger than in the Γ valley, hence size quantization effects are small in the L or X valleys. Those valleys are also well above first and second quantized subband in Γ valley and may be ignored. A uniform effective mass of 0.067 m_0 and relative dielectric constant of 12.9 are used in both GaAs and AlGaAs layers. The uniform dielectric constant neglects the image force in effective potential. More

assumptions in the calculations include abrupt interfaces, and a ΔEc of 0.3-eV.

A routine as follows was performed by self-consistent numerical solution of the Poisson's equation and Schrődinger's equation [117]. The wave function parallel to the heterointerface is assumed to be a plane wave in *x-y* plane. The envelop function is perpendicular to the *x-y* plane, that is in *z* direction. The wave function for the *i*-th subband thus satisfies the Schrődinger's equation according to:

$$-\frac{\hbar^2}{2m^*}\frac{d^2F_i(z)}{dz^2}+V(z)F_i(z)=E_iF_i(z) \qquad (5.2)$$

where, $F_i(z)$ is the wave function for the *i*-th subband, $V(z)$ is the effective potential, which is given by:

$$V(z)=-e\varphi_e(z)+V_h(z)+V_{xc}(z) \qquad (5.3)$$

where, $\varphi_e(z)$ is the electrostatic potential given by the solution of the Poisson's equation, $V_h(z)$ is the step function describing the interface barrier, and $V_{xc}(z)$ is the local exchange correlation potential.

Poisson's equation is given by:

$$\frac{d^2\varphi_e(z)}{dz^2}=\frac{q}{\varepsilon_0\varepsilon}\left(\sum_{i=1}^{M}N_i\left|F_i(z)\right|^2+N_a(z)-N_d(z)\right) \qquad (5.4)$$

where, M is the number of occupied subbands, $N_a(z)$ and $N_d(z)$ are the position-dependent acceptor and donor concentrations, N_i represents the carrier concentration in subband i and is given in equilibrium by

$$N_i=\frac{m^*}{\pi\hbar^2}\int\frac{1}{1+\exp((E-E_f)/k_BT)}dE \qquad (5.5)$$

where E_f is Fermi Energy. The Fermi integrals are solved numerically [118, 119] without using a Boltzmann approximation. This is necessary because the two-dimensional electron gas is highly degenerat for all cases considered.

The carrier concentration $n(z)$ in the quantum well is related to the wave function by summing up

all subbands occupied for potential evaluation in the Poisson's equation as,

$$n(z) = \sum_{i=1}^{M} F_i(z) F_i^*(z) N_i \tag{5.6}$$

The Schrödinger's equation can be solved using Numerov method [120], which is a two-step, fifth order predictor-corrector method for a second-order ordinary differential equation independent of the first derivative. This algorithm is efficient in terms of obtaining both the eigenvalues and eigenfunctions accurately within brief computational times. It starts with a triangular well, and finds the energy states at room temperature, *T=300K*, and wave functions for each state. We take the first five subbands, and the charge distribution can be calculated as formula (5.5). The self-consistent potential was obtained given the boundary conditions of the potential value and electric field value at the interface. We define the bottom of the conduction band as reference level, where the potential V=0. Given the sheet density of carriers, we can always find the electrical field at the interface from Gauss's law.

This calculation converges after several iterations. Table 5.1 shows the obtained energy eigenvalues for the five lowest subbands, and carrier populations in each subband. The reference energy level is the bottom of the conduction band at the heterointerface, zero point as shown in Figure 5.2. We can see that the first three subbands are populated with 94% of the carriers at room temperature.

Table 5.1 Binding energies and carrier population in each subband.

i-th subband	E_m (eV)	Population (%)
1	0.0555	69.57
2	0.0976	16.86
3	0.1199	7.38
4	0.1369	3.88
5	0.1504	2.32

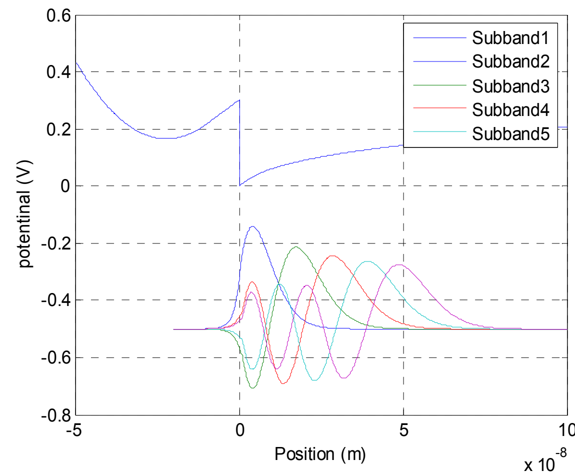

Figure 5.2 Self-consistent effective potential (top), and the corresponding wave functions for the lowest five subbands at 300K respectively (bottom).

It can be seen in Figure 5.2 (bottom) that the carrier density at 300-K extends into the AlGaAs layer. We expect the extension would be much less at lower temperature. From the envelop function we also observe that in the 2-D gas, the region close to the junction, most of the carriers populated in the first subband; carriers in the higher subbands are pushed away from the junction. Hence, the carriers in first subband are most relevant to the transport properties.

5.2.2 Electron-Electron Scattering with EMC simulation

5.2.2.1 Introduction of Monte Carlo technique

Monte Carlo (MC) techniques have been described for application in charge transport in semiconductors by Jacoboni and Reggiani [69]. Basically, this technique simulates the motion of one or more carriers inside the material subject to different scattering mechanisms describing the microscopic process of transport. It consists of two subsequent processes, (1) carrier free flight under the external force of electric and magnetic fields, (2) selecting the scattering events stochastically.

Without exception, Monte Carlo method is based on the generation of a sequence of random numbers between 0 and 1 with given distribution probabilities. For applications in semiconductor transport, several random numbers are generated to determine relevant qualities, such as, duration of free flight, scattering mechanism, final state wave vector after scattering. Figure 5.3 shows a flowchart of a typical Monte Carlo program suited for semiconductor device simulation.

As the procedure is iterated, a steady state will eventually be reached, where the probability of transitions into the state is proportional to the occupancy of that state, and the distribution function evolves with the ensemble is known at every instant of time.

It is sufficient in general to simulate the motion of a single carrier for a steady-state, homogeneous phenomenon. That is single Monte Carlo method. To investigate a non-stationary process, it is necessary to simulate a large number of carriers and follow their dynamics in order to obtain the desired information. This is the so called Ensemble Monte Carlo method, which we employed.

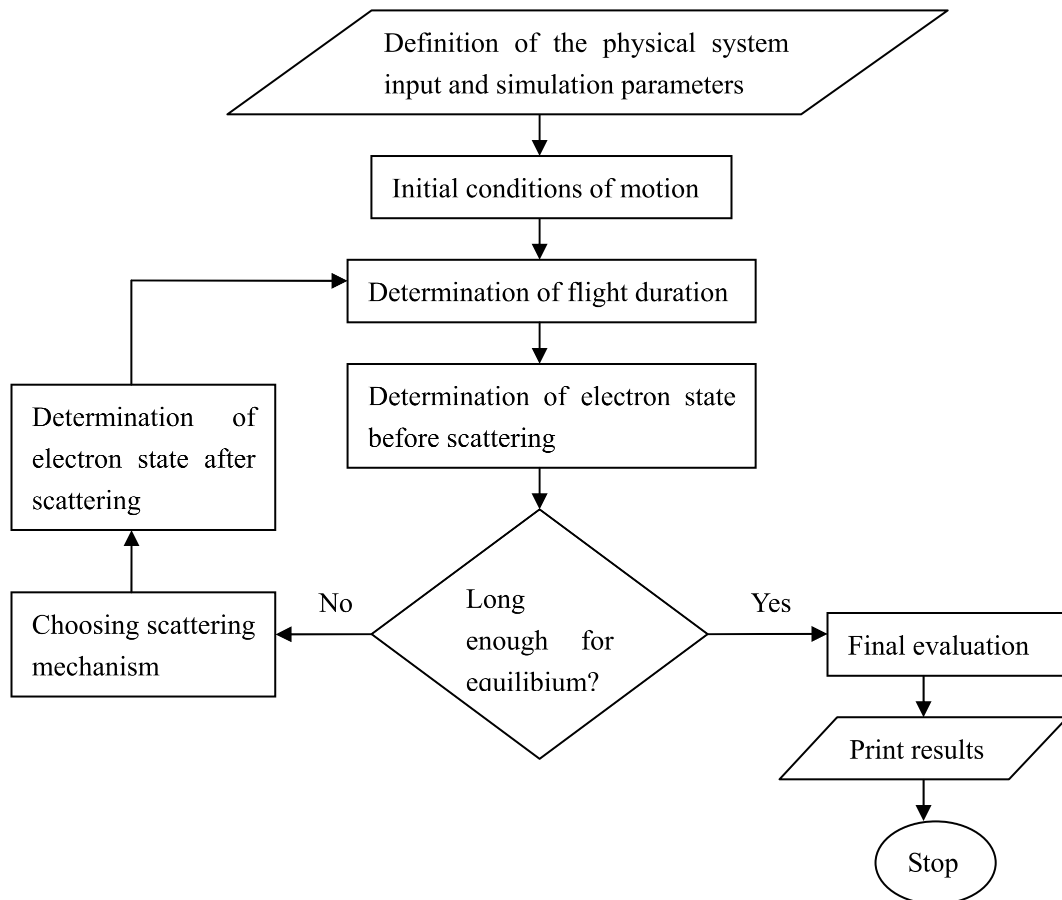

Figure 5.3 A simple flowchart of a Monte Carlo simulation program.

5.2.2.2 Scattering rate and form factor

Here we developed code to evaluate the scattering rate using EMC method and apply it to the 2-DEG system, and are particularly interested in a time scale that only the electron-electron scattering occurs. In the 2-DEG system, the electron-electron scattering rate is much larger than that of electron-phonon scattering [121], which is the dominant mechanism of energy dissipation out of the GaAs channel at room temperature. The electron-electron scattering rate in bulk material has been previously calculated using the Born approximation [122] [123], which turned out to overestimate the scattering rate.

We start by considering the scattering rate between an electron in the well with wave vector k in

subband *i* and a second electron with wave vector k_0 in the subband *j*. The final states of these two electrons are k_0 and *m* for the first electron and k_0' and *n* for the second electron. The total scattering rate is given by [124]:

$$\Gamma_{im}(k) = \frac{4\pi e^4 m^*}{A\hbar^3 k^3} \sum_{k_0, j, n} f_j(k_0) \int_0^{2\pi} \frac{\left|F_{ijmn}(q)\right|^2}{(q+q_{s0})^2} d\theta \quad (5.7)$$

where, q_{s0} is the inverse screening length in two dimensions, $f_i(k_0)$ is the distribution function for electrons, $F_{ijmn}(q)$ is the form factor, given by:

$$F_{ijmn}(q) = \int_{-\infty}^{\infty} dz \int_{-\infty}^{\infty} F_i(z) F_j(z') F^*{}_m(z) F^*{}_n(z') \exp(-q|z-z'|) dz' \quad (5.8)$$

where, $F_i(z)$ is the wave function at the *i*-th subband. The total scattering rate depends on the square of the form factor. The form factor is important, which describe the coupling strength among subband carriers. In another word, the stronger the coupling between subbands suggests the higher transition rates between them.

We calculated several form factors as a function of wave vector, as shown in Figure 5.4, for the triangular quantum well with the electronic states we calculated above. The indices *ijmm* label the initial, *i/j*, and final subband states, *m/n*. Figure 5.4 (a)(b)(c)(d) plot the form factor of initial carriers in the first, second, third and fourth subband respectively.

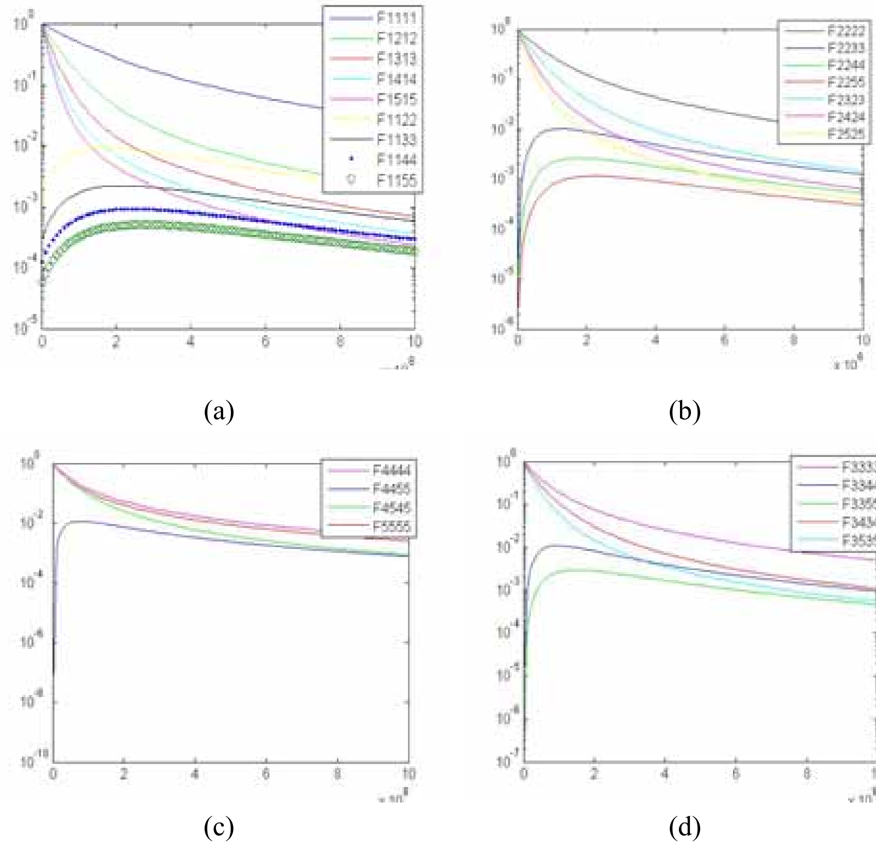

Figure 5.4 Electron-electron scattering form factors as a function of wave vector for a triangular well. X axis is the wave vector q, Y axis is the form factor. The indices *ijmm* label the initial, *i/j*, and final subband states, *m/n*.

We observe that, F_{iiii}, where the initial and final subbands for both electrons are the same, exhibits the highest form factor values in any subband above all other transitions. It means electron-electron scattering favors intrasubband over intersubband transitions. We also observe that the form factor for carriers in the same subband peaks at small wave vector, $q=0$, which indicates the small-angle scattering is favored in the intrasubband transitions; not necessarily true for intersubband transition though. The form factors associated with intersubband transitions is much lower in magnitude and vanishes at $q=0$. Certain combinations of initial and final subband states give rise to extremely small form factors. For intersubband transitions, the dominant transitions, corresponding to the form factor F1221, F1331, F1441, are exchange transitions where the two scattering carriers

exchange their subbands.

5.2.2.3 Electron-electron scattering

For the quasi-two-dimensional quantum well systems, we incorporate both intra- and intersubband scattering. And only two-dimensional transport has been considered, thus the spatial extension along the direction perpendicular to the 2-D plane is not considered. Our treatment of the 2-DEG involved a high concentration of electrons, where degeneracy [125] is expected to play an important role in evaluating the scattering rate, particularly in nonequilibrium cases. A rejection technique accounting for the Pauli Exclusion Principle in the EMC technique is adopted, so that the degeneration of carriers can be incorporated. Once the final state is selected, during the transient phase, a random number between 0 and 1 can be used to accept or reject the transition. Screening was accounted for by a single wave-vector-independent constant.

The electron-electron scattering is simulated with EMC technique using a modified self-scattering technique [126] for the bulk. We use the full multisubband scattering rate formulated in equation (5.7), choosing a maximizing function that is integrable, calculate the total scattering rate based on the new function. The actually value of the function can be evaluated when the final state is chosen through the rejection method. This technique is illustrated in Figure 5.5.

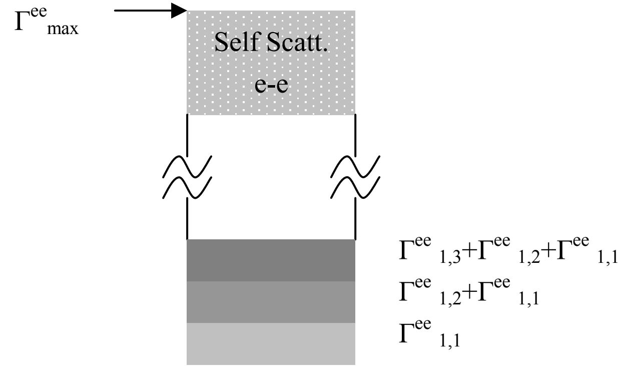

Figure 5.5 Histogram of e-e scattering rate with self-scattering technique.

We note from Figure 5.4 that, for the intrasubband scattering rate, the integrand is sharply peaked at $q=0$. On the other hand, the form factor is always less than unity, hence the maximum value of the integrand of Formula (5.7) is always less than $1/q_0^2$. Thus the maximum scattering rate is given by:

$$\Gamma_{\max,ii} = \frac{4\pi^2 q^4 m^* N_s}{\hbar^3 k^2 q_0^2} \qquad (5.9)$$

where, N_s is the total sheet density in the quantum well. This scattering rate is used to generate the free flight time during the simulation. Same principle applies to the intersubband scattering, thus

$$\Gamma_{\max,im} = \Gamma_{\max,ii} F^2{}_{\max} M \qquad (5.10)$$

where, M is the total number of subbands, and F_{max} is the maximum value of the form factor calculated above.

We simulate the transport process of photogenerated electrons reaching 2-DEG using the Ensemble Monte Carlo method, which is initiated by starting with 2-DEG in equilibrium at room temperature with average energy of a kT, the average thermal energy for 2-D system. Then we introduced an ensemble of carriers, representing the photogenerated carriers injected to the 2-DEG. The energy of the carrier ensemble assumes Gaussian distribution and averages at 150-meV above the bottom of conduction band in 2-DEG. The average energy value is particularly selected, close to the

fifth subband potential energy according to the previously calculated first several discrete energy levels. Here only electron-electron scattering is considered since its rate is much larger than that of the electron-phonon [121] scattering. The 2DEG density was assumed to be $5x10^{12}$ cm^{-2}. The first three subbands in 2-DEG were included, since as we addressed before, the first three subbands populated 94% of the total carriers.

In the beginning of the scattering, an electron is chosen at random from the ensemble, and the scattering angle is chosen at random according to the flat distribution associated with the maximizing function, equation (5.5). Using another random number between zero and the maximum value of $1/q_0^2$, the actual value of the integrand is compared to that of the random number; scattering is rejected if the integrand is less than this number. In this case, the electron and its scattering counterpart are then allowed to continue their free flight. If it is less than the integrand value, then the scattering is accepted; the momentum and energy change accordingly.

The scattering event is calculated for each electron for each time step, and the time step is chosen such that there is enough number of scattering event occurring in each step. After each step the electron energy distribution rearranges itself, and eventually reaches a steady state.

Simulation results are shown in Figure 5.6, which is the time evolution of electron energy distribution. Each curve represents an energy distribution function at some time, and the interval between the curves is 4.5-fs. We observe the evolution of the nonequilibrium portion of the carriers, indicated by the solid oval in Figure 5.6; the peaks in it are the extra electrons with energies above average. We find out these high energy electrons reach a quasi-equilibrium with 2-DEG system in around 30-fs. The time spent by non-equilibirum carriers reaching quasi thermal equilibrium, namely, carriers following the distribution function again, is the thermalization time, or the energy relaxation

time. This femtosecond time scale is consistent with the experimental results obtained by Knox et. al. [127] on carrier thermalization in a dense Fermi sea. As we mentioned above, in this simulation, the injected carrier ensemble carried an average energy close to the fifth subband energy, which is the upper limit of the carriers' energy. Hence the simulated energy relaxation time in the 2-DEG is the upper limit as well.

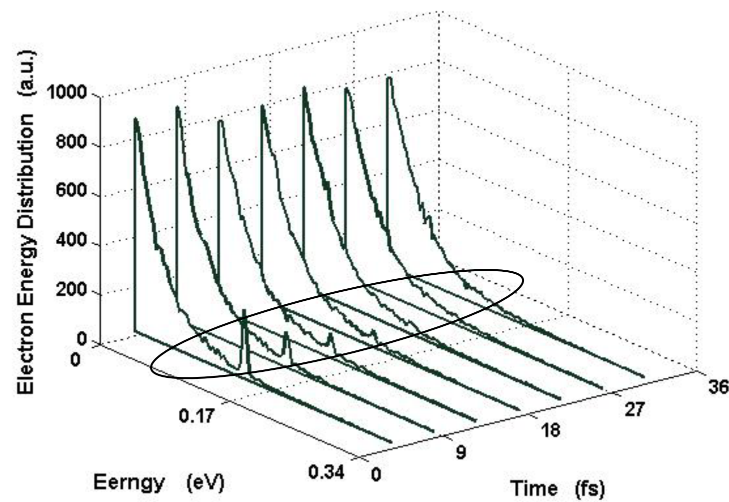

Figure 5.6 Time evolution of the energy distribution in 2DEG when perturbed by extra electrons with energies above average.

During the thermalization time, 2DEG relaxes to an elevated quasi-Fermi level, which means electrons anywhere in the 2DEG could be affected by energy variations in the 2DEG in this time scale; the quasi-Fermi level falls when new equilibrium is established as soon as the excess electrons in 2DEG are swept out of the device and collected by the external creating current. This is a continuous process that carriers are swept to the contacts as long as the quasi-Fermi level in the 2-DEG is above the system Fermi level. It can be interpreted that the electrons of the 2-DEG under anode are affected

by the energy variations of any other electrons in the 2-DEG in a few tens of femtosecond by sensing the elevated quasi-Fermi level. In another words, energy of electrons is distributed through the 2-DEG within a much smaller time than the real electrons transport by drift and diffusion. This result is intuitively reasonable since electron-electron scattering is an inelastic dynamic scattering process, which is the most efficient channel of energy swap in two-dimensional electron system.

It should be noted that, contrary to the channel of a High Electron Mobility Transistor (HEMT), this 2DEG is a reservoir of carriers sandwiched between two blocking Schottky contacts and maintained in quasi equilibrium since only a small amount of thermionic emission current flows. Transport of electrons in the 2-DEG hence is not by drift; rather the cloud of charge redistributes its energy in response to perturbation caused by the arrival of optically generated electrons. In essence, it is the energy that transport along the 2-DEG, in a much faster process than electron transport by drift, that enables the 2-DEG to effectively server as an extended contact for collection of carriers. This argument is also valid when electrons are injected with less energy, so far as their energy is above random fluctuation levels, since we took the upper limit of the average energy for the injected carriers as discussed previously.

The inelastic intersubband and intrasubband transitions due to electron-electron scattering allow energies to be transferred between subbands, so that a uniform energy is reached in the 2-D system efficiently. However, the 2-D system as a whole does not dissipate energy out of the system due to the energy conservation during the electron-electron scattering event. That is the reason we claim the 2-D system being in a quasi-equilibrium state; that the 2-D system itself has reached thermal equilibrium does not guarantee the 2-D system reach equilibrium with the device system.

This simulation result suggests the 2-D gas is able to work as an extended contact to collect

carriers.

5.3 Discussion

Physically, total time response of the doped device thus consists of vertical drift of electrons in the thin absorption region, followed by the fast energy relaxation based transport in the 2-D gas. Given the electron thermalization time at the femto-second level, we consider that the 2DEG system relaxes to thermal equilibrium in such a small time that the transport time in 2-DEG becomes negligible compared to the transit time. In contrast, for the undoped device, the transport of optically generated carriers follows the horizontal electric field line and is completely controlled by drift.

Above simulation is based on 2-DEG system, nevertheless, it is expected that relaxation processes in the valence band will be substantially faster than in the conduction band due to the higher average density of states in the valence band [128]. Therefore, we expect the 2-DHG has the same effect.

5.3.1 2-D versus 3-D gas system

Here we will discuss the effectiveness of the 2-D gas versus 3-D gas in terms of majority carrier collection.

Coulomb potential: The coulomb potential is obtained as we study the response of a system to a weak, static potential that is slowly varying in space by solving Poisson's equation, which is written in 3D as,

$$\nabla^2\varphi - Q_s{}^2\varphi = -4\pi\rho e_{ext} / \varepsilon \qquad (5.11)$$

The 2-D counterpart of the above is [129]:

$$\nabla(\varepsilon\nabla\varphi) - 2\overline{\varepsilon}\overline{q}_s\overline{\varphi}(\vec{r})\delta(z) = -4\pi\rho_{ext} \qquad (5.12)$$

where, ε is the dielectric constant, q_s and Q_s are the screening parameters with dimension of reciprocal length for 2-D and 3-D respectively. The symbols with bars, appearing in 2-D Poisson's equation,

represent the corresponding parameters averaged over the z direction, which is perpendicular to the 2-D plane. Solutions of these equations[129] give the Coulomb potential for 3-D:

$$\varphi(\vec{R}) = (Z_e / \varepsilon\vec{R}) \exp(-Q_s \vec{R}) \qquad (5.13)$$

for 2-D, the asymptotic form of the average potential is

$$\varphi(\vec{r}) \approx \frac{Z_e(1 + q_s z_0)}{\bar{\varepsilon} \bar{q}_s^{\,2} \vec{r}^{\,3}} \qquad (5.14)$$

This inverse-cube dependence of the potential on distance in 2-D is much slower than the exponential decay found in the 3-D case. This means the potential variations subject to external charge perturbations are much slower in 2-D than in 3-D. In this sense, 2-D system is more like metal than 3-D ones, and able to collect the carriers more efficiently.

Plasma: As the carrier density increase in the semiconductor, plasma will form and allow the gas to screen the external electric field. The mechanism of plasma conduction is completely different from what we have discussed previously; it is a collective behavior of carriers due to the high carrier density, like wave propagation rather than single particle conduction in the solid state materials. A large number of previous theoretical [130] and experimental study show that it is easier to form a plasma in the 2-D than in the 3-D in terms of threshold density to create plasma.

5.3.2 Schottky contacts

Another issue that brings our attention is, our proposal is based on the two blocking contacts forming at both ends of the 2-D system, which allow the 2-D system to be a closed one, hence keep the process of energy relaxation within the 2-D system only. In contrast, in an open system, like Ohmic contact, it allows for the free exchange of particles between 2-D gas and external circuit at a small effort, basically, the effort to overcome the serious resistance.

5.4 Conclusion

In this chapter, we examined the dynamic behavior of the device in which transit of optically generated carriers is not to the contacts directly, rather, electrons drift to the 2-DEG and subsequently transport along the 2-DEG via a much faster process of energy relaxation, hence the drift limitations of transport are circumvented in this stage, which speed up the time response of the device.

The electronic states of the 2-D system were fully exploited with quantum mechanical treatment by numerical solution of Schrodinger's equation of Poisson's equation. We studied the process of energy relaxation in 2-D system using EMC method by incorporating electron-electron scattering. The details of the EMC method applied to semiconductor charge transport was presented.

The simulation result showed a sub-picosecond energy relaxation time was achieved in the 2-D system toward thermal equilibrium. We propose that the photogenerated carries drifting to the 2-D gas are no longer transported by drift in the 2-D gas, rather, by the much faster process of energy relaxation of the electron gas, which is negligible compared to the transit in the absorption region in terms of time consumption. It indicates that the response time of the device is only limited by the transit time in the absorption region. This has important ramifications in device design.

The extremely fast electron energy thermalization, benefited by the two blocking Schottky contact, circumvents the drift velocity limitation of electron transport in semiconductor devices, and could be applied in a wide range of high speed device design.

CHAPTER 6: FUTURE WORK AND CONCLUSIONS

In this chapter, conclusions about the dissertation will be drawn and the author's contributions will be presented. Further work in the future, including a 2-DEG/2-DHG based photodetector design; edge-coupled waveguide design, theoretical work regarding the 2-D plasma; InP and LT-GaAs materials, will be discussed.

6.1 Future Work

Several aspects of research, such as in-depth theoretical work, wide ranges of applications, further material explorations, can be extended from the present work in the future as both breadth and depth are concerned. These issues include collective behavior in low dimensional structures, waveguide design, employment of InP and LT-GaAs materials.

6.1.1 2DEG/2DHG Device Design

In previous chapters we reported design, fabrication and analysis of high-speed heterostructure MSM photodetector device with built-in 2-DEG and 2-DHG feature respectively. Speed characterization of 2-DEG device showed that the vertical field in the intrinsic absorption region was able to enhance the transit time without sacrificing the optical coupling. However, the vertical field degrades the slow carrier as it facilitates the fast carrier transit. The time response of the 2-DEG device suffers from the long tail due to the slow carrier transit. The 2-DHG device was fabricated to study the slow carrier dynamics. The heavy hole effective mess and small valence band offset available in current material systems prevent the strict confinement, and the speed of the 2-DHG device is slow. Nevertheless, we confirmed that the 2-DHG helps collect the slow holes and overcome the long tail issues in the time response. It provides a solution to achieve high-speed detection by slow carrier collection.

Therefore, we propose a new design combining the advantage of both 2-DEG and 2-DHG devices. We design a heterostructure with both 2-DEG and 2-DHG in the absorption region, one on the top, and one at the bottom. In this manner, the 2-DEG gas plane and 2-DHG gas plan working together are able to create a built-in vertical field along the growth direction in the intrinsic absorption region; on the other hand, they operate as extended contacts collecting the respective majority carriers. The basic concept results in transforming the lateral HMSM to a vertical structure. As a vertically illuminated photodetector, the RCE structure would help enhance the quantum efficiency. The new design aims at high-speed detection without scarifying sensitivity.

In the design of a high-speed MSM photodetector, the main emphasis is to confine a dense 2-D gas and maintain a vertical field. The 2-DEG has been widely investigated in HEMT structures. $Al_{0.3}Ga_{0.7}As/GaAs$ has conduction band discontinuity, ΔE_c, of 0.3-eV, which is enough to generate quantized energy band and confine the electron gas within a 100-Å distance from the heterojunction. However, as has been demonstrated in the 2-DHG devices, the valence band offset provided by $Al_{0.5}Ga_{0.5}As/GaAs$ heterojunction is not high enough to confine the hole gas considering its large effective mass. Therefore, strained InGaAs material would be a good candidate to form the channel for hole gas. Another advantage of the strained InGaAs material is it can be easily adapted to InP material system for long wavelength detector albeit with different In- component.

The best way to form a built-in vertical field is to make the external electrodes contact the 2-D gas. To achieve that, the regrowth technique can be used in growth of the structure. The semiconductor regrowth interface can be chosen at the bottom of the intrinsic absorption region. During the device fabrication, the wafer is firstly etched down till the regrowth interface where one of the metal electrodes is to be deposited; then regrow with heavily doped p+ material. In this manner, the p+

electrode is able to extend vertically to the bottom of the absorption region makes direct contact with 2-D gas, thus it is easy to form a vertical field in the absorption region.

6.1.1.1 Epilayer design

In this design, we will still employ the cavity enhanced vertical illuminated (VPD) design. The layered structures, from the substrate along the growth direction, are semi-insulating GaAs substrate, AlGaAs pairs of DBR, strained InGaAs channel for 2DHG confinement, intrinsic absorption region GaAs, barrier enhancement layer AlGaAs, where an n-type and a p-type atomic planar doping layer are grown in the barrier enhancement layer and first DBR layer respective for purpose of modulation doping. The major considerations of the epilayer structure are i. e. the composition of the material, the thickness of each layer. The following section will discuss the design of each layer in a detail. The schematics of the device, shown in Figure 6.1, present a brief conceptual description of the device to be designed. The key points that has not been addressed are the 2DEG-2DHG configuration and the direct contact of the 3D electrode to 2D hole gas.

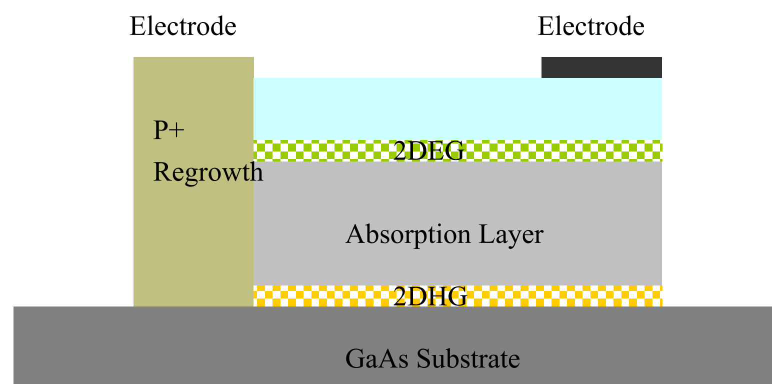

Figure 6.1 A simple schematic diagram of 2-DEG/2-DHG device to be designed.

For this new design, a most important issue we need to take into consideration is the parallel

planes of electron and hole gas between the 2DEG and 2DHG, as we see in the above schematics. This will cause increase of capacitance, which has to be accounted in device design.

Barrier enhancement layer: In Chapter 2, we discussed the $Al_xGa_{1-x}As$ barrier enhancement layer design for 2-DHG. Here the same principle applies except it applies to 2DEG.

This top layer plays several roles in the device performance. Firstly, it enhances the Schottky barrier height thus is able to reduce the dark current. Secondly, it combines with the active GaAs absorption region, forms a resonant cavity to increase the absorption. Lastly, the δ doping layer inside provides the carrier source for the 2-D gas at the heterointerface.

In choosing the Al content of $Al_xGa_{1-x}As$, one needs to consider:

(1) Al should be high enough to be transparent for light above 830-nm and have low index to support the optical standing wave, considering the reverse relationship between the optical refractive index and Al mole fraction. On the other hand, considering the reflection from the top mirror, namely air, lower Al- contents and higher refractive index makes distinctive contrast to the low refractive index layer thus achieving maximum reflectivity. Figure 6.2 plots optical refractive index and energy bandgap variations versus Al component [131]. The 830-nm wavelength transforms to an energy bandgap of 1.49-eV by an established relationship of $E=1.24/\lambda$, where E in unit of eV, and λ in μm. This point gives rise to an equivalent Al content of 7%, which is the lower limit to differentiate the passive wave confinement region from the active absorption region.

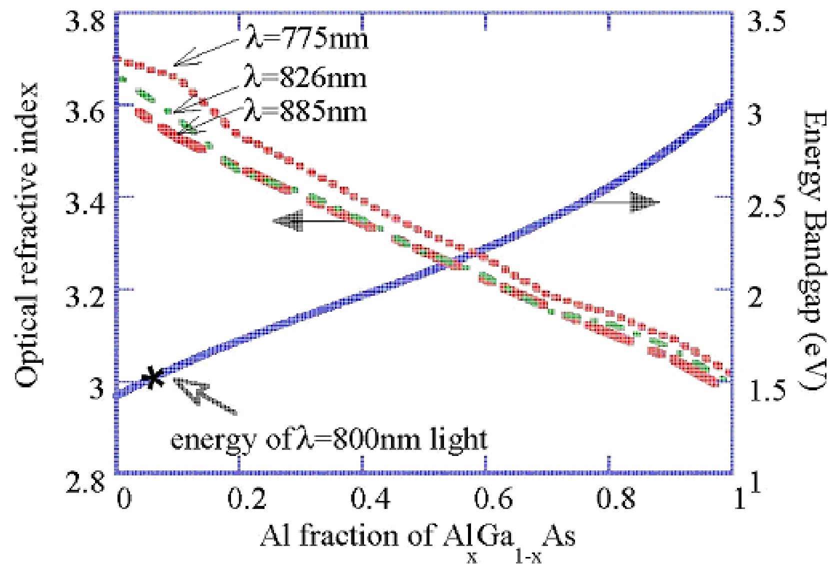

Figure 6.2 The AlGaAs refractive index and energy bandgap for different compositions [131].

(2) Al component directly influences the quality of 2DEG confinement. The increased energy bandgap of $Al_xGa_{1-x}As$, adjusted by Al component, results in a larger conduction/valence band discontinuity, hence the higher barrier height for quantum well, the better 2-D carrier confinement. In this sense, higher Al component is desired.

(3) High Al component in doped AlGaAs creates higher density of DX-center [132], a bistable deep-level center, deteriorates electrical and optical properties of the material due to the coexistence of Al and donor atoms. Such inferior characteristics can be greatly reduced by spatial separation of these atoms. Therefore, the uniform doping is better to be replaced with a δ-doped $Al_xGa_{1-x}As$ for purpose of modulation.

(4) Considering the direct contact with metal, the $Al_xGa_{1-x}As$ should have high enough carrier mobility to make good contact for the metalization, thus the Al content should be kept low. The electron motilities of $Al_xGa_{1-x}As$ do not significantly changed in the compositions of $0<x<0.3$, but the hole motilities drop abruptly as x increases [133]. Hence, to keep the Al contents of $Al_xGa_{1-x}As$ as low

as possible helps to generate lower material resistivity and series contact resistance.

The design of the concentration of δ-doped layer, and thickness of the spacer layer has been discussed in chapter 3, and will not be addressed here any further. From all the above considerations, we choose an Al component of 30% for barrier enhancement layer. The choice of thickness is more related to the resonant-cavity-enhanced (RCE) structure, which will be addressed in next section.

Active region: The material of the active region is the intrinsic undoped GaAs. The major concern for the active region is its thickness. Relevant considerations are: (1) the thickness directly relates to the speed of the device since the transit path of photogenerated carriers is the depth of the absorption region, given the vertical field created by 2-D gas. Large thickness causes longer transit time, and slower speed of the device. (2) The thickness must large enough to allow the maximum absorption of input radiation in the active region, (3) as we mentioned before, in the 2DEG-2DHG design, the thickness of the cavity can not be too thin to allow the intrinsic RC time constant dominating the speed of the device due to the capacitance contributions from electron gas and hole gas.

The active region combining with barrier enhancement layer constitutes a Fabry-Perot resonant cavity for optical confinement. The large difference of the refractive index between air and barrier enhancement layer allows the air to be one of the end mirrors, and quarter wave stacks of DBR is the other end mirror for the cavity. Figure 6.3 is the schematic diagram of RCE photodetector.

In the figure, L1, L2 are the thickness of barrier enhancement layer and absorption layer respectively, R1 and R2 are the reflectivity of the top and bottom mirror, Ψ_1 and Ψ_2 are phase shifts introduced by top and bottom mirrors due to light penetration into the mirrors. The quantum efficiency of the structure can be derived as [42]:

$$\eta = (1 - R_1)(1 - e^{-\alpha L_2}) \times \left\{ \frac{\left(1 + R_2 e^{-\alpha L_2}\right)}{1 - 2\sqrt{R_1 R_2} e^{-\alpha L_2} \cos(2\beta L + \Psi_1 + \Psi_2) + R_1 R_2 e^{-2\alpha L_2}} \right\} \quad (6.1)$$

where, α is the absorption coefficient of the absorption layer, and β is the propagation constants in absorption region. The quantum efficiency reaches a maximum when $2\beta L + \Psi_1 + \Psi_2) = 2n\pi$ according to the formula above.

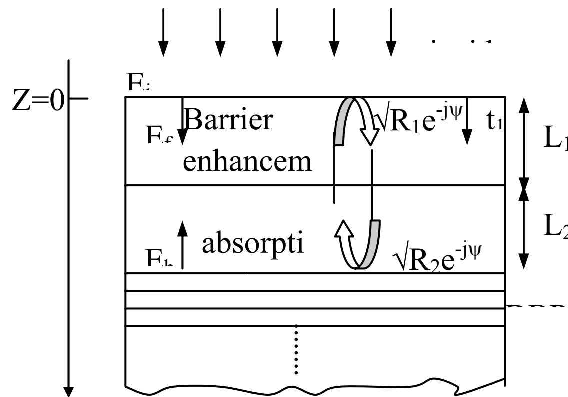

Figure 6.3 Schematic diagram of Resonant Cavity Enhanced structure [63].

As we mentioned in the beginning, the capacitance generated from the overlap the 2DEG and 2DHG may hamper the device performance. Figure 6.4 calculate the frequency dependence over the thickness of the intrinsic region based on transit time and RC time limitations. We assume the area of the active region is A = 10x10 μm^2, and half of the area is covered with metal contact. According to above resonance conditions, the thickness of cavity has to meet the condition that,

$$T = m \frac{\lambda}{2n_{GaAs}} \quad (6.2)$$

where, $m = 1,2,3...$ and n_{GaAs} is the refractive index of the intrinsic GaAs.

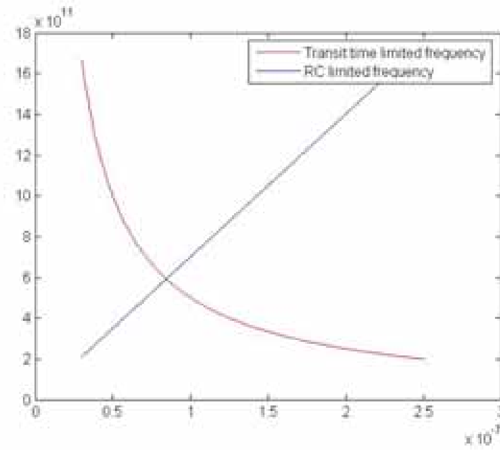

Figure 6.4 The optimization of RC limited and transit time limited frequency response.

This plot indicates that as long as the thickness is greater than 80-nm, the speed of the device will not be limited by the RC time constant. The half-wave thickness for resonance is 118-nm, given the refractive index of GaAs as 3.5. Technically, the device will not be limited by RC time. This calculation is subjected to the previous assumptions about the device area of active region and coverage percentage of the metal electrode.

InGaAs channel: This layer basically provides a channel to confine the 2DHG. The $In_xGa_{1-x}As$ is a versatile material due to its flexibility of engineering in terms of band gap, lattice constant, energy band structure, and etc. It can be adapted to both GaAs and InP substrate given different mole fraction of In. Its energy band engineered by lattice strain lends the material particular features for wide applications. Here we focus our discussion to the properties of $In_xGa_{1-x}As$ on a GaAs substrate.

The strained $In_xGa_{1-x}As$ differs from its bulk version for two reasons: the low thickness of the $In_xGa_{1-x}As$ channel leads to quantum size effects and the deformation of lattice alters band structure and material parameters. The in-plane and off-plane strain tensors are given:

$$\sigma_{//} = (a_0 / a) - 1; \sigma_{\perp} = -2(c_{12} / c_{11})\sigma_{//}; \quad (6.3)$$

$$P = -[(c_{11} + 2c_{12}) / 3](2\sigma_{//} + \sigma_{\perp}); \quad (6.4)$$

where, P is the total strain tensor combining the isotropic and anisotropic components, the composition dependent c_{11} and c_{12} are the elastic stiffness constant of $In_xGa_{1-x}As$

$$c_{11} = 1.223(1-x) + 0.833x\,,\ \ c_{12} = 0.571(1-x) + 0.453x \tag{6.5}$$

a and a_0 are the lattice constant of strained $In_xGa_{1-x}As$ and host material, respectively. Total energy splitting due to strain is obtained using the deformation potential by

$$\Delta E_{X2-X4} = \Phi_u(\sigma_\perp - \sigma_{//}) \tag{6.6}$$

where the subscript X2-X4 represents the 6-fold degenerated X-valleys are split into a 4-fold quadruplet and a 2-fold pair, Φ_u is the deformation potential, its composition dependence is formulated as,

$$\Phi_u = 8.61(1-x) + 4.5x \tag{6.7}$$

The detailed parameters are given in [134], and the electrical properties of strained $In_xGa_{1-x}As$ have been simulated using those parameters.

The increased In- mole fraction lifts the zone-center (Γ valley) degeneracy of the heavy-hole and light-hole bands; it results in a reduction of the in-plane hole effective mass and increase of effective mass in growth direction. As a direct consequence, the 2-D holes in $In_xGa_{1-x}As$ channel layer may reach a better confinement.

In- component respective to the bandgap, valence band offset, and extent of strain are critical in confining the holes to a quantized 2-D. Table 6.1 lists the electrical and optical material parameters for InAs, and GaAs.

Table 6.1 Material parameters for InAs and GaAs.

	InAs	GaAs
Lattice constant (Å)	6.0583	5.65325
Energy bandgap (eV)	0.354	1.424
Dielectric constant (Static/High f)	15.15/12.3	12.9/10.89
Effective electron mass (mo)	0.023	0.063
Effective hole mass (heavy) (mo)	0.41	0.51
Effective hole mass (light) (mo)	0.026	0.082
Mobility of electrons/holes (cm2V-1s-1)	40000/500	8500/400
Infrared refractive index(300 K)	3.51	3.5
Electron affinity (eV)	4.9	4.07

To obtain high valence band discontinuity thus generating a better quantum well for holes, large component of In- is required. In the device, the quantum well for holes is a double heterojunction structure, namely, the $In_xGa_{1-x}As$ is sandwiched by $Al_xGa_{1-x}As$ the one of the DBR stack layers that adjacent to the $In_xGa_{1-x}As$ channel. The schematic energy band diagram is plotted in below Figure 6.5.

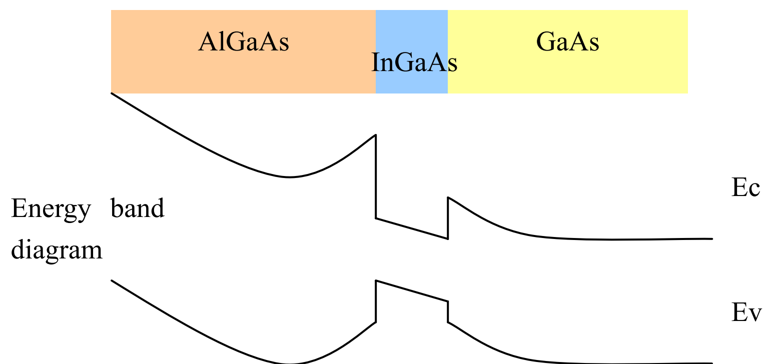

Figure 6.5 Energy band diagraom for AlGaAs/InGaAs/GaAs.

The active region combining with barrier enhancement layer constitutes a Fabry-Perot resonant cavity for optical confinement. The large difference of the refractive index between air and barrier

enhancement layer allows the air to be one of the end mirrors, and quarter wave stacks of DBR is the other end mirror for the cavity. Figure 6.3 is the schematic diagram of RCE photodetector.

A balance between the In- contents and critical thickness is crucial in maintaining the material properties of strain. For any strained material, the lattice mismatch is fully accommodated by strain without high density of dislocations when the material thickness does not exceed a critical value.

Figure 6.6 shows the calculated and measured critical layer thickness of the InGaAs on GaAs as a function of InAs mole grown at 460-℃ [74]. The line on the left is after the theory of Mathews which is based on the single interface relaxation single-kink, mechanical equilibrium. The broken line is based on the same theory with the double interface relaxation, double kink. Critical layer thickness following the energy balance model of People and Bean is also shown. As seen, experiments agree with the Mathews model for large strains and People and Bean model for small strains.

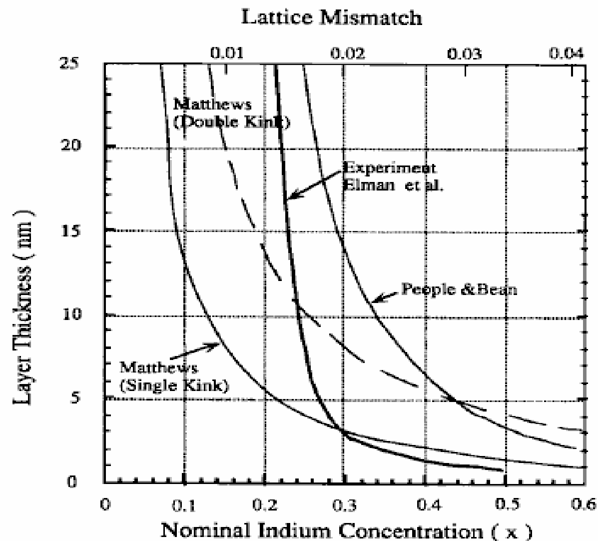

Figure 6.6 The calculated and measured critical thickness of InGaAs as a function of In mole fraction [74].

Given the information above, a conservative estimation for an x=0.2 $In_xGa_{1-x}As$, the thickness better does not exceed 10-nm.

Though the thickness of the $In_xGa_{1-x}As$ is not meant to be large, we still need to take it into consideration for cavity design. The finite thickness and its unique refractive index make it a distinctive layer, which affects the reflectivity of the whole epilayer structure and the effective cavity length.

Quarter wave DBR: The realization of high-reflectivity mirrors typically involves one or more dielectric quarter-wave stacks to achieve a desired reflectivity and bandwidth for selected wavelength. The condition to be satisfied for the DBR material is (1) lattice matched material (2) both must have bandgap greater than the incident photon energy such that ensure they can confine the optical field of interest effectively and do not absorb the incident light. As a consequence, short wavelength might be absorbed to some extent in the mirror. (3) The DBR pair should have the refractive index contrast as large as possible. More detailed discussions about DBR is presented in [135]. Based on above criteria, we choose the AlAs/Al0.3Ga0.7As pairs for its large refractive index contrast.

6.1.1.2 Design for characterization

From the discussion above, the epitaxial layer of new 2-DEG and 2-DHG based high-speed photodetector is grown in sequence as follows. Several characterizations are meant to be performed in order to fully understand the device behavior.

Table 6.2 Layered structure design for 2-DEG/2-DHG based photodetector design.

Layer #	Thickness	Material	Description
12	5 nm	GaAs	n+ $5x10^{18}cm^{3}$ Cap layer
11	56.4 nm	Al.3Ga.7As	Barrier Layer
10	Si Delta	Al.3Ga.7A	Modulation Delta doping, $6*10^{12}/cm^{2}$
9	5 nm	Al.3Ga.7A	Undoped
8	109.4 nm	GaAs	Absorption layer, adjusted by InGaAs layer
7	8 nm	In.2Ga.8As	Strained 2DHG channel
6	5 nm	Al0.3Ga0.7As	Spacer
5	Be Delta	Al0.3Ga0.7As	Modulation Delta doping, $2.5*10^{12}/cm^{2}$
4	57.3 nm	Al0.3Ga0.7As	Compensated thickness of Delta layer
3	71.1 nm (x15)	AlAs	15 wells for Bragg Reflection
2	62.3 nm(x14)	Al0.3Ga0.7As	15 wells for Bragg Reflection
1	200 nm	GaAs	buffer
0	2"	GaAs	Semi-insulating Substrate

Static Measurement: Basic static DC measurement includes Transmission Line Model (TLM), current-voltage (I-V) dark and under light, capacitance-voltage (C-V) dark and under light, current spectra (I-λ). TLM patterns can be used to characterize the bulk material resistivity and contact resistance [136]. From I-V characterization, the quantum efficiency, sensitivity, responsitivity, can be extracted. The C-V information can be used to extract the carrier density information. I-λ is able to characterize the optical properties of RCE cavity and DBR.

Time-response measurement: Basic method to characterize the dynamic response of the device is the electrical sampling. Typically, the bandwidths of the sampling oscilloscope, microwave cable, cascade microwave probe and the bias Tee are around 40-GHz. Taking the bandwidth as a Gaussian-like profile, the impulse response due to the instrument is about 16-ps FWHM. For any device response frequency greater than that, the electro-optic measurement technique has to be employed.

Microwave measurement: Further microwave measurement, basically the s-parameters, obtained by small-signal response of the device is able to verify the lumped equivalent circuit. The parasitic equivalent circuit[137] of a photodetector is shown in Figure 6.7.

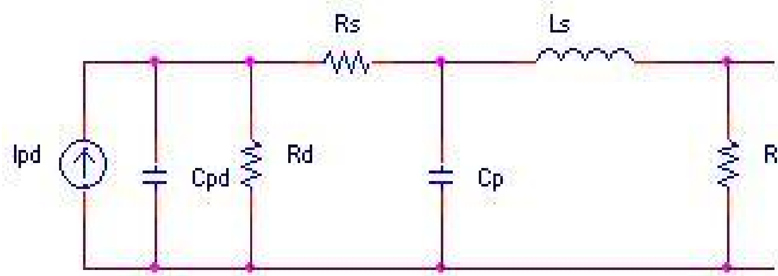

Figure 6.7 Equivalent circuit of semiconductor photodetector.

The Ipd is the intrinsic photocurrent, Cpd is parasitic capacitor, Cp is the pad capacitor, Rs is the series resistor. The microwave properties of the circuit are represented by the S-parameter. S_{11} represents the reflection of the signal from one end of 50-Ω transmission line of the measured waveguide; S_{21} shows the microwave transmission through the waveguide. It can be obtained by a numerical solution of Maxwell's equations at different frequencies. The measured S-parameter by network analyzer thus can be utilized to verify the equivalent circuit[138].

For waveguide structures, small-signal AC measurement can characterize waveguide properties, including the microwave field attenuation factors, microwave index and the waveguide characteristic impedance.

6.1.1.3 Summary

The 2-DEG/2-DHG based vertical field MSM-PD design aims at wide bandwidth and high

efficiency performance. The vertical field attempts to transform the transit path of photogenerated carriers from a lateral one, where the finger separation determines the dynamics, to a vertical one, where the thickness of the absorption region determines its dynamics. In another word, it allows the large finger separation devices reach the same speed of the small ones; important advantages of this design are (1) the speed of the detector can be enhanced by thin active region, rather than by optical lithography defined mask pattern. It is much easier to implement the former one than the latter with current technology; (2) the efficiency can be improved by employing larger finger separations, hence less reflected loss due to the electrode area, without sacrificing the speed performance.

In this chapter, we designed a 2-DEG/2-DHG based high-speed vertical MSM photodetector for vertical illumination. The featured structures are discussed, including RCE, DBR, strained $In_xGa_{1-x}As$, 2DEG-2DHG, and etc. The design guidelines for epitaxial growth layers toward enhanced overall performances are investigated systematically. Finally, the design for characterization is presented.

6.1.2 Edge-coupled traveling-wave Design

For high-saturation power and high-frequency design, the edge-coupled traveling-wave design can be employed when monolithic integration or high responsivity are not the first priority. The advantage of MSM waveguide structure over the p-i-n waveguide lies in the fact that MSM structure inherently has low capacitance per unit length and is easier to achieve a 50-Ω transmission line with velocity-matched property, which suggests the optical signal and microwave signal propagate at the same velocity, as compared to the p-i-n waveguide structures. It is worthwhile to develop a MSM edge-coupled traveling-wave design. The Figure 6.8 shows a schematic MSM traveling-wave photodetector design, which includes the traveling-wave structure and the MSM detector structure.

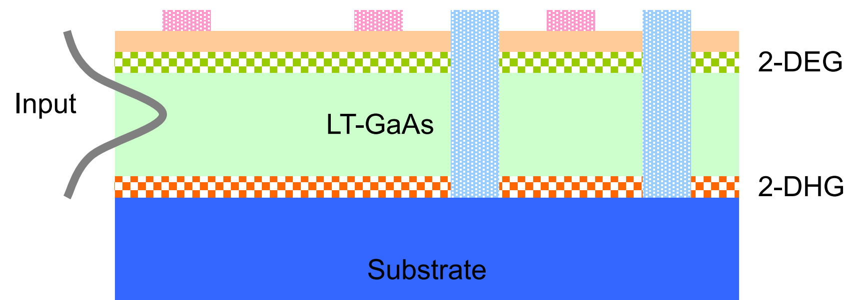

Figure 6.8 Schematic diagram of distributed MSM photodetector.

Edge-coupled design: Our MSM photodetector can be adapted to an edge coupled design, where the electrical wave and optical wave travel in the same direction, which leads to separate optimization of quantum efficiency and frequency bandwidth. It is essential for transit time limited device and high saturation current applications due to the advantage of waveguide structure. In contrast to vertical illuminated devices, the total photocurrent response is collected be the fully distributed photodetectors with optical wave traveling along the transmission line. We have discussed the edge-coupled device in the introduction part, and will not address it in further details.

Traveling-wave design: The traveling-wave photodetector is one type of waveguide structure with edge-coupled input light. From a circuit point of view, waveguide structure is a distributed photocurrent. The main factors influencing the speed of distributed photodetectors are velocity mismatching, impedance mismatching, and microwave loss. For high-frequency applications, the speed of device in a long waveguide structure is always limited by the microwave loss no matter how much effort has been done toward velocity and impedance matching. A traveling wave structure is used only when the devices are short enough and will not be degraded by velocity mismatch, such that the bandwidth is determined by the device response only, rather than the high microwave propagation loss from the transmission line. Therefore, a photodetector is defined as traveling-wave photodetector

only when the optical and electrical waves interact in a coherent distance.

The bandwidth limitation is subject to the device response and circuit response. The former is determined by the intrinsic region response, the latter is determined by circuit response, namely the interaction of optical and electrical waves along the propagation line. With suitable traveling-wave design, the speed of the circuit can be optimized. The essence of traveling-wave design is optimizing the circuit response to overcome the RC-imposed limitation, so that achieving a bandwidth of the circuits higher than the limitation imposed by the device response.

A better traveling wave design requires the velocities of the optical wave matching the electrical wave such that no walk-off issues occur. It also requires matching the microwave impedance of the waveguide to the circuit load, hence minimize the microwave reflection from the load boundaries to avoid RC roll-off frequency, otherwise, it would cause the limitation from RC lump element. A typical structure of traveling-wave design for MSM device is a coplanar waveguide (CPW) structure, which has lower capacitance and dispersion [139].

The main concerns in the traveling-wave circuit design are the length of the device, and the thickness of the intrinsic region. Longer device is able to obtain higher quantum efficiency due to more complete light absorption, but it does create higher microwave loss. From a circuit perspective, increasing the thickness of intrinsic region results in higher impedance, microwave velocity, optical confinement factor and lower microwave loss, however, the quantum efficiency and speed are sacrificed due to the longer transit time. The design of the intrinsic region is also restricted by the geometry of transmission line. These trade-offs among performances have to be considered for device design

6.1.3 Extension of theoretical work

Plasma for Tera-hertz radiation detection: The theoretical work toward two-dimensional gas can be extended from the thesis. In a 2-D gas system, as the electron-electron collisions become dominant and the system does not exchange energy with external systems, the electrons in 2-D gas demonstrated a collective behavior, the so-called 2-D plasma wave. Carriers behave like a two-dimensional electron fluid, i.e., they can be described by hydrodynamic equations. These equations are used to describe the water flow in shallow channels, and the solution provides a solid theoretical basis for detection, mixing, and frequency multiplication of terahertz radiation by using 2-D electron fluid system [140]. Given the dispersion law, the 2-D plasma wave in a submicron length channel, acting as a resonant cavity, can reach the frequencies around TeraHertz. This result has significant consequences for the device performance since it provides a chance for current solid-state devices overcoming the frequency limitations due to the fast speed of plasma.

The plasma wave in 2-D semiconductors can be further explored for many applications, particularly in terahertz sources and detectors, where the gap exists for semiconductor materials between the wavelength of electrical and optical signal. In short-channel device, spontaneous plasma wave may cause an instability, predicated by Dyakonov[140], and it provides a mechanism for the emission of tunable terahertz, or far infrared electromagnetic, radiation. This has been observed by Knap et al [141] from a GaAs based deep submicron gate high-electron-mobility transistor device, though the exact mechanism of such emission remains unclear. 2-D plasma in a HEMT structure can also operate as a detector for terahertz radiation. The resonant voltage detection using plasma resonance in 2-D system has been proposed by Shur and his co-workers [140, 142]. In a GaAs , or GaN based HEMT, the terahertz frequency detection has been demonstrated [143-145]. The tunable

detection can also be achieved by varying the gate bias [146].

However, there are still considerable unsolved issues, both theoretical and experimental ones, regarding the 2-D plasma wave. The problems that have to be addressed include, the justified prerequisites for creating plasma waves, the coupling mechanisms between the plasma waves and the electromagnetic radiations, the boundary conditions [147], i.e, the contact to external circuit, the viscosity in the electron fluid, the transient response [148], the plasma dispersion relations, the effect of velocity saturation and the plasma wave choking, the resonant conditions, and DC/AC signal excitations. Further study of the topic may be developed toward 1-D plasma waves and surface plasma.

Heterodimensional contact: Due to the development of fabrication technology and theoretical progress, quantum devices, i.e. quantum well, quantum wire, has been explored for wide applications. The connection of the quantum device with external circuit or systems gives rise to heterodimensional contacts, which are the contact junctions between regions of different dimensionalities. Heterodimensional technology has several advantages, such as ultra-low power [149], high functionality, ideal scaling, excellent temperature coefficients [150], low output conductance in saturation, low drain-induced-barrier lowering (DIBL). A schematic diagram about heterodimensional contacts are depicted in Figure 6.9. In our newly designed devices, the p+ regrowth region has to make a direct contact with 2-D gas, which is 3-D semiconductor contacting with 2-D semiconductor. In addition, other configurations, i.e. 3D-2D, 3D-1D, 2D-2D are feasible, such as the recessed metal electrode contacting with the 2-DEG or 1-DEG, 2D MESFETs [151]. In some applications, we need to solve the issue of small current transmittance in heterodimensional contact, such as in single electron device (SED). Some applications deliberately reduce the current by heterodimensional contact. For

example, our 2-DHG photodetector measures a current as low as several pico-amps, and low dark current, i.e. picoamps [152], was achieved as well due to the heterodimensional contact.

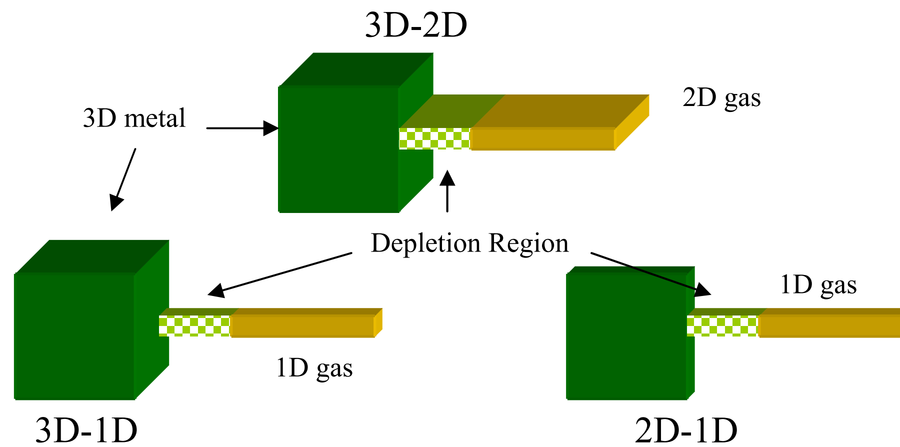

Figure 6.9 Schematic diagram of heterodimensional contact.

The topics regarding heterodimensional contact includes transmission of current transport [53], and boundary conditions for heterodimensional contact [152]. The physics of heterodimensional junction contact ranges from wider depletion region thus lower capacitance and higher breakdown voltage, to small change in the barrier height with temperature; from Schottky barrier enhancement to better carrier confinement.

6.1.4 Material Explorations

At present, the devices we have designed are all based on GaAs material system for short wavelength detection. It is desirable to extend the design to the long wavelength regime for wider applications.

InGaAs/InP material system: For optical fiber communications, the widely used wavelength regimes are in the range of 1300~1510-nm. Most of the optical receivers in this regime are based on

the InP substrate material system, i.e. InGaAs, GaInAsP. Our design can be easily adapted to the InP system as well. The InP DBR system has been extensively explored in Vertical-Cavity Surface-Emitting Laser (VCSEL) design. The active region of $In_xGa_{1-x}As$ can be used to match the lattice constant of InP substrate with *x=0.53*, and barrier enhancement layer of $In_{0.52}Al_{0.48}As$ with x = 0.52.

We have previously completed a design with layered structure, shown in the Table 6.3, for InP substrate(The DBR without phosphor for the purpose of fabrication). Other related design can be adapted based on this structure.

Table 6.3 Layered structure for InP material system.

Layer #	Thickness	Material	Specification
8	50 Å	$5*10^{18}$ n+ InGaAs	Cap layer
7	500 Å	$In_{0.52}Al_{0.48}As$	Barrier enhancement layer
6	Si Delta dope	$1*10^{13}$/cm2	
5	50 Å	$In_{0.52}Al_{0.48}As$	Undoped
4	3558 Å	$In_{0.53}Ga_{0.47}As$	Undoped
3	1219 Å (x15)	$In_{0.52}Al_{0.48}As$	15 wells for Bragg reflection
2	1138 Å(x15)	$In_{0.53}Al_{0.13}Ga_{0.34}As$	15 wells for Bragg reflection
1	2000 Å	InP	Thickness is as needed by the grower
0	2"	InP	Semi-insulating Substrate

Low temperature GaAs (LT-GaAs): LT-GaAs material means the growth occurs at temperature ranges around 200-350℃, when high density of defects forms in the crystal, rather than the normal high quantity GaAs growth temperature of 600℃. The high density of defects is caused by excess As, Ga vacancies and the As interstitial defects, where the carriers are easily trapped in these levels. The carrier lifetimes of LT-GaAs can be controlled by either growth temperature or annealing temperature

[153] [154]. By using LT-GaAs, the device response is determined by the carrier trapping time which is much less than the carrier-transit time.

It has been demonstrated that LT-GaAs LT-GaAs can be employed to fabricate the high-speed photodetectors with bandwidths up to several hundred gigahertz at 800-nm wavelength on GaAs substrate for both p-i-n [8] and MSM structures [4].

A sub-picosecond carrier trapping time was observed at long wavelength [154] as well, which allow the material to be employed in high-speed detection at long telecommunication wavelength regimes, i.e. 1300-nm.

It has been demonstrated [154] that long wavelength light can be absorbed in LT-GaAs MSM structure with lower quantum efficiency due to the low absorption coefficient and short carrier trapping time.

6.2 Conclusions and Contributions

In this dissertation, we simulated the two-dimensional-electron-gas (2-DEG) based heterostructure MSM photodetector, and compared it with undoped structure. The static behavior simulations, including 2-D potential profile, electric field distributions, and carrier concentration, were performed with commercially available software ISE-TCAD; The carrier transient behavior in the absorption region was investigated by Ramo's theorem, which accounted for current by summing up the contributions from motion of carriers in the absorption region. The contributions from electrons and holes are separated, which allow us to analyze the time response in detail. The simulation revealed the vertical field in the absorption region enhanced the electron transport.

To study the slow hole transport in the device, a 2-DHG based heterostructure photodetector was designed and simulated. The devices was fabricated and characterized. The reflectance spectrum was

simulated, which showed great consistency with the experimental results. The two-stage dark current was due to the vertical depletion of the 2-DHG and lateral depletion of the absorption region. The simulation of the transient time response revealed similar vertical field, which was developed in the absorption region due to the 2-D gas along the heterostructure. It shows the vertical field facilitates holes transport, but degrades electrons transport. The long tail observed in the experimental data was due to the electrons' slow motion at the bottom of the device. The hole transport in the 2-DHG device is enhanced by the vertical field.

The 2-DHG device also showed high capacitance sensitivity. We obtained a high-sensitivity varactor for high-order frequency multiplier applications. The Cmax/Cmin ratio of 113 and high sensitivity of 35 are the best results reported in the literatures. We investigated the optically modulated sensitivity of the C-V characteristics. A small signal equivalent circuit model was proposed including the major sources of the capacitance; those are charges from delta-doping layer, from 2-DHG and from background charges respectively.

We showed that two-dimensional gas can work as an extended contact to collect photogenerated carriers by means of carrier-carrier scattering which results in a fast energy relaxation time. We studied the transport behavior of two-dimensional carriers, confined by a triangular potential due to the heterostructure, by Ensemble Monte Carlo technique. The detailed two-dimensional electronic states and electron-electron scattering events in the two-dimensional gas were investigated. The result reveals a 30 femto-second thermalization time in the 2-DEG, which allows the photogenerated carriers in equilibrium with the 2D gas and to be collected by the electrode without drifting.

In addition, we designed a 2-DEG/2-DHG structure based high-speed photodetector on GaAs substrate for optical communication applications. It takes the advantages of both vertical field and

confined 2-D gas, and transforms a lateral MSM structure to a vertical one. It improves the speed of the photodetector without sacrificing the external quantum efficiency, namely, the coupling efficiency of optical power to the device, by optimizing the absorption depth rather than further decreasing the finger gap.

The major contributions of this thesis are (1) simulation and analysis the 2-DEG device, revealing a vertical field in the absorption region which facilitates electron transport; (2) design, simulation and analysis of 2-DHG based MSM photodetector, where the slow carrier transport is enhanced by vertical field; analysis its relevant performances; (3) analysis of the mechanism for collection of photogenerated carriers by the 2DEG by means of electron-electron scattering assisted energy thermalization; (4) analysis a 2-DHG varactor device which has shown the highest reported Cmax/Cmin ratio and sensitivity [155]; (5) proposal for a 2-DEG/2-DHG based heterostructure MSM photodetector that takes advantage of vertical field created by the 2-D gas and the fast thermalization time in the 2-D gas.

List of References

[1] H. Onaka, H. Miyata, G. Ishikawa, K. Otsuka, H. Ooi, Y. Kai, S. Kinoshita, M. Seino, H. Nishimoto, and T. Chikama, "1.1 Tb/s WDM transmission over a 150 km 1.3 um zero0dispersion single-mode fiber," presented at Optical Fiber Communication Conference, San Jose, CA, USA, 1996.

[2] G. Keiser, *Optical fiber communication*, 3nd ed: McGraw-Hill, Inc., 2000.

[3] G. W. Anderson, L. E. Chipman, F. J. Kub, D. Park, M. Y. Frankel, T. F. Carruthers, J. A. Modolo, K. D. Hobart, and D. S. Katzer, "Gallium arsenide metal-semiconductor-metal photodiodes as optoelectronic mixers for microwave single-sideband modulation," *Applied Optics*, vol. 37, pp. 28-33, 1998.

[4] J.-W. Shi, K.-G. Gan, Y.-J. Chiu, Y.-H. Chen, C.-K. Sun, Y.-J. Yang, and J. E. Bowers, "Metal-semiconductor-metal traveling-wave photodetectors," *IEEE Photonic Technology Letters*, vol. 16, pp. 623-625, 2001.

[5] S. Y. Chou and M. Y. Liu, "Nanoscale tera-hertz metal-semiconductor-metal photodetectors," *IEEE Journal of Quantum Electronics*, vol. 28, pp. 2358-2368, 1992.

[6] D. Lasaosa, J.-W. Shi, D. Pasquariello, K.-G. Gan, M.-C. Tien, H.-H. Chang, S.-W. Chu, C.-K. Sun, Y.-J. Chiu, and J. E. Bowers, "Traveling-Wave Photodetectors With High Power-Bandwidth and Gain-Bandwidth Product Performance," *IEEE Journal of Selected Topic on Quantum Electronics*, vol. 10, pp. 728-741, 2004.

[7] J. J. E. Bowers and C. A. Burrus, "High-speed zero-bias waveguide photodetectors," *Electronics Letters.*, vol. 22, pp. 905-906, 1986.

[8] Y. J. Chiu, S. B. Fleischer, and J. E. Bowers, "High-speed lower-temperature-grown GaAs p-i-n traveling-wave photodetector," *IEEE Photonic Technology Letters*, vol. 10, pp. 1012-1014, 1998.

[9] C. C. Barron, C. J. Mahon, B. J. Thibeault, G. Wang, W. Jiang, L. A. Coldren, and J. E. Bowers, "Resonant-cavity-enhanced pin photodetector with 17 GHz bandwidth-efficiency product," *Electronics Letters*, vol. 30, pp. 1796-1797, 1994.

[10] S. Donati, *Photodetectors: devices, circuits, and applications*. Upper Saddle River: Prentice-Hall PTR, 2000.

[11] M. Razeghi, "Optoelectronic devices based on III-V compound semiconductors which have made a major scientific and technological impact in the past 20 years," *IEEE Journal on Selected Topics in Quantum Electronics*, vol. 6, pp. 1344-1354, 2000.

[12] J. Singh, *Semiconductor Devices*: McGraw-Hall, 1993.

[13] J. Harari, J.-P. Vilcot, and D. Decoster, "Metal semiconductor metal photodetectors," in *Wiley encyclopedia of electrical and electronics engineering*, vol. 12, J. G. Webster, Ed., 1999, pp. 561-577.

[14] S. S. Gevorgian, T. Martinsson, P. L. J. Linner, and E. L. Kollberg, "CAD models for multilayered substrate interdigital capacitors," *IEEE transactions on microwave theory and techniques*, vol. 44, pp. 896-904, 1996.

[15] R. L. N. K. S. Giboney, T. E. Reynolds, S. T. Allen, R. P. Mirin, M. J. W. Rodwell,and J. E. Bowers "Traveling-wave photodetectors with 172-GHz bandwidth and 76-GHz bandwidth-efficiency product," *IEEE Photonic Technology Letters*, vol. 7, pp. 412-414, 1995.

[16] S. M. Sze, *Physics of semiconductor devices*, 2nd ed. New York: John Wiley & Sons, Inc, 1981.

[17] K. Kato, K. Kawano, and A. Kozen, "Design of ultrawide-band, high sensitivity p-i-n photodetectors," presented at IEICE Trans. Electron., 1993.

[18] I. H. Tan, C. K. Sun, K. S. Giboney, J. E. Bowers, E. L. Hu, B. I. Miller, and R. J. Capic, "120-GHz long-wavelength low-capacitance photodetector with an air-bridged coplannar metal waveguide," *IEEE Photonic Technology Letters*, vol. 7, pp. 1477-1479, 1995.

[19] J. E. B. a. C. A. Burrus, "Ultrawide-band long-wavelength p-i-n photodetectors," *Journal of Lightwave Technology*, vol. LT-5, pp. 1339-1350, 1987.

[20] K. Kato, "Ultrawide-band/high-frequency photodetectors," *IEEE transactions on Microwave Theory and Techniques*, vol. 47, pp. 1265-1281, 1999.

[21] K. Kishino, M. Unlu, J. Chyi, J. Reed, L. Arsenault, and H. Morkoc, "Resonant cavity-enhanced (RCE) photodetectors," *IEEE Journal of Quantum Electronics*, vol. 27, pp. 2025-2034, 1991.

[22] S. Ramo, "Currents induced by electron motion," presented at Proceedings of the I.R.E., 1939.

[23] M. Achouche, V. Magnin, J. Harari, L. Lelarge, E. Derouin, C. Jany, D. Carpentier, F. Blache, and D. Decoster, "High performance evanescent edge coupled waveguide unitraveling-carrier pohtodiodes for >40-Gb/s optical receivers," *IEEE Photonics Technology Letters*, vol. 16, pp. 584-586, 2004.

[24] S. M. Sze, D. J. Coleman, Jr., and A. Loya, "Current transport in metal-semiconductor-metal (MSM) structures," *Solid-state Electron*, vol. 14, pp. 1209-1218, 1971.

[25] C. H. Lee, *Picosecond optoelectronic devices*. New York: Academic, 1984.

[26] R. A. Lawton and A. Scavannec, "Photoconductive detectors of fast-transition optical waveforms," *Electron Letters*, vol. 11, pp. 74-75, 1975.

[27] D. H. Auston, A. M. Johnson, P. R. Smith, and J. C. Bean, "Picosecond optoelectronic detection, sampling , and correlation measurements in amorphous semiconductors," *Applied Physics Letters*, vol. 37, pp. 371-373, 1980.

[28] F. E. Doany, D. Grischkowsky, and C. C. Chi, "Carrier lifetime versus ion-implantation dose in silicon on sapphire," *Applied Physics Letters*, vol. 50, pp. 460-462, 1987.

[29] S. Y. Wang and D. M. Bloom, "100-GHz bandwidth planar GaAs Schottky photodiode," *Electronics Letters*, vol. 19, 1983.

[30] W. P. B. J. van Zeghbroeck, J. M. Halbout, and P Vettiger, "105-GHz bandwidth metal-semiconductor-metal photodiode," *IEEE Electronics Device Letters*, vol. 9, pp. 527-529, 1988.

[31] E. Ozbay, K. D. Li, and D. M. Bloom, "2.0 ps, 150 GHz GaAs monolithic photodiode and all-electronic sampler," *IEEE Photonics Technology Letters*, vol. 3, pp. 570-572, 1991.

[32] Y. Chen, S. Williamson, T. Brock, F. W. Smith, and A. R. Calawa, "375-GHz photodiode on low-temperature GaAs," *Applied Physics Letters*, vol. 59, pp. 1984-1986, 1991.

[33] J. B. D. Soole and H. Schumacher, "Transit-time limited frequency response of InGaAs MSM photodetector," *IEEE Transactions on Electron Devices*, vol. 37, pp. 2285-2291, 1990.

[34] X. Zhou, T. Y. Hsiang, and R. J. D. Miller, "Monte Carlo study of photogenerated carrier transport in GaAs surface space-charge fields," *Journal of Applied Physics*, vol. 66, pp. 3066-3073, 1989.

[35] X. Chen, B. Nabet, A. Cola, F. Quaranta, and M. Currie, "A delta-doped resonant cavity enhanced heterostructure metal-semiconductor-metal photodetector," *IEEE Electron Device Letters*, vol. 24, pp. 312-315, 2003.

[36] D. L. Crawford, Y. G. Wey, A. Mar, J. E. Bowers, M. J. Hafich, and G.Y.Robinson, "Highspeed InGaAs/InP p-i-n photodiodes fabricated on a semi-insulating substrate," *IEEE Photonics Technology Letters*, vol. 2, pp. 647-649, 1990.

[37] Y. G. Wey, D. L. Crawford, K. Giboney, J.E. Bowers, M.J. Rodwell, P. Silvestre, M.J. Jafich, and G. Y. Robinson, "Ultrafast graded double-heterostructure GaInAs/InP photodiode," *Applied Physics Letters*, vol. 58, pp. 2156-2158, 1991.

[38] Y. I. K. Kato; A. Kozen; Y. Muramoto, T. Nagatsuma, and M. Yaita "110-GHz, 50%-efficiency mushroom-mesa waveguide p-i-n photodiode for a 1.55-um wavelength," *IEEE Photonic Technology Letters*, vol. 6, pp. 719-721, 1994.

[39] K. Kato, A. Kozen, Y. Muramoto, Y. Itaya, T. Nagatsuma, and M. Yaita, "110-GHz, 50%-efficiency mushroom-mesa waveguide p-i-n photodiode for a 1.55-um wavelength," *IEEE Photonic Technology Letters*, vol. 6, pp. 719-721, 1994.

[40] M. W. N.Shimizu, T. Furuta, and T. Ishibashi, "InP-InGaAs unitraveling-carrier photodiode with improved 3-dB bandwidth of over 150 GHz," *IEEE Photonics Technology Letters*, vol. 10, pp. 412-414, 1998.

[41] A. Stőhr, A. Malcoci, A. Sauerwald, I. C. Mayorga, R. Gusten, and D. S. Jager, "Wide-Band Traveling-Wave Photodetectors for Photonic Local Oscillators," *Journal of Lightwave Technology*, vol. 21, pp. 3062-3070, 2003.

[42] M. S. Ünlü and S. Strite, "Resonant cavity enhanced photonic devices," *Journal of Applied Physics*, vol. 78, pp. 607-639, 1995.

[43] K. S. Giboney, M. J. W. Wodwell, and J. E. Bowers, "Traveling-wave photodetector theory," *IEEE transactions on microwave theory and techniques*, vol. 45, pp. 1310-1319, 1997.

[44] M. Jutzi, K. Eve, W. Vogel, D. Wiegner, and M. Berroth, "Lateral PIN-photodetector in commercial CMOS technology operating at 1.25 Gbit/s and 850 nm," presented at 7th Workshop Optics in Computing Technology, Mannheim, 2002.

[45] M. Siegert, M. LOken, C. Glingener, and C. Buchal, "Efficient optical coupling between a polymeric waveguide and an ultrafast silicon MSM photodiode," *IEEE Journal of Selected Topic on Quantum Electronics*, vol. 4, pp. 970-974, 1998.

[46] S.-Y. Lo, Y.-L. Wei, R.-H. Yeh, and J.-W. Hong, "Suppressing dark-current in planar Si-based MSM photodetetor with alternated i-a-Si:H/i-a-SiGe:H grade superlattice-like layers," *Electronics Letters*, vol. 41, 2005.

[47] R. P. Macdonald, N. G. Tarr, B. A. Syrett, S. A. Boothroyd, and J. Chrostowski, "MSM photodetector fabriated ph polycrystalline silicon," *IEEE Photonics Technology Letters*, vol. 11, pp. 108-110, 1999.

[48] K. Nakajima, T. Ikda, K.-I. Sugimoto, H. Kan, and Y. Mizushima, "Properties and design of the ultrafast GaAs metal-semiconductor-metal photodetector with symmetrical Schottky contact," *IEEE Transactions on Electron Devices*, vol. 37, pp. 31-35, 1990.

[49] W. C. Koscielniak, J. L. Pelouard, and M. A. Littlejohn, "Dynamic behavior of photocarriers in a GaAs metal-semiconductor-metal photodetector with sub-half-micron electrode pattern," *Applied Physics Letters*, vol. 54, pp. 567-569, 1989.

[50] E. Sano, "Two-dimensional ensemble Monte Carlo calculations of pulse response of submicrometer GaAs metal-semiconductor-metal photodetectors," *IEEE Transactions on Electron Devices*, vol. 38, pp. 2075-2081, 1991.

[51] C. Moglestue, J. Rosenzweig, J. Kuhl, M. Klingenstein, M. Lambsdorff, A. Axmann, J. Schneider, and A. Hulsmann, "Picosecond pulse response characteristics of GaAs metal-semiconductor-metal photodetectors," *Journal of Applied Physics*, vol. 70, pp. 2435-2448, 1991.

[52] S. Averin, R. Sachot, J. Hugi, M. de Fays, and M. Ilegems, "Two-dimensional device modeling and analysis of GaInAs metal-semiconductor-metal photodiode structures," *Journal of Applied Physics*, vol. 80, pp. 1553-1558, 1996.

[53] G. B. Tait and B. Nabet, "Current transport modeling in quantum-barrier-enhanced heterodimentional contact," *IEEE Transactions on Electron Devices*, vol. 50, pp. 2573-2578, 2003.

[54] N. Grote and H. Venghaus, *Fiber Optic Communication Devices*. Germany, Springer-verlag, 2000.

[55] T. Sugeta and T. Urisu, "High-gain-metal-semiconductor-metal photodetector for high-speed optoelectronic circuits," *IEEE Transactions of Electronics Devices*, vol. ED-26, pp. 1855-1979, 1979.

[56] M. Ito, O. Wada, K. Nakai, and T. Sadnrai, "Monolithic integration of a metal-semiconductor-metal photodiode and a GaAs preamplifier," *IEEE Electron Device Letters*, vol. ED-5, pp. 531-532, 1984.

[57] Y. C. Lim and R. A. Moore, "Properties of alternately charged co-planar parallel strips by conformal mappings," *IEEE Transactions on Electron Devices*, vol. ED-15, pp. 173-180, 1968.

[58] W. C. Koscielniak, J. L. Pelouard, R. M. Kolbas, and M. J. Littlejohn, "Dark current characteristics of GaAs metal-semiconductor-metal (MSM) photodetectors," *IEEE Transactions on Electron Devices*, vol. 37, pp. 1632, 1990.

[59] P. A. Houston and A. G. R. Evans, "Electron drift velocity in n-GaAs at high electric fields," *Solid State Electron.*, vol. 20, pp. 197-204, 1977.

[60] J. S. Blakemore, "Intrinsic density ni(T) in GaAs: deduced from band gap and effective mass parameters and derived independently from Cr acceptor capture and emission coefficients," *Journal of Applied Physics*, vol. 53, pp. 520-531, 1982.

[61] J. Pozhela and A. Reklaitis, "Electron transport properties in GaAs at high electric " *Solid State Electron.*, vol. 23, pp. 927-933, 1980.

[62] V. L. Dalal, A. B. Dreeben, and A. Triano, "Temperature Dependence of Hole Velocity in p-GaAs," *Journal of Applied Physics*, vol. 42, pp. 2864-2867, 1971.

[63] X. Chen, "Novel heterostructure metal-semiconductor-metal (HMSM) photodetector with resonant cavity for fiber optical communications," in *Electrical and computer engineering department*. Philadelphia: Drexel University, 2002.

[64] S. G. Petrosyan and A. Y. Shik, "Contact phenomena in a two-dimensional electron gas," *Sov. Phys. Semicond.*, vol. 23, pp. 696-697, 1989.

[65] J. Mares, J. Kristofik, and P. Hubik, "The screening properties of 2DEG in the intergral quantum hall regime," presented at 3rd international euro conference on advance semiconductor device and microsystems, Smolenice Castle, Slovakia, 2000.

[66] S. Wang, *Fundamentals of semiconductor theory and device physics*: Prentice-Hall, 1989.

[67] L. Reggianni, Private communications, 2003.

[68] M. Lundstrom, *Fundamentals of carrier transport*, 2nd ed. New York: Cambridge University Press, 2000.

[69] C. Jacoboni and L. Reggiani, "The monte carlo method for the solution of charge transport in semiconductors with applications to covalent materials," *Reviews of Modern Physics*, vol. 55, pp. 645-705, 1983.

[70] K. Tomizawa, *Numerical Simulation of Submicron Semiconductor Devices*. Boston: Artech House, 1993.

[71] J. Blair and J. Krusius, "Monte Carlo simulation of the fundamental photodetector response on sub-picosecond time scales," presented at IEEE Cornell conference on advanced concepts, 1995.

[72] Z. Susnjar, Z. Djuric, M. Smiljanic, and Z. Lazic, "Numerical calculation of photodetector response time useing ramo's theorem," presented at Proc. 20th international conference on microelectronics Nis, Serbia, 1995.

[73] IOFFE, "Semiconductors on NSM."

[74] H. Morkoc, B. Sverdlov, and G.-b. Gao, "Strained layer heterostructures, and their applications to MODFET's, HBT's, and Lasers," presented at Proceedings of the IEEE, 1993.

[75] G. C. Osbourn, "Recent trends in III–V strained layer research " *Journals of Vacuum and Science Technology B*, vol. 4, pp. 1423, 1986.

[76] J. W. Matthews and A. E. Blakeslee, "Defects in epitaxial multilayer," *Journals of Crystal Growth* vol. 27, pp. 118-125, 1974.

[77] E. Schirber, I. J. Fritz, and L. R. Dawson, "Light-hole conduction in InGaAs/GaAs strained-layer superlattices " *Applied Physics Letters*, vol. 46, pp. 187-189, 1985.

[78] M. Ciorga, M. Kubisa, K. Ryczko, L. Bryja, J. Misiewicz, and O. P. Hansen, "Observation of excitons formed by the holes confined at the Al0.5Ga0.5As/GaAs interface," *Microelectronic Engineering*, vol. 51-52, pp. 235-240, 2000.

[79] H. L. Stőrmer, K. Baidwin, A. C. Gossard, and W. Wiegmann, "Modulation-doped field-effect transistor based on a two-dimensiontal hole gas," *Applied Physics Letters*, vol. 44, 1984.

[80] W. I. Wang, E. E. Mendez, and F. Stern, "High mobility hole gas and valence-band offset in modulation-doped p-AlGaAs/GaAs heterojunctions," *Applied Physics Letters*, vol. 45, pp. 639-641, 1984.

[81] G. Li and C. Jagadish, "Recent progress in δ-doping of III-V semiconductors grown by metal organic vapor phase epitaxy," *Solid-State Electronics*, vol. 41, pp. 1207-1225, 1997.

[82] C. E. C. Wood, G. Metze, J. Berry, and L. F. Eastman, "Complex free-carrier profile synthesis by "atomic-plane" doping of MBE GaAs," *J. Appl. Phys.*, vol. 51, pp. 383-385, 1980.

[83] S. Sassen, B. Witzigmann, C. Wolk, and H. Brugger, "Barrier height engineering on GaAs THz Schottky diodes by means of high-low doping InGaAs- and InGaP- Layers," *IEEE Transactions of Electronics Devices*, vol. 47, pp. 24-31, 2000.

[84] A. Anwar and B. Nabet, "Barrier enhancement mechanisms in heterodimensional contacts and their effect on current transport," *IEEE transactions on microwave theory and techniques*, vol. 50, pp. 68-71, 2000.

[85] R. Ragi, M. A. Romero, and B. Nabet, "Modeling the electrical characteristics of Schottky contacts in low-dimensional heterstructure devices," *IEEE transactions on electron devices*, vol. 52, pp. 170-175, 2005.

[86] F. A. Padovani and R. Stratton, "The accuracy of the WKB approximation for tunneling in metal-semiconductor junction," *Applied Physics Letters*, vol. 13, pp. 167-169, 1968.

[87] M. Born and E. Wolf, *Principles of Optics*. Cambridge, London, 1999.

[88] D. T. F. Marple, "Refractive index of GaAs," *Journal of Applied Physics*, vol. 35, pp. 1241-1242, 1964.

[89] D. D. Sell, H. C. Casey, and K. W. Wecht, "Concentration dependence of the refractive index for n - and p -type GaAs between 1.2 and 1.8 eV," *Jounal of applied physics*, vol. 45, pp. 2650-2657, 1974.

[90] R. E. Fern and A. Onton, "Refractive Index of AlAs," *Journal of applied physics*, vol. 42, pp. 3499-3500, 1971.

[91] D. E. Aspnes, S. M. Kelso, R. A. logan, and R. Bhat, "Optical properties of AlxGa1–x As," *Journal of applied physics*, vol. 60, pp. 754-767, 1986.

[92] H. C. Casey, D. D. Sell, and M. B. Panish, "Refractive index of AlxGa1–xAs between 1.2 and 1.8 eV," *Applied Physics Letters*, vol. 24, pp. 63-65, 1974.

[93] J. P. Van der Ziel and A. C. Gossard, "Absorption, refractive index, and birefringence of AlAs-GaAs monolayers," *Journal of applied physics*, vol. 48, pp. 3018-3023, 1977.

[94] D. J. Deri and M. A. Emanuel, "Consistent formular for the refractive index of AlxGa1-xAs below the band edge," *Journal of applied physics*, vol. 77, pp. 4667-4672, 1995.

[95] H. C. Jr. Casey, D. D. Sell, and K. W. Wecht, "Concentration dependence of teh absorption coefficient for n- and p- type GaAs between 1.3 and 1.6 eV," *Journal of Applied Physics*, vol. 46, pp. 250, 1975.

[96] B. G. Streetman and S. Banerjee, *Solid State Electronic Devices*, 5 ed. Upper saddle river, New Jersey: Prentice Hall, 2000.

[97] H. Kroemer, W. Y. Chien, J. S. Jr. Harris, and D. D. Edwall, "Measurement of isotype heterojunction barriers by C-V profiling," *Applied Physics Letters*, vol. 36, pp. 295-297, 1980.

[98] M. A. Rao, E. J. Caine, H. Kroemer, S. I. Long, and D. I. Babic, "Determination of valence and conduction-band discontinuities at GaInP/GaAs heterojunction by C-V profiling," *Journal of Applied Physics*, vol. 61, pp. 643-649, 1987.

[99] P. Penfield and R. P. Rafuse, *Varactor Applications*. Cambridge,MA: The M.I.T. Press, 1962.

[100] J. Maget, M. Tiebout, and R. Kraus, "Influence of novel MOS varactors on the performance of a fully integrated UMTS VCO standard 0.25-μm CMOS technology," *IEEE Journals of Solid-State Circuits*, vol. 37, pp. 953-958, 2002.

[101] G. Chattopadhyay, E. Schlecht, J. S. Ward, J. J. Gill, H. H. S. Javadi, F. Maiwald, and I. Mehdi, "An all-solid-state broad-brand frequency multiplier chain at 1500 GHz," *IEEE Transactions on Microwave Theory and Techniques*, vol. 52, pp. 1538-1547, 2004.

[102] E. L. Kollberg and A. Rydberg, "Quantum-barrier-varactor diode for high efficiency millimeter-wave multipliers," *Electronics Letters*, vol. 25, pp. 1696-1697, 1989.

[103] E. Lheurette, X. Melique, P. Mounaix, F. Mollot, O. Vanbesien, and D. Lippens, "Capacitance engineering for InP-Based Heterostructure Barrier Varactor," *IEEE Electron Device Letters*, vol. 19, pp. 338-340, 1998.

[104] R. Meola, J. Freyer, and M. Claassen, "Improved frequency tripler with intergrated single-barrier varactor," *Electronics Letters*, vol. 36, pp. 803-804, 2000.

[105] J. Vukusic, B. Alderman, T. A. Emadi, M. Sadeghi, A. Ø. Olsen, T. Bryllert, and J. Stake, "HBV Tripler with 21% efficiency at 102 GHz," *Electronics Letters*, vol. 42, pp. 355-356, 2006.

[106] Q. Xiao, Y. Duan, J. L. Hesler, T. W. Crowe, and R. M. Weikle, "A 5-mW and 5% Efficiency 210 GHz InP-Based Heterostructure Barrier Varactor Quintupler," *IEEE Microwave and Wireless Components Letters*, vol. 14, pp. 159-161, 2004.

[107] M. Marso, M. Wolter, P. Javarka, A. Fox, and P. Kordos, "AlGaN/GaN varactor diode for integration in HEMT circuits," *Electronics Letters*, vol. 37, pp. 1476-1478, 2001.

[108] A. Anwar, B. Nabet, and J. Culp, "An electrically and optically gate-controlled Schottky/2DEG varactor," *IEEE Electron Device Letters*, vol. 21, pp. 473-475, 2000.

[109] M. Schefer, U. Lott, H. Benedickter, B. U. Klepser, W. Patrick, and W. Bachtold, "Monolithic coplanar, varactor tunable V-band HEMT oscillators with injection locking capability," *Electronic Letters*, vol. 32, pp. 1899-1900, 1996.

[110] B. Gelmont, M. Shur, and C. Moglesture, "Theory of junction between two-dimensional electron gas and p-type semiconductor," *IEEE Transactions of Electronics Devices*, vol. 39, 1992.

[111] M. J. Chou, D. C. Tsui, and G. Weimann, "Negative photoconductorivity of two-dimensional holes in GaAs/AlGaAs heterojunctions," *Applied Physics Letters*, vol. 47, 1985.

[112] T. Makimoto, N. Kobayashi, and Y. Horikoshi, "Electron conduction in GaAs atomic layer doped with Si," *J. Appl. Phys.*, vol. 63, pp. 5023-5026, 1988.

[113] J. A. Correa, F. A. G. de Oliverira, M. I. M. de Silva, M. V. B. Moreira, G. M. Riberiro, and H. Chacham, "Temperature dependence of the equilibrium Hall concentration in silicon planar-doped GaAs samples," *Solid St. Commum.*, vol. 98, pp. 1063-1068, 1996.

[114] E. F. Schubert, J. E. Cunningham, and W. T. Tsang, "Electron-mobility enhancement and electron-concentration enhancement in δ-doped n-GaAs at T=300K," *Solid St. Commun.*, vol. 63, pp. 591-594, 1987.

[115] W. Walukiewicz, "Hole-scattering mechanisms in modulation–doped heterostructures," *Journal of applied physics*, vol. 59, 1986.

[116] I. Bahl and P. Bhartia, *Microwave solid state circuit design*. Hoboken, New Jersey: John Wiley & Sons, Inc., 2003.

[117] K. H. K. Yokoyama, "Monte carlo studen of electronic transport in algaas/gaas single-well heterostructures," *Physics Review B*, vol. 33, pp. 5595-5606, 1986.

[118] M. Goano, "Algorithm 745. Computation of the complete and incomplete Fermi-Dirac integral," *Trans. Math. Software*, vol. 21, pp. 221-232, 1995.

[119] M. Goano, "Series expansion of the Fermi-Dirac integral F_j(x)! over the entire domain of real j and x," *Solid-State Electronics*, vol. 36, pp. 217-221, 1993.

[120] C. Chow, "Computer Solutions to the Schrödinger Equation," *Am. J. Phys*, vol. 40, pp. 730-734, 1972.

[121] P. Harrison, "The nature of the electron distribution functions in quantum cascade lasers," *Applied Physics Letters*, vol. 72, pp. 2800-2802, 1999.

[122] E. Abrahams, "Electron-Electron Scattering in Alkali Metals " *Physics Review* vol. 95, pp. 839, 1954.

[123] C. J. Hearn, *The physics of nonlinear transport in semiconductors*. New York, NY: Plenum, 1980.

[124] S. M. Goodnick and P. Lugli, "Effect of electron-electron scattering on nonequilibrium transport in quantum-well systems," *Physical Review B*, vol. 37, pp. 2578-2588, 1988.

[125] P. Lugli and D. K. Ferry, "Degeneracy in the ensemble Monte carlo method for high-field transport in semiconductors," *IEEE transactions on electron devices*, vol. ED-32, pp. 2431-2437, 1985.

[126] R. Brunetti, C. Jacoboni, A. Matulionis, and V. Dienys, "Effect of interparticle collision on energy relaxation of carriers in semiconductors," *Physica 134B*, vol. 32, pp. 369-373, 1985.

[127] W. Knox, D. Chemla, G. Livescu, and J. E. Henry, "Femtosecond carrier thermalization in dense fermi seas," *Physics Review Letters*, vol. 61, pp. 1290-1293, 1988.

[128] I. Vurgaftman and J. Singh, "Monte Carlo study of electron relaxation in quantum-wire laser structures," *IEEE Journal of quantum electronics*, vol. 30, pp. 2012-2025, 1994.

[129] T. Ando, "Electronic properties of two-dimensional systems," *Reviews of Modern Physics*, vol. 54, pp. 437-672, 1982.

[130] Z. Q. Zou and Y. P. Lee, "Comparison of the collective excitation spectra of three-, two- and one-dimensional electron systems," *Physica B*, vol. 305, pp. 155-163, 2001.

[131] S. Adachi, *Properties of aluminum gallium arsenide*, 3th ed: INSPEC 1993.

[132] P. M. Mooney, N. S. Caswell, and S. L. Wright, "The capture barrier of the DX center in Si-doped AlxGa1–xAs," *Journal of Applied Physics*, vol. 62, pp. 4786-4797 1987.

[133] N. Chand, T. Henderson, J. Klem, W. T. Masselink, R. Fischer, Y. C. Chang, and H. Morkoc, "Comprehensive analysis of Si-doped AlxGa1-xAs (x=0 to 1)," *Physical Review B*, vol. 30, pp. 4481-4492, 1984.

[134] J. L. Thobel, L. Baudry, A. Cappy, P. Bourel, and R. Fauquembergue, "Electron transport properties of strained InxGa1-xAs," *Applied Physics Letters*, vol. 56, pp. 346-348, 1990.

[135] D. I. Babic and S. W. Corzine, "Analytic expressions for the reflection delay, penetration depth, and absorptance of quarter-wave dielectric mirrors," *IEEE Journal of Quantum Electronics*, vol. 28, pp. 514-524, 1992.

[136] R. E. Williams, *Gallium Arsenide processing techniques*. Dedham: Artech House, Inc, 1984.

[137] W. C. Koscielniak, J.-l. Pelouard, and M. A. Littlejohn, "Intrinsic and extrinsic response of GaAs metal-semiconductor-metal photodetectors," *IEEE Photonics Technology Letters*, vol. 2, pp. 125-127, 1990.

[138] E. H. Bottcher, D. Kuhl, F. Hieronymi, E. Droge, T. Wolf, and D. Bimberg, "Ultrafast semiinsulation InP-InGaAs-InP MSM Photodetectors, modeling and performance," *IEEE Journal of Quantum Electronics*, vol. 28, pp. 2343-2357, 1992.

[139] R. W. Jackson, "Coplanar waveguid vs. microstrip for millimeter wave integrated circuits," presented at IEEE-MTT-S International microwave symposium digest, 1986.

[140] M. Dyakonov and M. Shur, "Detection, mixing, and frequency multiplication of terahertz adiation by two-dimensional electronic fluid," *IEEE transactions on electron devices*, vol. 43, pp. 380-387, 1996.

[141] W. Knap, J. Lusakowski, T. Parenty, S. Bollaert, A. Cappy, V. V. Popov, and M. S. Shur, "Terahertz emission by plasma waves in 60 nm gate high electron mobility transistors," *Applied Physics Letters*, vol. 84, pp. 2331-2333, 2004.

[142] M. Dyakonov and M. Shur, "Shallow water analogy for a ballistic field effect transistor: new mechanism of plasma wave generation by DC current," *Physical Review Letters*, vol. 71, pp. 2465-2468, 1993.

[143] W. Knap, Y. Deng, S. Rumyantsev, and M. S. Shur, "Resonant detection of subterahertz and terahertz radiation by plasma waves in submicron field-effect transistors," 2002.

[144] J. Q. Lu, M. S. Shur, R. Weikle, and M. I. Dyakonov, "Detection of microwave radiation by electronic fluid in AlGaN/GaN high electron mobility transistors," presented at 16th Biennial conference of advanced concepts high-speed semiconductor. devices circuits, Ithaca, NY, 1997.

[145] R. Weikle, J. W. Lu, M. S. Shur, and M. I. Dyakonov, "Detection of microwave radiation by electronic fluid in high electron mobility transistors," *Electron. Lett.*, vol. 32, pp. 2148-2149, 1996.

[146] X. G. Peralta, S. J. Allen, M. C. Wanke, N. E. Harff, J. A. Simmons, P. Lilly, J. L. Reno, J. G. Burke, and J. P. Eisenstein, "Terahertz photoconductivity and plasmon modes in double-quantum-well field-effect transistors," *Applied Physics Letters*, vol. 81, pp. 1627-1629, 2001.

[147] F. J. Crowne, "Contact boundary conditions and the Dyakonov-Shur instability in high electron mobility transistors," *Journal of Applied Physics*, vol. 82, pp. 1242-1254, 1997.

[148] S. Rudin and G. Samsondidze, "Edge and strip plasmons in a two0dimensional electron fluid," *Physics Review B*, vol. 58, pp. 16369-16373, 1998.

[149] W. C. B. Peatman, H. Park, and M. Shur, "Two-dimensional metal-semiconductor field effect transistor for ultra low power circuit applications," *IEEE Electron Device Letters*, vol. 15, pp. 245-247, 1994.

[150] T. Ytterdal, M. Hurt, M. Shur, H. Park, R. Tsai, and W. C. B. Peatman, "High-temperature characteristics of two-dimensional MESFETs," *IEEE Electron Device Letters*, vol. 17, pp. 214-216, 1996.

[151] T. Ytterdal, M. S. Shur, M. Hurt, and W. C. B. Peatman, "Enhancement of Schottky barrier height in heterodimensional metal-semiconductor contacts," *Applied Physics Letters*, vol. 70, pp. 441-442, 1996.

[152] R. A. Katkar and G. B. Tait, "Modeling of current density boundary conditions for a heterodimensional contact of 3D metal to 2D semiconductor," *Journal of computational electronics*, vol. 3, pp. 5-12, 2004.

[153] E. S. Harmon, M. R. Melloch, J. M. Woodall, D. D. Nolte, N. Otsuka, and C. L. Chang, "Carrier lifetime versus anneal in low temperature growth GaAs," *Applied Physics Letters*, vol. 63-16, 1993.

[154] P. Grenier and J. F. Whitaker, "Subband gap carrier dynamics in low-temperature grown GaAs," *Applied Physics Letters*, vol. 70, pp. 1998-2000, 1997.

[155] X. Zhao, A. Cola, A. Tersigni, F. Quaranta, E. Gallo, J. Spanier, and B. Nabet, "Optically modulated high-sensitivity heterostructure varactor," *IEEE Electron Device Letters*, vol. 27, pp. 710-712, 2006.

Vita

Xia Zhao was born in Wuhan, Hubei, P. R. China in September 1976. She received her degree of Bachelor of Science majoring in electrical engineering from Huazhong University of Science and Technology in June of 1998, and degree of Master of Science majoring in electrical engineering from Institute of Microelectronics R&D Center, Chinese Academy of Sciences in June of 2001. Since February 2002, she joined optoelectronics laboratory, working with Dr. Bahram Nabet in Electrical and Computer Engineering department, Drexel University for graduate study toward Ph.D. degree. During her stay at Drexel University, she has involved with many research activities, including carrier transport in low dimensional structures and formulism of confined structures, such as 2-D and 1-D, resonant cavity quantum dot photodetector, teraherze radiation sensor, vertical field high-speed MSM photodetector design on both GaAs and InP material systems, simulations of the static and dynamic behavior of heterostructure devices using commercial available software or developing codes by numerical methods. Her main interests of research are low-dimensional semiconductor device design and performance analysis. Over her graduate study at Drexel University, she accomplished design of 2-DHG MSM photodetector, simulation of vertical field heterostructure, analysis of slow carrier transport for high-speed photodetector. Her research activities have been published in many prestigious technical journals, including IEEE Electron Device Letters. IEEE Trans. on Electronic Device, Microelectronics. So far, she published three journal papers, five conference papers. She is preparing two more journal papers.